5-2015

Optimization and Control of Lumped Transmitting Coil-Based In-Motion Wireless Power Transfer Systems

Nazmul Hasan
Utah State University

Follow this and additional works at: https://digitalcommons.usu.edu/etd

Part of the Electrical and Computer Engineering Commons

OPTIMIZATION AND CONTROL OF LUMPED TRANSMITTING

COIL-BASED IN-MOTION WIRELESS POWER TRANSFER SYSTEMS

by

Nazmul Hasan

A thesis submitted in partial fulfillment
of the requirements for the degree

of

MASTER OF SCIENCE

in

Electrical Engineering

Approved:

Dr. Zeljko Pantic	Dr. Regan Zane
Major Professor	Committee Member

Dr. Rajnikant Sharma	Dr. Mark R. McLellan
Committee Member	Vice President for Research and
	Dean of the School of Graduate Studies

UTAH STATE UNIVERSITY
Logan, Utah

2015

Abstract

Optimization and Control of Lumped Transmitting Coil-Based In-Motion Wireless Power

Transfer Systems

by

Nazmul Hasan, Master of Science

Utah State University, 2015

Major Professor: Dr. Zeljko Pantic

Department: Electrical and Computer Engineering

Wireless inductive power transfer systems are the only viable option for transferring energy to a moving vehicle. In recent years, there has been a great deal of interest in in-motion vehicle charging. The dominant technology thus far for in motion charging is elongated tracks, creating a constant field for the moving vehicle. This technology suffers from high volt ampere ratings and lower efficiency of 70%. On the other hand, stationary charging systems can demonstrate efficiency upto 95%. This thesis proposes lumped coils, similar to stationary charging coils for in-motion electric vehicle charging application. This novel primary coil architecture introduces new challenges in optimization and control. Traditional design of wireless inductive power transfer systems require designer experience, use of time consuming 3D FEM algorithms and lacks the comprehensive nature required for these systems. This thesis proposes two new optimization algorithms for the design problem which are comprehensive, based on only analytical formulations and do not need designer experience. There are challenges in the control of power transfer as well. Higher efficiency comparable to stationary systems can only be realized with proper synchronization of primary voltage with the vehicle position. Vehicle position detection and communication introduce significant cost and convenience issues. This thesis proposes a novel control

algorithm which eliminates the need for vehicle position sensing and yet transfers the required percentage of energy. Both the optimization and control algorithms are verified with hardware setup.

(130 pages)

Public Abstract

Optimization and Control of Lumped Transmitting Coil-Based In-Motion Wireless Power

Transfer Systems

by

Nazmul Hasan, Master of Science

Utah State University, 2015

Major Professor: Dr. Zeljko Pantic
Department: Electrical and Computer Engineering

This thesis explores optimization and control aspects of in-motion electric vehicle charging. The vision is of an electrified roadway, where the vehicles can move and charge at the same time. The present systems have long tracks embedded in the roadway which transfer energy. This thesis explores smaller coils in the road, which has the promise of higher efficiency and lower volt ampere ratings. The promise can only be realized through optimized design and synchronized control of charging with respect to vehicle position. The existing design procedures lack comprehensiveness, require designer experience and use computationally costly 3D FEM algorithms. The proposed optimization algorithms are comprehensive, eliminates designer experience and employs analytical modeling. The control of power transfer is very much related to proper synchronization of the power transfer with vehicle position. Vehicle position detection can be inaccurate as well as costly. Thus, the idea is to develop a sensorless power transfer control, which can control the power transfer without the need of any position sensing.

To my beloved parents:
Dr. Md. Alauddin and Kumrun Nahar Chawdhury
and my only younger sister, who always makes me feel I have an elder sister:
Zarin Tasnim

Acknowledgments

As the two year journey to my MS comes to an end, it is time to reminisce and thank the wonderful group of people that I have had the opportunity to meet here at Logan, Utah.

Firstly, I would like to express my deepest gratitude and appreciation to my advisor Dr. Zeljko Pantic. I can fondly remember hours of very interesting discussion on resonant systems, magnetics and power electronics in his office. Special thanks Dr. Regan Zane, who created a wonderful research laboratory at UPEL (Utah State University Power Electronics Laboratory). UPEL is equipped with state of the art facilities to research on power electronics and its application areas. I would further like to thank my honorable committee member Dr. Rajnikant Sharma and professor Dr. Reyhan Baktur for their help and guidance. Also, thanks to Mary Lee Anderson for her guidance through the administrative process.

I would like to thank my colleagues at UPEL: Tuba Yilmaz, Tarak Saha, Hongjie Wang, Ryan Bohm, Isaac Cocar, Kelly Hathaway, and Thomas Amely. I would like to specially thank my colleague Weilun Warren Chen. I will always remember those discussions with Warren on a multitude of topics in power electronics: control of power converters and many many practical details of making power converters.

In addition, I would like to thank all my friends at Logan who made my stay an enjoyable experience. Thanks to Sazib and Shante, Asiful Ghani, Abdur Razzaq, Sonia Binte Murshed, Andre, Parvez and Sumi, Ababil, Mehedi, Towfiq, and Zia.

Finally I would like to thank my parents Dr. Md. Alauddin and Kumrun Nahar Chawdhury, who have always stood by me and believed in me, celebrated my victories, and were the my rock of encouragement in tough times. I cannot thank you enough. Also thanks to my little sister Zarin Tasnim.

Nazmul Hasan

Contents

List of Tables

List of Figures

Acronyms

BPSO	Binary Particle Swarm Optimization
EV	Electric Vehicle
HPSO	Hybrid Particle Swarm Optimization
HEV	Hybrid Electric Vehicle
ICPT	Inductively Coupled Power Transfer
IPT	Inductive Power Transfer
LPT	Laser Power Transfer
MATLAB	Matrix Laboratory
MOPSO	Multi Objective Particle Swarm Optimization
PHEV	Plug-In Hybrid Electric Vehicle
PP	Parallel-Parallel Compensation
PS	Parallel-Series Compensation
PSO	Particle Swarm Optimization
SS	Series-Series Compensation
SP	Series-Parallel Compensation
UPEL	Utah State University Power Electronics Laboratory
WCPT	Wireless Capacitive Power Transfer
WEH	Wireless Energy Harvesting
WIPT	Wireless Inductive Power Transfer
WPT	Wireless Power Transfer

Chapter 1

Introduction

1.1 Wireless Power Transfer

At the start of the industrial age, power was generated and transferred in a mechanical form: either heat or rotating kinetic energy [1]. The devices of power transmission were also mechanical: gears, drive shafts, hydraulic connections, pneumatic connections, etc. With the advent of electrical machines in the 19th century, electrical power demand surpassed the mechanical counterpart by virtue of its superior transfer capability. While the mechanical power is not possible to be transferred to long distances, the electrical power can be transferred to long distances using conductive power lines [2,3]. This advantage has made power transfer synonymous with electrical power transmission.

In recent years, there has been a move towards eliminating the cable to make the power transfer even more flexible. There are applications where the use of cables can be very inconvenient, if not impossible; for example: transcutaneous applications [4,5]. Also, in some applications, removing the wire can give extra degree of freedom, e.g. charging applications in electric vehicles or consumer electronics [6,7]. With the advent of wireless communication, consumer has become accustomed to wireless transmission of information and data. Still, there is one wire in a wireless electronic gadget: the power supply cable. If that cable can be eliminated, only then can the devices be truly wireless.

The scope of this thesis is wireless power transfer applied to in-motion electric vehicle charging. In the rest of this chapter, different wireless power transfer mechanisms are introduced [8–23]. At the end of the discussion, it becomes evident that inductive transfer is the only viable option for vehicle charging. This thesis addresses issue of optimum design of inductive couplers based on analytical modeling techniques. While stationary electric vehicle charging has generated a wide range of interests and applications in recent years,

in-motion charging has not yet gained momentum in terms of practical applications. This thesis explains the issues associated with the novel architecture of lumped primary transfer coils and proposes a novel solution of the problem, which is introduced in the last part of the introduction.

1.2 Classification of Wireless Power Transfer Systems

Essentially, electrical power transfer employs electromagnetic waves to transfer energy. Electromagnetic waves are best described by Maxwell's equations. Maxwell's equations state that an electric field of time varying nature can create a magnetic field of the same nature. Again, a time varying magnetic field can create a time varying electric field. In essence, one can create another and they can propagate without any particular source, a phenomena widely used in wireless communication. The discussion gives the impression that power can be transferred to very long distances as well! The caveat is that the field strength drops with distance, being inversely proportional in the near field and square inverse proportional in far field. Thus the only way to transfer appreciable amount of power is to transfer in near field. In far field, low power energy harvesting applications are possible. There is a special class of coherent wave, LASER, which is capable of transferring significant amount of power; but it is highly harmful to human health. In the following discussion, different types of wireless power transfer techniques are explained briefly, which establishes the fact that inductive power transfer is the most suitable option among wireless power transfer technologies for electric vehicle charging application.

1.2.1 Different Wireless Power Transfer Technologies

This subsection lists the classification of wireless power transfer systems. The broad categories of near-field and far-field energy transfer can each be subdivided into more categories.

- Near Field Wireless Power Transfer

    1. Wireless Inductive Power Transfer (WIPT)

2. Wireless Capacitive Power Transfer (WCPT)

- Far Field Wireless Power Transfer

    1. Wireless Energy Harvesting (WEH)

    2. Microwave Power Transfer (MPT)

1.2.2 Near Field Wireless Power Transfer

Distance inside one wavelength of radiation is called near field radiation (Fig. 1.1). Inside this region, electric or magnetic field can exist without the presence of the other, with a source creating them. This region is also called the reactive region, as any change in the load is reflected back to the source. This region is suitable for high power transfer, as the field strength does not drop substantially within this region. The shielding of electromagnetic field from public exposure is also possible within this region. This makes near field techniques ideal for power transfer applications. Based on the field of power transfer, techniques can be divided into inductive and capacitive techniques.

Wireless Inductive Power Transfer (WIPT)

Inductive power transfer [24] uses magnetic field to transfer power over a short range. It is the most popular technology of wireless power transfer and has found wide range of applications, including electric vehicle charging, material handling systems, consumer electronics, biomedical implants, underwater power delivery systems, and many more. A typical block diagram of these systems is presented in Fig. 1.2. Low frequency AC power from the grid is converted to high frequency AC, which is suitable for driving the resonant coil. The conversion usually takes two stages: first stage is an AC-DC (Rectifier) converter, followed by a DC-AC (Inverter) converter. The high frequency current which flows through the coil creates a high frequency magnetic field according to Ampere's Law. The secondary coil cuts this magnetic field and a voltage is induced according to Faraday's Law of Induction. Both primary and secondary coils are compensated through resonant networks. Primary
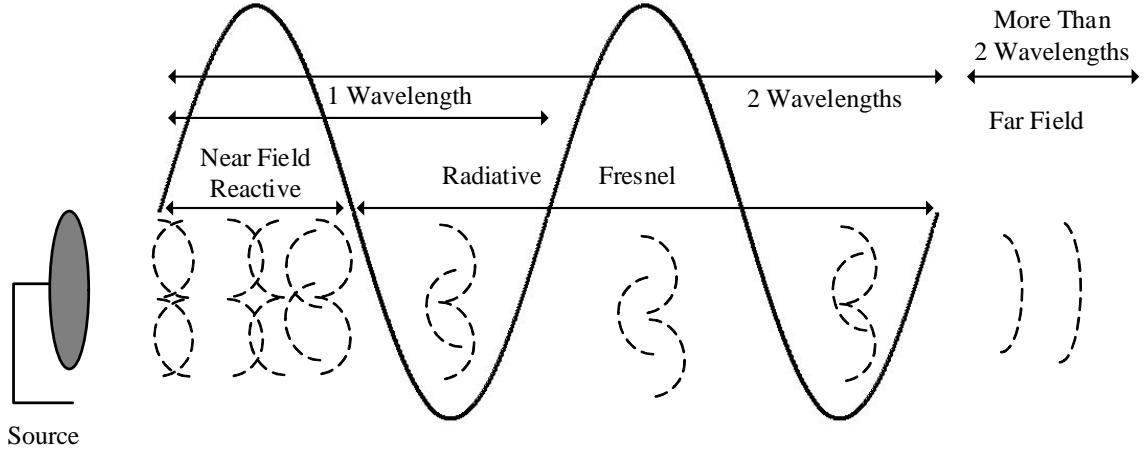
Fig. 1.1: Representation of near and far field wave.

compensation network improves the power quality in the primary while the secondary compensation network increases the power transfer. The high frequency AC voltage at the secondary is again conditioned by secondary side converters for appropriate loads.

Wireless Capacitive Power Transfer (WCPT)

Contrary to WIPT systems, capacitive power transfer [25] uses electric field to transfer power. While similar types of converters and compensation techniques are used in both transmitter and receiver sides [8–12], the wireless section is radically different. A typical block diagram is given in Fig. 1.3. The fundamental principle of WCPT system is as follows: a time varying voltage in capacitor plates creates a displacement current in the dielectric ensuring the current continuity. WCPT systems have a few advantages over WIPT
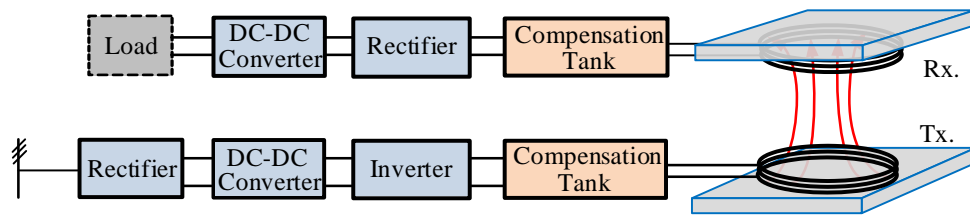
Fig. 1.2: Wireless inductive power transfer system©[2015] IEEE.
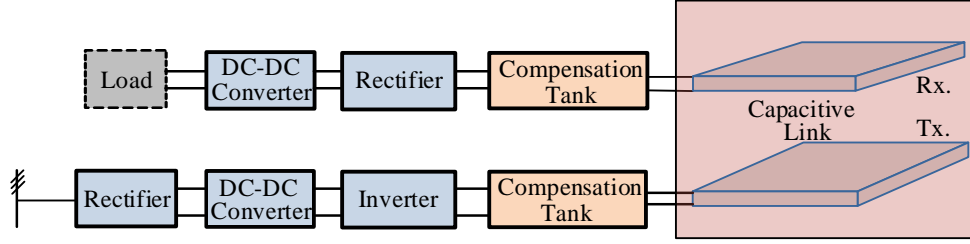
Fig. 1.3: Wireless capacitive power transfer system.

systems. Firstly, as the power transfer medium is electric field, power transfer continues even in the presence of metal barriers, contrary to WIPT systems. The reason behind is the well documented fact that magnetic fields cannot penetrate metal object. Secondly, EMI containment is relatively easy, as most of the electric field is contained within the gap. On the other hand, WCPT systems suffer from low efficiency at lower frequency and low power transfer capability [26].

1.2.3 Far Field Wireless Power Transfer

Regions in which distances are greater than two wavelengths of the electromagnetic wave are called far field regions as shown in Fig. 1.1. The strength of the field is lower in this region, as it drops with square of the distance. Thus, a typical electromagnetic wave is incapable of transferring high amount of power across this comparatively large distance. But, there are special techniques and applications for wireless power transfer in far field [13–15, 27], two of which will be discussed in the following text.

Microwave Power Transfer (MPT) and Laser Power Transfer (LPT)

In a traditional communication antenna, most of the energy do not reach the load because of the low directivity of the system. Enhancing the directivity of the electromagnetic wave by using higher frequency signals in microwave range, significant amount of power transfer is possible. This phenomena was introduced in seventies [13] and later demonstrated experimentally [14]. Specifically designed coherent sources can amplify the electromagnetic

radiation and transfer it very precisely to long distances. The technology is named LASER (Light Amplification by Stimulated Emission of Radiation [28]), and the power transfer technique is called Laser Power Transfer (LPT) [27]. However, both MPT and LPT can be fatal to human health, due to large amount of energy stored in condensed electromagnetic waves, thus these technologies are limited to applications with minimum human exposure [15].

Wireless Energy Harvesting (WEH)

Wireless energy harvesting is a rapidly growing field [29]. WEH explores tecniques to harvest energy from information-carrying electromagnetic waves for powering small devices like sensors. Wireless sensors have energy storage, which makes them bulky and non-autonomous. By extracting energy out of the communication electromagnetic waves, it is possible to power the battery sensors and thus reduce the battery size or eliminate it. Fig. 1.4 shows the block diagram of a typical WEH system.

1.3   Design of WIPT Systems

Although larger coils with higher number of turns possess superior coupling coefficient and thus greater power transfer capability, they suffer from lower efficiency. The reason behind is the presence of parasitic effects in ac resistance, i.e. the skin effect and proximity effects and the parasitic capacitance formation between nearby turns. These result in higher values of ac resistance and consequently higher quantity of loss with the increase of number
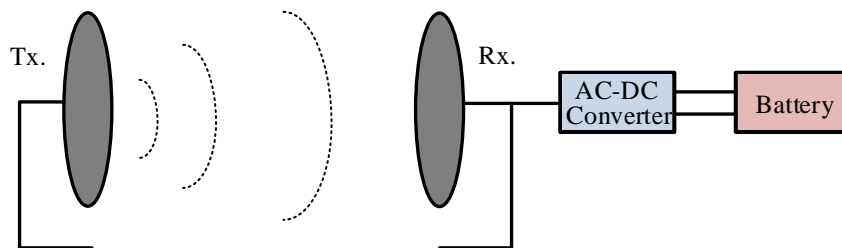
Fig. 1.4: Wireless energy harvesting system.

of turns. This reasoning leads us to believe that a comprehensive design approach taking all the parameters into account is of paramount importance in finding the most efficient inductive link design. In recent times there have been a few works on optimizing inductive link designs for vehicle applications [30–38], but there are scopes of significant improvement in terms of more accurate modeling and comprehensive nature of optimization.

Thus there are two major branches of the design question: firstly, the accurate modeling of inductive link parameters; secondly, the comprehensive optimization of the design variables. The design procedures presented thus far ignore some important parameters [30–38], i.e. resonant capacitor ESR, which can be major sources of loss. Again, the modeling of components often includes finite element simulation tools, which can make the computations time consuming as well as computationally challenging. This thesis looks at analytical modeling techniques, which can accurately model parameters such as coil inductance, coil parasitic resistance, and resonant capacitor ESR. All system components, including all possible loss mechanisms, are modeled comprehensively. These are: coil AC resistance, the ESR of the resonant capacitors, the series resistance of the inductors, and parasitic capacitance formed between adjacent turns of a coil.

The design of WIPT system includes choice of seven to ten parameters, and the complex relationship among them makes it impossible to formulate analytical formulation of the best choice. The design procedures presented thus far have lacked the comprehensive nature required to solve this problem [30, 31, 33, 35, 36, 39]. Thus, there is a need for exhaustive search in the whole space, meaning, all possible combinations should be tested and the most efficient solution should be chosen. There are also other important design considerations such as the output voltage of the inverter, the system VA rating, and the inverter VA rating are a few among them. This design procedure can be time consuming and computationally demanding. In light of the huge time and computational expense, this thesis explores stochastic metaheuristic algorithms as a possible alternative to these brute force search approaches. These algorithms give the option to intelligently search for the best solution without the need for evaluating all the possible solutions. Particle Swarm

Optimization (PSO) proposed by Kennedy and Elbert in 1995 [40] is immensely popular in solving engineering optimization problems due fast speed of convergence. The approach is also proved to be reliable [40]. Thus, this thesis explores two design procedures: the exhaustive search algorithm and the particle swarm optimization.

1.4 Power Transfer Synchronization Problem in Lumped Primary Coil Structures

While the dimensions of a WIPT system receiver coil are restricted by the vehicle size, two distinctive designs have been adopted for the transmitter coil: distributed elongated track and series of independent lumped coils. Distributed elongated tracks of various lengths and structures have been employed in designs presented in [18–21]. While energized, the track provides continuous and nearly constant power to a vehicle moving over and along this track. Long tracks present a significant amount of inductance and parasitic resistance. Therefore, these systems have very high VA ratings and limited efficiency, ranging from 70% to 80% although equivalent stationary WPT systems of similar power per pad are reported to achieve the efficiency of over 90% [41]. In dynamic wireless power transfer systems with lumped primary coil structure, one coil at a time is involved in power transfer, and the entire inductance of the primary coil contributes to it by increasing the mutual coupling between the coils. Energized in a timely manner, these coils can deliver power more efficiently than the elongated track, at the same time reducing the coil voltage stress and eliminating the need for distributed series compensation. However, efficiency improvement is only observed when the two coils are aligned. When coils are misaligned, both transferred power and efficiency are greatly reduced.

From the discussion above, two conclusions can be drawn: a) lumped coils acting as transmitter coils can provide higher power transfer efficiency only if they are inactive most of the time and energized only when the vehicle with the receiver is above the particular transmitter coil. For example, a 0.5 m receiving coil of a vehicle moving at the speed of 18 km/h would be exposed to identical transmitting coil for less than 150 ms. Moreover, the time of strong alignment would be just a fraction of that interval. This time becomes

even shorter if the vehicle is laterally misaligned with respect to the transmitter coil position. Thus there are two challenges in dynamic charging of EVs: accurate vehicle position detection and reporting of that position to the charger in a timely manner. Some means of position detection and wireless communication (for example Global Positioning System (GPS) [42] and Dedicated Short Range Communication (DSRC) [43], can be considered to help in providing timed energizing of the transmitter coil. In that case, vehicle should continuously update its position and inform the charger about it. The charger would use the information to determine the most suitable voltage and timing needed to energize the coil and deliver power. Although seemingly simple, this approach introduces some implementation issues, increases the cost and reduces the reliability of the system.

In this thesis, we propose a new method, not requiring any vehicle position detection devices, and completely eliminating or significantly lowering the wireless communication requirements between the two WPT subsystems. The method relies on the understanding of power delivery profiles and intelligent control of the primary track current to maximize energy efficiency performance index. We suggest control over the voltage that energizes the resonant circuit. That way, the reference of the voltage will be continuously updated according to the measured power transferred to the receiver. The relation between voltage reference and measured power is determined off-line to maximize the energy efficiency parameter, and stored in a form of a look-up table inside the controller. The method exclude position detection devices.

1.5 Thesis Outline

This thesis is divided into two main parts: first part addresses the problem of optimized design of inductive power transfer systems and the second part deals with the control of power transfer. Chapter 2 describes the analytical modeling techniques to get the electrical parameters of the coil and the associated compensation tanks. Chapter 3 describes novel optimized design techniques. Chapter 4 presents comprehensive analysis on the synchronization problem of in-motion wireless power transfer in lumped coil structures. Chapter 5 presents sensorless control of power transfer without synchronization sensors. Chapter 6 is

the conclusion which outlines future work directions.

Chapter 2

Modeling of Wireless Inductive Power Transfer System Components

Meticulous modeling of wireless inductive power transfer systems is essential for accurate design of these systems. A closer inspection of WIPT systems reveal that these systems have an inductive link as a central part, with power electronic converters conditioning the power at both sides. Thus, modeling of WIPT systems indicate modeling of the inductive link. The modeling approaches presented thus far have inadequacy in one of the three aspects: a) they require the use of computationally costly 3D FEM tools for accurate modeling, b) most design approaches ignore the high-frequency effects of the coil current and c) resonant capacitor ESR is not adequately modeled, which can be a significant source of loss. This chapter introduces analytical modeling of all electrical parameters of a WIPT systems (i.e. inductance, resistance, capacitance), from the geometric parameters (i.e. number of turns, radius of coil, thickness of wires etc). Coil modeling includes the calculation of inductive and resistive parameters. Inductive parameters are self- and mutual inductances of the coil. WIPT systems operate at VLF and LF frequency range, which gives rise to parasitic AC resistance effects such as skin and proximity effects. Quantitative formulations for the calculations of these effects are given in this chapter. Finally, widely used compensation configurations are explained.

2.1 The Inductive Link in WIPT Systems

A block diagram representing a WIPT system is presented in Fig. 2.1 with highlighted inductive power transfer subsystem. The inductive power transfer subsystem consists of coils and associated compensation capacitors. Design of a WIPT system essentially means design of an inductive link, as converters at both sides can be designed using well established

converter design procedures. The design of an inductive link includes proper modeling of electrical parameters as a function of geometric parameters. The coil modeling includes the modeling of inductive parameters, self- and mutual inductances, the coil capacitance and coil parasitic resistances. Modeling of resonant capacitor ESR is an important aspect of highly efficient systems. Selection of proper compensation topology is also a critical aspect of the design process. These parameters are summarized below, and the following sections presents the analytical modeling procedure of these parameters.

- Modeling Coil Parameters

    - Coil Self-Inductance

    - Coil Mutual Inductance

    - Coil Capacitance

    - Coil Equivalent Circuit

- Modeling Resonant Capacitor ESR

- Compensation Topologies

2.2 Modeling Coil Parameters

Central part of a WIPT system is a set of coupled coils, which transfers power from primary to secondary by means of high frequency magnetic field. The physical parameters
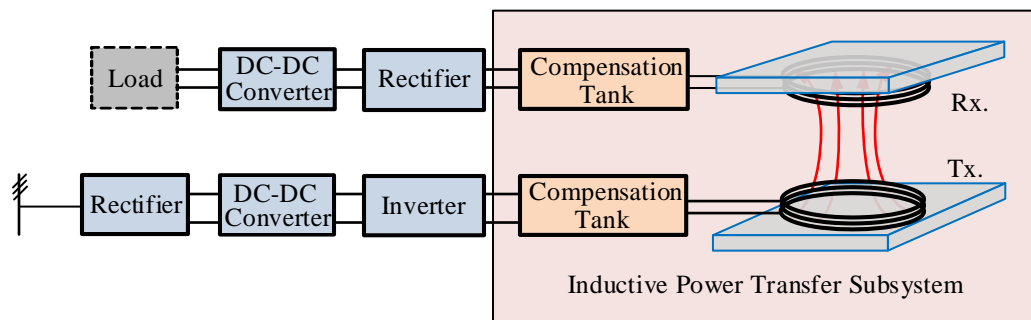
Fig. 2.1: Inductive power transfer subsystem.

are geometric parameters, e.g. coil diameter, number of turns, distance between primary and secondary etc. But, for the calculation of circuit variables (voltage and current) one needs circuit parameters (inductance, capacitance, etc.). The electrical parameters include the self- and mutual inductance. The self-inductance determines the VA rating of the coil and inverter. Mutual inductance determines the power transfer with higher mutual inductance corresponding to more transferred power. The loss in the coil is generated by the parasitic resistance. Although Ohm's law can predict coil resistance in DC very accurately, the coil resistance increases substantially in high frequency AC systems. The principal sources of this escalation are the skin and proximity effects. Accurate modeling of an AC resistance includes these parasitic effects. Finally, though the coils are designed to present an inductive load, the parasitic capacitance alters the inductance values. Parasitic capacitance effects are also modeled in subsection 2.2.2 and the equivalent circuit is developed in subsection 2.2.4.

Knowledge of coil structure is basic requirement for coil electrical parameters modeling. The coil consists of several turns of wire arranged in several layers. A typical cross section of a wire is presented in Fig. 2.2. The inductor is rectangular in its cross section, and inside there are circular cross-section wires. The spacing between wires in vertical and horizontal directions can influence the parasitic resistance. As WIPT systems operate in high frequencies (10-100 kHz), the skin effect is significant. To counter the high frequency effects of current crowding in the outer layer, each wire is actually not a single solid wire, but combination of many thin strands. The strand diameter is typically smaller than the skin depth parameter at the frequency of operation.

2.2.1 Coil Inductance

This thesis considers only circular coils. Although other coil geometries are possible, circular coils provide the most uniform mutual inductance, meaning the inductance decreases at a smooth rate, contrary to rectangular coils [22]. Thus this particular geometry of coil is favored by industry for future electric vehicle application. A Litz wire based circular coil can be treated as a collection of concentric circular loops. Thus, the central part of
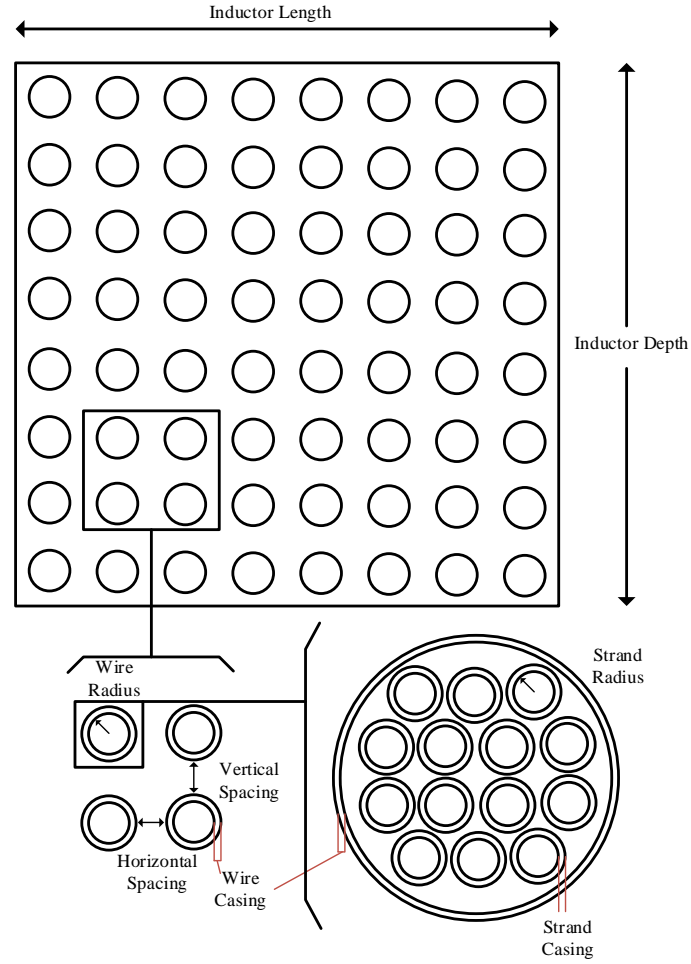
Fig. 2.2: An illustration of coil cross-section and a Litz wire structure.

the inductance calculation is the calculation of inductance of two concentric circular loops, illustrated in Fig. 2.3. Neumann's formula, (2.1), gives the inductance of two concentric circular coils.

$$M_{ij} = M_{ji} = \frac{\mu_0}{4\pi} \oint \oint \frac{dl_i \cdot dl_j}{|x_i - x_j|} \tag{2.1}$$
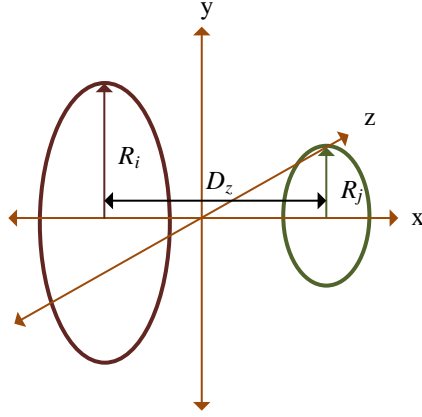
Fig. 2.3: Concentric circular loops in Neumann's formula.

$$a = \frac{R_i^2 + R_j^2 + D_z^2}{R_i^2 R_j^2}$$

$$b = \frac{2}{R_i R_j}$$

$$\beta = \sqrt{\frac{2b}{a+b}}$$

$$M_{ij} = 2\mu_0 \frac{\sqrt{a+b}}{b}[(1 - \frac{\beta^2}{2})K(\beta) - E(\beta)] \tag{2.2}$$

Solving (2.1), we get (2.2). A closer look at (2.2) reveals that it has elliptic integral inside the formula, which cannot be calculated analytically. But, MATLAB provides functions which can calculate the numerical value of elliptic integrals. Thus, this formula can be easily implemented in the MATLAB environment. Meaning of the symbols used in the equations is explained below:

R_i = radius of the i-th loop.

R_j = radius of the j-th loop.

D_z = vertical distance between two loops.

$K(\beta)$ = elliptic integral of first kind.

$E(\beta)$ = elliptic integral of second kind.

a, b, β are constants derived from the geometric variables, the calculation process is given below.

Coil Self-Inductance

The self-inductance of a coil is summation of inductances of all loops in the coil and the mutual inductance of loops of the coil itself. Self-inductance of i-th loop is L_i; the mutual inductance between the m-th and the n-th loop is denoted as $M_{n,m}$. D_i stands for the coil loop diameter, while the wire cross section diameter is denoted by OD.

$$L_i = \frac{1}{2}\mu_0 D_i \ln \frac{D_i}{OD} \tag{2.3}$$

$$L_{self} = \sum_n \sum_m M_{n,m} + \sum_i L_i \tag{2.4}$$

Coil Mutual Inductance

Coil mutual inductance is the summation of all mutual inductances between turns of different coils. Each coil may have more than one layer and each layer has a certain number of turns associated with it. $N_{l,p}$ stands for the number of layers in primary, $N_{tl,p}$ stands for the number of turns per layer in primary, $N_{l,s}$ is the number of layers in secondary and $N_{tl,s}$ is the number of turns per layer in secondary. Equation (2.5) presents calculation of mutual inductance between two coils by aggregating mutual inductances between loops, one being at the primary, and one at the secondary.

$$M = \sum_{i=1}^{N_{l,p}} \sum_{j=1}^{N_{l,s}} \sum_{k=1}^{N_{tl,p}} \sum_{l=1}^{N_{tl,s}} M_{ik,jl} \tag{2.5}$$

2.2.2   Coil Capacitance

Although an inductive coil is designed to be an inductor, there are several parasitic phenomena which generate capacitive behavior in the system, as reported in [44, 45]. Capacitance mainly comes from two sources:

- wire insulation, shown in Fig. 2.4

- air gap between two adjacent wires, shown in Fig. 2.5

If we consider a wire conductor as a capacitor conductor, then the insulation of the wire can be considered as the capacitor insulator. Thus, we easily get a capacitor structure in the coil. This coil capacitance per unit angle is given in (2.6), as calculated in [44, 45]. This capacitance is calculated for only one wire. To complete the capacitor between two adjacent turns, one needs to consider two insulation capacitors in series.

$$\frac{dC_{insulator}}{d\theta} = \frac{\varepsilon_0 \varepsilon_r \pi D_i}{\ln \frac{r_0}{r_0 - \zeta}} \tag{2.6}$$

Fig. 2.5 illustrates the fact that air presents an insulation between two adjacent wire conductors, thus forming a capacitance. (2.7), explained in [44, 45], presents expression of capacitance per unit angle due to air gap. In the following equations, D_i stands for coil cross section internal diameter, D_o stands for the outer diameter, θ is the angle formed in the center of the wire, r_o is the outer radius, ζ denotes the insulation width, ϵ_0 is the air permittivity and ϵ_r is the relative permittivity.

$$\frac{dC_{gap}}{d\theta} = \frac{\varepsilon_0 \pi D_i}{2(1 - \cos \theta) + \frac{h}{r_0}} \tag{2.7}$$

The two capacitances can be considered in series electrical connection. Thus, the total capacitance expression can be calculated by evaluating the integral in (2.8), reported in [44, 45].

$$C_{tt} = \frac{0.5 C_{gap} C_{insulation}}{C_{gap} + 0.5 C_{insulation}} = \varepsilon_0 \varepsilon_r \int\limits_0^{\theta_e/2} \frac{\pi D_i r_0}{\zeta + \varepsilon_r r_0 (1 - \cos \theta) + 0.5 \varepsilon_r h} d\theta \tag{2.8}$$
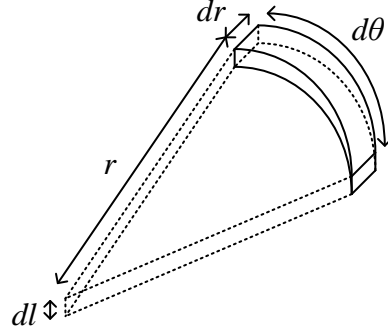
Fig. 2.4: The illustration of a wire insulation.
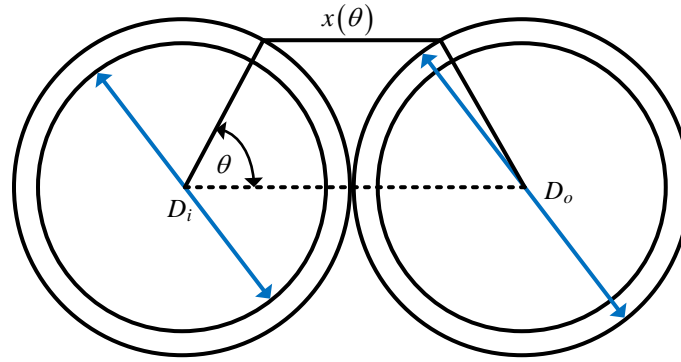
Fig. 2.5: The illustration of an air gap between two wires.

A few steps of the integration are shown below:

$$C_{tt} = \varepsilon_0 \varepsilon_r \pi D_i r_0 \int\limits_0^{\frac{\pi}{4}} \frac{1}{\zeta + \varepsilon_r r_0 + 0.5\varepsilon_r h - \varepsilon_r r_0 \cos\theta} d\theta$$

$$= \frac{a}{p+q} \int\limits_0^{\frac{\pi}{4}} \frac{\sec^2 \frac{\theta}{2}}{1 + \frac{p-q}{p+q} \tan^2 \frac{\theta}{2}} d\theta$$

$$C_{tt} = \frac{2a}{\sqrt{p^2 - q^2}} \tan^{-1}[\sqrt{\frac{p-q}{p+q}} \tan \frac{\theta}{2}]_0^{\frac{\pi}{4}} \tag{2.9}$$

Here, the constants are:

$$a = \varepsilon_0 \varepsilon_r \pi D_i r_0$$

$$p = \zeta + \varepsilon_r r_0 + 0.5 \varepsilon_r h$$

$$q = -\varepsilon_r r_0$$

Once the capacitance between turns is calculated, the next step is to calculate the capacitance of the whole coil. In a coil, a single loop sees two types of turn-to-turn capacitance, one is the capacitance between two turns in the same layer and second is the capacitance between two turns in different layers. C_x can be termed as the capacitance in same layer, while C_y can be termed as capacitance between layers. [4,5] presents equation for the self-capacitance calculation of the whole coil, given the turn to turn capacitance is known. Interestingly, the self-capacitance depends on the direction of wounding the inductor. For a winding type where each subsequent layer is wound in the opposite direction, (2.10) calculates the capacitance, while for a winding type where each subsequent layer is wound in the same direction, (2.11) provides the self-capacitance calculation.

$$C_{self} = \frac{1}{N_t^2} [C_x (N_{tl} - 1) N_l + C_y \sum_{i=1}^{N_{tl}} (2i - 1)^2 (N_l - 1)] \tag{2.10}$$

$$C_{self} = \frac{1}{N_t^2} [C_x (N_{tl} - 1) N_l + C_y N_{tl}^2 (N_l - 1)] \tag{2.11}$$

2.2.3 Coil Resistance

Accurate design of WIPT systems considering efficiency requires knowledge of precise resistance value. First step towards the calculation of accurate resistance is to calculate the wire resistance at DC. (2.12) calculates the DC resistance of a litz wire winding using Ohm's law [4,5]. Here, N_{tl} is the number of turns per layer and N_s is the number of strands in a wire. This formula calculates the resistance of one strand throughout the inductor,

using the arc length formula for l, to take into account the spiraling nature of the inductor.

$$R_{dc} = \rho \frac{l}{A_{con}} = \rho \frac{N_{tl}}{N_s \pi r_s^2} \sum_i \sqrt{4\pi^2 R_i^2 + h_x^2} \tag{2.12}$$

AC resistance due to skin effect can be calculated by the first order approximation of Bessel function, when the conductor radius is smaller than skin depth. When the conductor radius is smaller than or commeasurable to skin depth, AC resistance can be calculated using first order approximation of bessel function. The expression of power dissipation from skin effect is already given in literature [46, 47] and is shown in (2.13); where r_s is the radius of a single strand, R_{DC} is the DC resistance and δ is the skin depth. $\delta = \sqrt{2/\mu_0 \sigma \omega}$, μ_0 and σ being the permeability and conductivity of the conductor respectively.

$$R_{SK} = R_{DC}[1 + 0.021(r_s/\delta)^4] \tag{2.13}$$

Proximity effect induced power dissipation in a single strand is given by (2.14), as explained in [46, 47]. Here, H_{peak} is the peak field through one strand. Adding the power dissipation of all strands, the total power dissipation in a winding due to proximity effect is calculated in (2.15). Here, $A_{winding}$ is the area of the cross section and η is a calculated parameter dependent on the coil geometry.

$$P_{PRO} = \frac{\pi^3 r_s^4 \mu_0^2 \sigma f^2}{2} H_{peak}^2 \tag{2.14}$$

$$P_{PRO \cdot wind} = \frac{\pi^2 r_s^4 \mu_0^2 \sigma N_t^3 N_s I^2 f^2}{8 A_{winding}} \eta(b/t) \tag{2.15}$$

The comparison of the skin and proximity effects is give in (2.16). β is the area efficiency defined by the ratio of the total conducting area over the cross section of the winding. This equation also reveals the fact that the dominant loss mechanism is proximity effect, not the skin effect.

$$\frac{P_{PRO \cdot wind}}{P_{SK \cdot wind} - P_{DC \cdot wind}} \approx 6 \frac{\pi N_t^2 N_s^2 r_s^2}{A_{winding}} \eta = 6 N_t N_s \beta \eta \tag{2.16}$$

The AC resistance of the coil can be derived as shown in (2.17), mentioned in [4,5].

$$R_{ac} = R_{dc} \frac{P_{SK \cdot wind} + P_{PRO \cdot wind}}{P_{DC \cdot wind}} = R_{dc}(1 + \frac{f^2}{f_h^2}) \tag{2.17}$$

where,

$$f_h = \frac{\sqrt{2\sqrt{2}}}{\pi r_s^2 \mu_0 \sigma \sqrt{N_t N_s \eta \beta}}$$

$$\beta = \frac{A_{con}}{tb}$$

$$\eta = \sqrt{\frac{N_t(OD)^2}{tb}}$$

2.2.4 Coil Equivalent Circuit

Fig. 2.6 illustrates a comprehensive equivalent circuit representation of an inductor as well as the simplified version. The L_{eff} is the effective inductance of the coil at a certain frequency and ESR is the equivalent series resistance. (2.18) calculates the self-resonating frequency (f_{self}), which is quite high (several MHz) compared to the typical WIPT system operating frequencies (10-100 kHz). Calculations of L_{eff} and ESR are given in (2.19) and (2.20) respectively.

$$f_{self} = \frac{1}{2\pi\sqrt{LC_{self}}} \tag{2.18}$$

$$L_{eff} = \frac{L}{1 - 4\pi^2 f^2 L C_{self}} \tag{2.19}$$

$$ESR = \frac{L}{1 - 4\pi^2 f^2 L C_{self}} \tag{2.20}$$
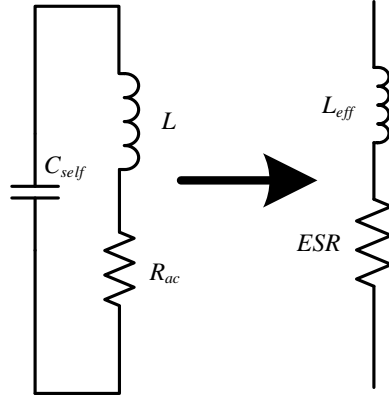
Fig. 2.6: Equivalent circuit of a coil.

2.3 Modeling Resonant Capacitor Parameters

Capacitor modeling includes detailed characterization of capacitor behavior and its representation of in a form of an electric circuit. WIPT systems are essentially high frequency AC current systems. Thus, the capacitor's equivalent series resistance, ESR, of the capacitors is a significant source of loss. An accurate characterization of capacitors is very important. Fig. 2.7 presents a very accurate model of resonant capacitors. ESL is the series inductance of the capacitor. R_p is the parallel resistor which models voltage dependent loss element. R_d and C_d stands for diffusion resistance and capacitance, respectively.

2.3.1 Motivation for Resonant Capacitor ESR Modeling

Resonant capacitor losses can be significant, although they are typically ignored. This subsection investigates losses associated with resonant capacitors analytically. Some plots are generated based on typical parameter values, presented in the later part of this section. These plots show the comparison of losses in resonant capacitors compared to losses in the coils. A close look at different compensation techniques reveals three basic circuit configurations in WIPT systems:

- Series compensation circuit in primary and secondary

- Parallel compensation circuit in primary
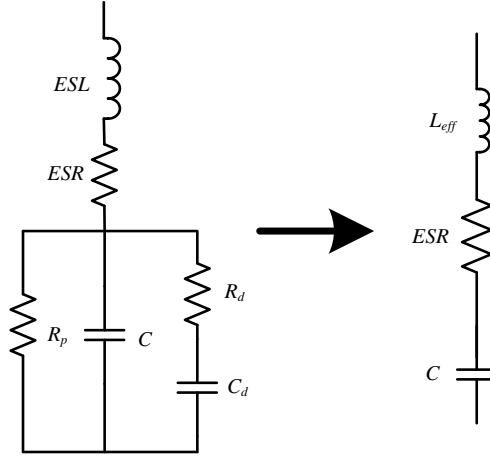
Fig. 2.7: Equivalent circuit of a capacitor.

- Parallel compensation circuit in secondary

In the following discussion, all three of these circuits are thoroughly analyzed, and loss ratio between inductor and capacitor is formulated.

Series compensation circuit in primary and secondary

Fig. 2.8 illustrates a series compensated coil. The circuit representation of a series compensated coil is the same in both primary and secondary sides. As all the circuit elements are in series, there is only one current flowing through all components. The current is termed as the input current, I_{in}. The formulation of the current is,

$$I_{in} = \frac{V_{in}}{Z_{in}} = \frac{V_{in}}{j\omega L + \frac{1}{j\omega C} + R_{Load}} = \frac{V_{in}}{R_{Load}}$$

The current flowing through the parasitic resistance in the track creates a loss. The losses in track inductance can be calculated as,
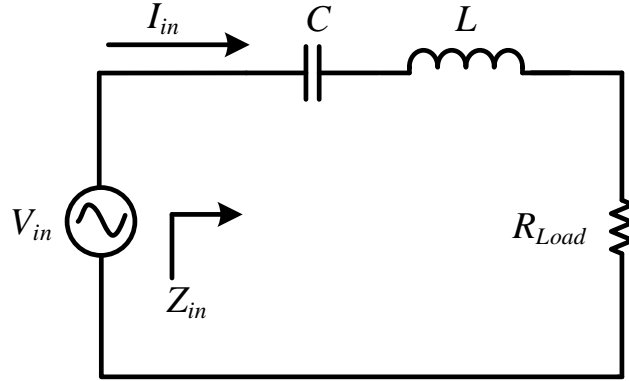
Fig. 2.8: Series compensation circuit for both primary and secondary circuits.

$$P_L = I_{in}^2 R_L = (\frac{V_{in}}{R_{Load}})^2 \cdot \frac{\omega L}{Q_L}$$

Similarly, there will be losses in the resonant capacitor due to its ESR. Loss formulation will be:

$$P_C = I_{in}^2 R_C = (\frac{V_{in}}{R_{Load}})^2 \cdot \frac{\omega C R_C}{\omega C} = (\frac{V_{in}}{R_{Load}})^2 \cdot \frac{1}{\omega C Q_C}$$

Finally, the ratio of losses can be computed as in 2.21.

$$\gamma = \frac{P_L}{P_C} = \frac{(\frac{V_{in}}{R_{Load}})^2 \cdot \frac{\omega L}{Q_L}}{(\frac{V_{in}}{R_{Load}})^2 \cdot \frac{1}{\omega C Q_C}} = \frac{Q_C}{Q_L} \tag{2.21}$$

Parallel compensation in primary

Parallel compensated primary circuit, shown in Fig. 2.9, must be current fed. Thus, an input current I_{in} is assumed to be feeding the resonant tank. The current through the coil inductor is calculated by the current divider rule:
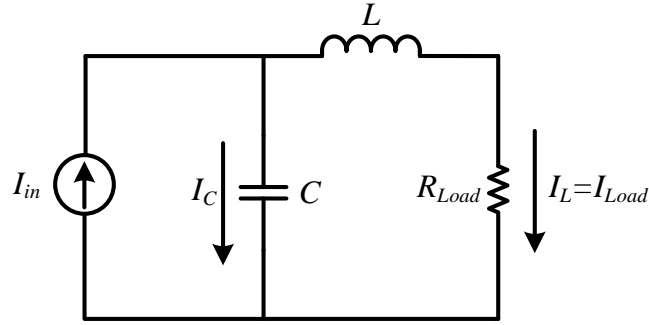
Fig. 2.9: Parallel compensation circuit for the primary.

$$I_L = I_{in}\frac{1/j\omega C}{j\omega L + R_{Load} + 1/j\omega C} = I_{in}\frac{1/j\omega C}{R_{Load}} = I_{in}\frac{1}{j\omega C R_{Load}} = I_{in}\frac{1}{jQ_{Load}}$$

$$\Rightarrow |I_L| = \frac{I_{in}}{Q_{Load}}$$

Same approach can be employed to calculate the current flowing through the capacitor, I_C.

$$I_C = I_{in}\frac{j\omega L + R_{Load}}{j\omega L + R_{Load} + 1/j\omega C} = I_{in}\frac{j\omega L + R_{Load}}{R_{Load}} = I_{in}(\frac{j}{Q_{Load}} + 1)$$

$$\Rightarrow |I_C| = I_{in}\sqrt{1 + \frac{1}{Q_{Load}^2}} = I_{in}\frac{\sqrt{1 + Q_{Load}^2}}{Q_{Load}}$$

The loss in the inductor resistance will be:

$$P_L = I_L^2 R_L = (\frac{I_{in}}{Q_{Load}})^2 R_L$$

Similarly, the losses in the capacitor ESR is:

$$P_C = (I_{in}\frac{\sqrt{(1 + Q_L^2)}}{Q_L})^2 R_C = I_{in}^2\frac{1 + Q_{Load}^2}{Q_{Load}^2} R_c$$

The ratio of losses is:

$$\gamma = \frac{P_L}{P_C} = \frac{(\frac{I_{in}}{Q_{Load}})^2 \times R_L}{I_{in}^2 \frac{1+Q_{Load}^2}{Q_{Load}^2} R_c} = \frac{1}{1+Q_{Load}^2} \frac{R_L}{R_C} = \frac{1}{1+Q_{Load}^2} \frac{Q_C}{Q_L} \tag{2.22}$$

Parallel compensation in secondary

Parallel compensated secondary is a voltage source driven tank shown in Fig. 2.10. The input current is the current through the inductor. Division of the voltage source by equivalent impedance seen by the voltage source gives the magnitude of the input current.

$$I_{in} = \frac{V_{in}}{j\omega L + ((\frac{1}{j\omega C})^{-1} + (R_{Load})^{-1})^{-1}} = \frac{V_{in}}{j\omega L + (j\omega C + \frac{1}{R_{Load}})^{-1}}$$

$$\Rightarrow I_{in} = \frac{V_{in}}{j\omega L + \frac{R_{Load}}{j\omega C R_{Load}+1}}$$

$$\Rightarrow I_{in} = \frac{V_{in}}{j\omega L + \frac{R_Load}{jQ_{Load}+1}}$$

The current division rule is employed to calculate the capacitor current:

$$I_C = I_{in} \frac{R_{Load}}{R_{Load} + \frac{1}{j\omega C}} = I_{in} \frac{1}{1 + \frac{1}{j\omega C R_{Load}}} = I_{in} \frac{Q_{Load}}{Q_{Load} - j}$$

$$\Rightarrow I_C = I_{in} \frac{Q_{Load}}{\sqrt{Q_{Load}^2 + 1}}$$

Power loss in the coil resistance is:

$$P_L = I_{in}^2 R_L$$

Power loss in the capacitor resistance is:

$$P_C = I_C^2 R_C = (I_{in} \frac{Q_{Load}}{\sqrt{Q_{Load}^2 + 1}})^2 R_C$$
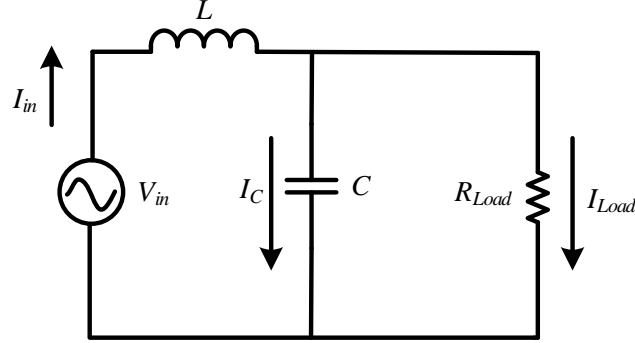
Fig. 2.10: Parallel compensation circuit for the secondary.

The ratio of losses will be:

$$\gamma = \frac{P_L}{P_C} = \frac{I_{in}^2 R_L}{(I_{in}\frac{Q_{Load}}{\sqrt{Q_{Load}^2+1}})^2 R_c} = \frac{R_L}{\frac{Q_{Load}^2}{Q_{Load}^2+1}R_C}$$

$$\Rightarrow \gamma = \frac{Q_{Load}^2 + 1}{Q_{Load}^2}\frac{Q_C}{Q_L} \tag{2.23}$$

Numerical Visualization of the Loss Ratio

Preceding equations present analytical formulations of loss ratio between resonant capacitor and coupling coil for different compensation structures. Although these equations are proper understanding of this ratio for practical systems require numerical visualization of this ratio for different load conditions. A typical quality factor of 500 is considered for coil and while resonant capacitor quality factor is considered to be 1000. The loaded quality factor of WIPT systems range between 2-5. Thus, for this range of load quality factor, loss ratio is plotted for different compensation structures in Fig. 2.11. The total loss ratio will be the product of loss ratio in primary and secondary. This is presented in Fig. 2.12. These figures show higher loss in capacitor than coil for all compensation structures for these typical operating conditions. This is a strong motivation for modeling capacitor losses in the design process of WIPT systems.
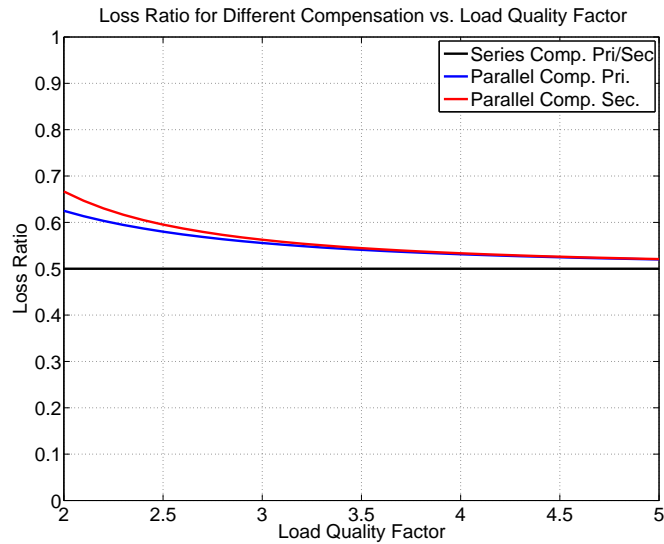
Fig. 2.11: Loss ratio for different compensation structures.

2.3.2 Modeling of Resonant Capacitor ESR

Resonant capacitor ESR varies for different manufacturers, even for different series within the same manufacturer. However, for a certain manufacturer and series, one can formulate a certain function which can predict ESR within an acceptable range. In this research, 940C series manufactured by Cornell Dubilier Electronics (CDE) is considered. A closer look at the ESR in this series reveals exponential increase of ESR for lower values of capacitors. This characteristics is typical for other series and other manufacturers, as well. Fig. 2.13 presents the datasheet values and the modeled curve. Exponential curve fitting is employed for solving this problem and the technique demonstrates very good matching between measured and modeling values.

2.4 Compensation Techniques

A coil can be compensated either in series or parallel. Although in the literature several other types of compensation techniques are reported which involve one or more reactive elements, these two basic compensation techniques are the most popular. These two compensation techniques applied to primary and secondary coils give us four different compensation combinations as shown in Fig. 2.14. Series compensation in the primary has
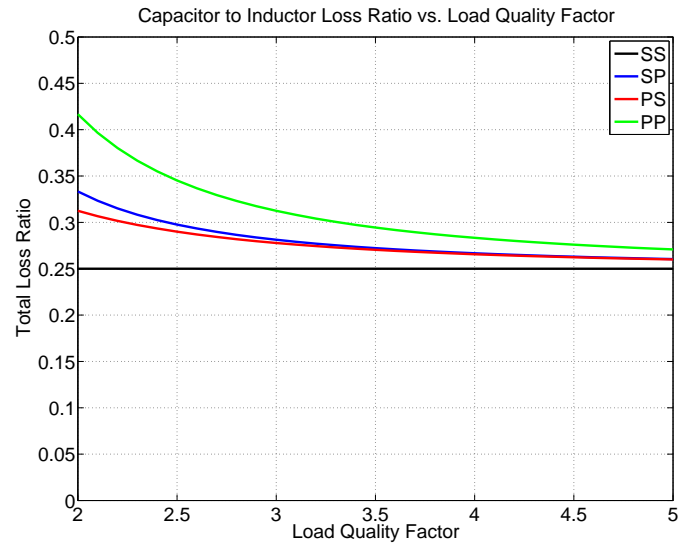
Fig. 2.12: Total loss ratio for different compensation structures.

to be voltage fed. On the other hand, the primary parallel compensation has to be current fed. Series compensation in the secondary boosts the secondary current, while the parallel compensation can boost the secondary voltage. The choice of compensation techniques depend on application characteristics and designer preference.
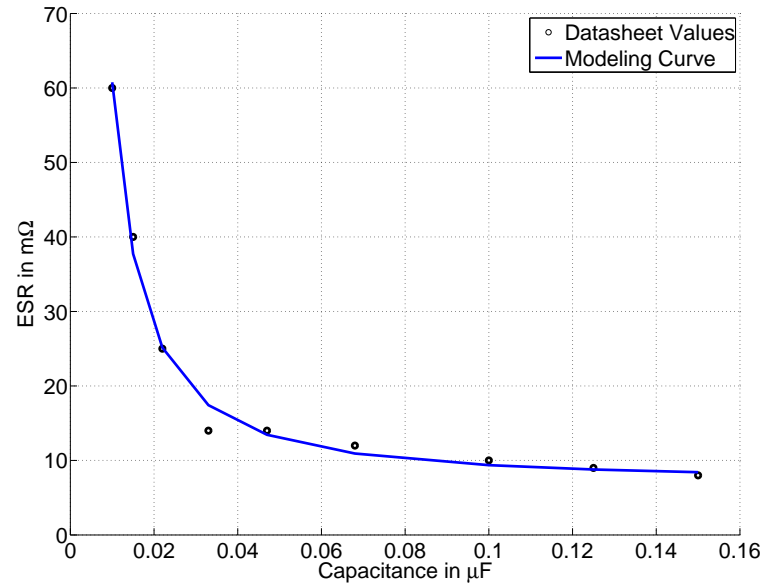
Fig. 2.13: ESR modeling for 940C series capacitors from CDE.
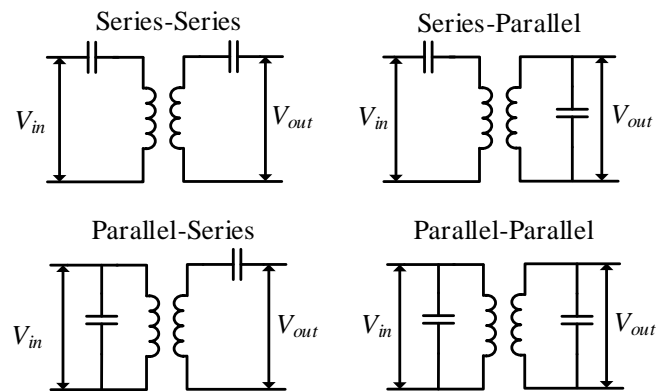
Fig. 2.14: Four major compensation configuration in inductive links ©[2015] IEEE.

Chapter 3

Optimized Design of Magnetic Coupler and Compensation Tank

Optimized design of wireless inductive power transfer systems is an ongoing research question. The proposed designs found in the literature thus far [30–38], have lacked the comprehensive nature required for a highly efficient inductive link design. Moreover, the design of WIPT systems has multiple objectives, which makes the design process more complex. Most of the proposed designs use 3D electromagnetic finite element simulation tools, which are computationally challenging and make the design process complicated.

This chapter introduces two novel design approaches which are comprehensive in terms of modeling system components, independent of designer experience and free from 3D FEM tools. First algorithm is an exhaustive search based algorithm, which evaluates all possible solutions in a solution space and then finds the most suitable design based on a certain set of performance indices. Computational cost associated with an exhaustive search is reduced significantly in the second design approach, which employs a Particle Swarm Optimization technique (PSO)-based design procedure. In the later sections the motivation of the design process is explained by an extensive literature review. Search algorithm is explained and a particular design example is presented. This discussion is followed by an explanation of PSO and by a design example based on PSO.

3.1   Literature Review and Motivation for Design Approach

This section analyzes the major papers presented in literature thus far on the design of WIPT systems and makes critical comments on possible scopes of improvement. Each design procedure has its strong points as well as weak points. The goal of this section is to identify the avenues of advancement, thus enabling the proposal of a sophisticated

algorithm.

Researchers at the University of Auckland, in New Zealand have proposed two different design approaches in [33, 34]. The major deficiencies of these design approaches are: a) it needs experience from the part of designers, b) the designer has to decide on the magnetic structure beforehand, and c) the frequency of operation is fixed. In [31, 35], the authors introduce a new figure of merit that tries to reduce the copper mass of the system. Besides from the fact that the importance of copper mass in the design process is a matter of debate, the design also reaches imprecise conclusions. The analysis indicates that the frequency of operation for maximum efficiency reaches the maximum allowable frequency. This conclusion is only reached due to overlooking high frequency effects of Litz wire AC resistance. Although Litz wires are stranded to negate the parasitic effects on AC resistance at high frequencies, exposure to high frequency still increases the wire resistance significantly. Another set of design procedures in [30, 36], reports analytical formulation of maximum inductance point and maximum efficient points. These formulations ignore the resistive effects of coils at high frequency and also the resonant capacitor ESR, which makes the formulations more tractable as well as less accurate. Moreover, all the design approaches presented thus far neglect the losses associated with resistance in resonant capacitors which can be a significant source of losses in these systems as explained in [38] and also in chapter 2 of this thesis.

In light of the literature review, a number of areas of improvement can be identified in both system modeling, as well as optimization. The major scopes of improvement in modeling can be identified as: a) accurate modeling of wire resistance at higher frequencies, b) precise modeling of resonant capacitor ESR. The design approach presented in light of these previous works, the authors would like to point out the need for exhaustive search in the whole space: meaning all possible combinations should be tested and the most efficient solution should be chosen. There are also other important design considerations like the output voltage of the inverter, system VA rating and the inverter VA rating are a few among them. Thus optimizing the system for one design objective can easily result in

suboptimal performance in terms of other design objectives. The design of WIPT systems consist of optimal choice of five to ten interdependent design parameters, with multiple design objectives. This situation makes the development of analytical design procedures nearly impossible. Thus, the most accurate solution of this problem is to search the whole solution space exhaustively and find the most suitable solution. The first design approach accomplishes this task. Although highly accurate, this search algorithm suffers from substantial time and computational expense. This computational burden can be reduced by intelligent search of this solution space. Stochastic metaheuristic algorithms can intelligently search for the best solution without the need for evaluating all points in the solution space, presenting a very attractive alternative to exhaustive search algorithms. Particle Swarm Optimization (PSO) [40], proposed by Kennedy and Elbert in 1995, is a prominent technique in solving for engineering optimization problems due to fast convergence toward the optimum solution. This thesis also explores this particular optimization algorithm in the design problem of wireless inductive power transfer systems.

3.2 Exhaustive Search Algorithm

Exhaustive search algorithm performs a comprehensive search of the total solution space. The algorithm, implemented in MATLAB, analytically models all components of the magnetic link, as well as its associated parasitic effects analytically. Design of a inductive coil involves choice of the geometric parameters of the coil: wire thickness and number of turns. Accurate knowledge of the search space is necessary to initialize the search.

Wireless inductive power transfer systems usually have an area constraint dictated by the particular application constraints. For example, an electric vehicle like electric car has a certain distance from the bottom of the chassis to the top of the road. This distance determines the distance between primary and secondary coils. The coil dimensions are also dictated by the area of the vehicle. This area requirement can be translated to geometric parameters like number of turns and number of turns per layer in both primary and secondary. There are at least three additional degrees of freedom: frequency, primary wire thickness and secondary wire thickness.

The discussion above gives a guideline to the order of steps in selecting the boundary of design variables. The first step is to choose the frequency of operation, which determines the strand thickness. Wire thickness is determined by both the strand thickness as well as the current rating. The number of turns can be determined by the area and the wire thickness. The steps are listed below:

i frequency of operation (f)

ii thickness (AWG) of wires

iii number of turns per layer at the primary ($N_{tl,p}$)

iv number of layers at the primary ($N_{l,p}$)

v number of turns per layer at the secondary ($N_{tl,s}$)

vi number of layers at the secondary ($N_{l,s}$)

A flow chart of the proposed iterative algorithm is illustrated in Fig. 3.1. The algorithm sweeps through all the six parameters listed above. For every combinations of these six variables, circuit parameters such as inductance, resistance and capacitances are calculated based on analytical formula developed in Chapter 2. Once the circuit parameters are calculated, the circuit variables are solved and the optimum design is chosen based on efficiency as the performance index. Credibility of the algorithm hinges on the accurate prediction of circuit parameter values. In the following section, a design example is presented which verifies the performance of the design.

3.3 A Design Example using Search Algorithm

Early childhood development of children with cognitive disabilities is an ongoing research problem [48–51]. In recent years scientists have proposed interactive robots as an important tool for proper mental growth of children [49,50]. Studies carried out in the Rehabilitation Engineering Research Center for the Advancement of Cognitive Technologies (RERC-ACT) [52] at CU Denver have found the use of interactive robotics beneficial in
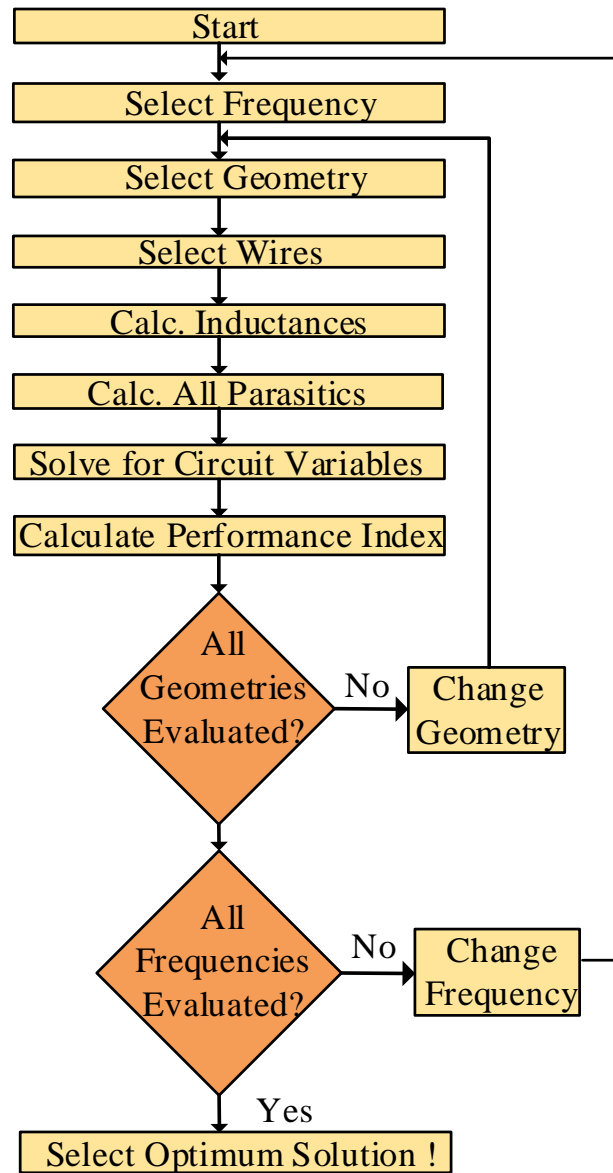
Fig. 3.1: Flow chart of the exhaustive search algorithm ©[2015] IEEE.

several aspects of child development processes. These robots can read children behavior and translate these behaviors to robotic responses such as: move closer, move away, play music and perform a dance like behavior, etc. However, the benefits are dependent on the autonomy of the robot, as human presence during the sessions can be disruptive to this process of robot-child interaction. Robot employed for this project is an m3Pi hobbyist robot platform, whose capabilities are significantly enhanced by adding 2.4 GHz radio communication, sonar, kinetic camera, piezo sound generator, and Wixel communication modules to make it capable of executing complex kinetic and communication tasks. Success of the therapeutic session not only depends on its performances, but the visual appearance of the robot, as well, so a stuffed animal cover, supported by an inside metal construction is used to hide the real robot structure. However, all these additives increase the power consumption of the four AAA batteries that supply the robot, which is turn drastically shortens their operation time between two recharging intervals. Limited energy storage of the robot limits the duration of the sessions and makes human presence necessary when the battery replacement and recharging is needed. Wireless Inductive Power Transfer (WIPT) appears then as the only method for the accomplishment of an automatic and autonomous charging of the robot, and consequently as the only method for reducing distractions to a minimum [53] ©[2015] IEEE.

The proposed search algorithm was employed to design a WIPT system for the socially interactive robot application. As usual, the design constraints are derived from the space constraint of the application. In this case, the space under the robot and the thickness of the table determines the inductive link distance. The receiver coil space is dictated by space under the robot. While the receiver coil is space limited, the transmitter coil is not. The transmitter coil can be increased in both directions, outward and inward turns, increasing the mutual inductance significantly. Table 3.1 lists the geometric constraints of the robot WIPT system.

The search algorithm developed in this thesis is run with the restrictions presented in Table 3.1 as an input to the algorithm. The algorithm outcome is a list of design parame-

Table 3.1: System specifications for the robot WIPT system

Parameter	Value
Length from front wheel to the end of the board	2.7 Inch
Length from wheel to wheel	2.7 Inch
Height from bottom of the robot to top of the table	1.0 Inch
The thickness of the table	0.5 Inch
Rated power	7 W

ters as presented in Table 3.2. This design is implemented in the socially interactive robot platform shown in Fig. 3.3. The total setup consists of a table with a line following track. The robot follows the track to the marked charging spot, and stops there to start the communication with the primary charger. The inductive link is mounted at the bottom of the robot and the bottom of the table surface, as illustrated in Fig. 3.2. The charger establishes a bidirectional communication with the robot to setup a nominal charging condition. Then the charging is started.

Table 3.2: Design parameters for the WIPT system for Robot ©[2015] IEEE

Design Parameter	Value
Operating frequency	40 kHz
Primary coil AWG	12
Number of strands in the primary wire	660
Number of turns per layer at primary	16
Number of layers in primary	3
Secondary coil AWG	18
Number of strands in the secondary wire	100
Number of turns per layer at secondary	11
Number of layers in secondary	1

The verification of the optimization algorithm is essentially the verification of the circuit parameter calculation. Since the correct calculation of the circuit parameters will ensure correct computation of the performance indices resulting in an accurate optimization of the system. The experimental result of the WIPT system parameters conform very closely with the theoretical calculations as presented in Table 3.3.

3.4 Motivation for Exploring an Artificial Intelligence Based Algorithm

This section presents a case study of possible design options in an WIPT design process.

Table 3.3: Experimental results of search algorithm ©[2015] IEEE

Parameter	Simulation result	Experimental result
Primary coil inductance	118.86 μH	119.68 μH
Primary coil resistance	92.2 mΩ	84.3 mΩ
Secondary coil inductance	7.86 μH	7.88 μH
Secondary coil resistance	57.1 mΩ	49.7 mΩ
Mutual inductance	7.45 μH	7.49 μH
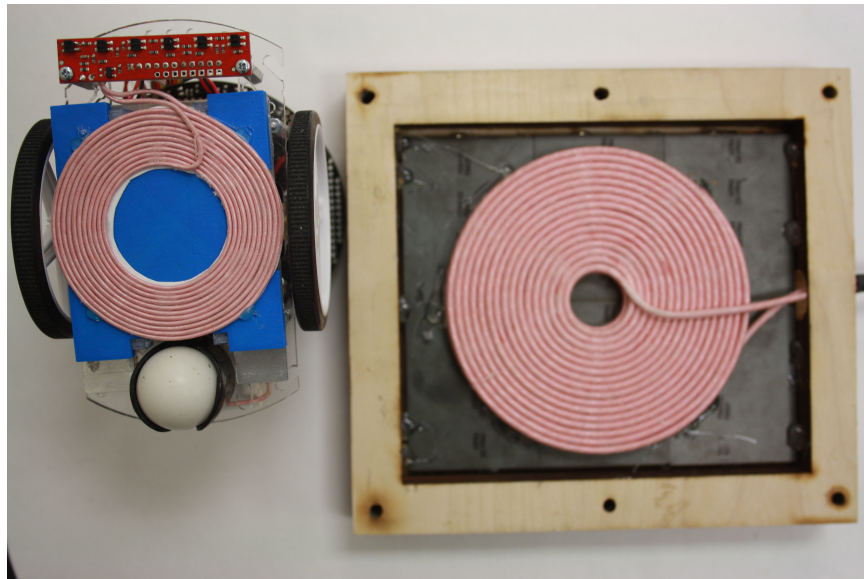
Fig. 3.2: The designed coils implemented in robot.
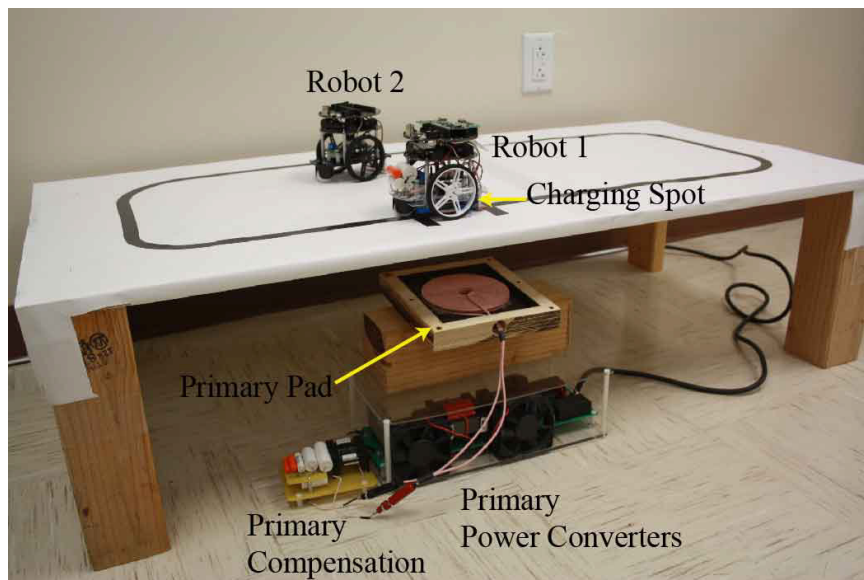
Fig. 3.3: The robot setup with textual explanations ©[2015] IEEE.

A typical electric vehicle coil is selected for the study. We take a 700 mm diameter coil which can be populated by 4 mm diameter wire. The inner turns of a coil contribute to marginal improvement in mutual inductance, as reported in [38]. Thus, the the coil is expected to be populated up to 30% of the outer diameter. This choice makes the maximum possible number of turns to be around 60. Difficulty in wounding a multiple layer coil structure limits the maximum number of layers; a very liberal estimate should be 5. The frequency limit is set by the inverter operating range; a range of 20 to 150 kHz is reported in literature. This gives 130 different frequency options. Thickness of the wire is usually selected based on other design considerations, a pragmatic number is reported in the table below. All the possible combinations are combined in Table 3.4.

Product of the options presented in Table 3.4 is the total number of design combinations. The result of the product is a staggering number of 421200000. It is clearly time consuming to compute the design parameters for all those design combinations. Experienced designers choose a feasible range of operation and then iterate their designs until the most satisfactory result is reached. But, there is always a possibility of choosing a suboptimal design. This justifies the need for a quick and comprehensive search algorithm which searches the whole search space of possible designs and chooses the most efficient one.

3.5   Particle Swarm Optimization

Particle swarm optimization (PSO) algorithm, proposed by Kennedy and Elbert in 1995, is inspired by intelligence of bird flocks or insect swarms. A bee swarm in a garden of

Table 3.4: Design options ©[2015] IEEE

Parameter	Range	Options
Operating Frequency	20-150 kHz	130
Number of turns in Primary	60	60
Number of layers in Primary	5	5
Number of turns in Secondary	60	60
Number of layers in Secondary	5	5
AWG of Primary wire	12-8	6
AWG of Secondary wire	12-8	6

flowers, as in Fig. 3.4, can be taken as an example. If a single bee locates a good source of honey, they have a mechanism to share the knowledge; which consequently draw more bees to the same destination. If the bees are randomly scattered at the outset, identification of the largest source of honey is possible. This mechanism of sharing the knowledge creates a type of shared intelligence for the group, termed as swarm intelligence. Researchers have developed mathematical models for swarm intelligence [54], illustrated graphically in Fig. 3.5 ,enabling application of this phenomena in solving engineering problems. Although there are several other optimization algorithms reported in the literature, Particle Swarm Optimization (PSO) is one of the most widely adopted evolutionary optimization techniques and is reported to converge very quickly.

Swarm intelligence technique can be employed to find the best solution in a particular solution space. Instead of extensively searching the whole solution space by evaluating every point, this algorithm starts with a few random test points spaced apart in the solution space. Fitness values are computed in these test points and based on results, points are assigned for future iterations. More evaluations are carried out closer to the points which have better fitness compared to the points which have worse. This gradual change of search points in new iterations is called evolution and it is the basis of any evolutionary algorithm. After a certain number of iterations, the solution with the best fitness value is reached. In the following subsections, the terminology and mechanism of PSO algorithm is presented in detail.

3.5.1 Classification of PSO Algorithm

PSO is capable of solving a wide variety of optimization problems. According to the nature of the optimization problem, the PSO algorithm can be altered to best match the nature of the problem. Based on fundamental optimization techniques, the algorithm can be divided into three categories: real, binary and hybrid. In terms of objective types, the technique can be classified into single and multiple objective [55].

The three major types of PSO algorithms are introduced below [55].

Fig. 3.4: A bee searching honey - motivation of PSO Algorithm. Courtesy www.beetography.com ©Zachary Huang

.
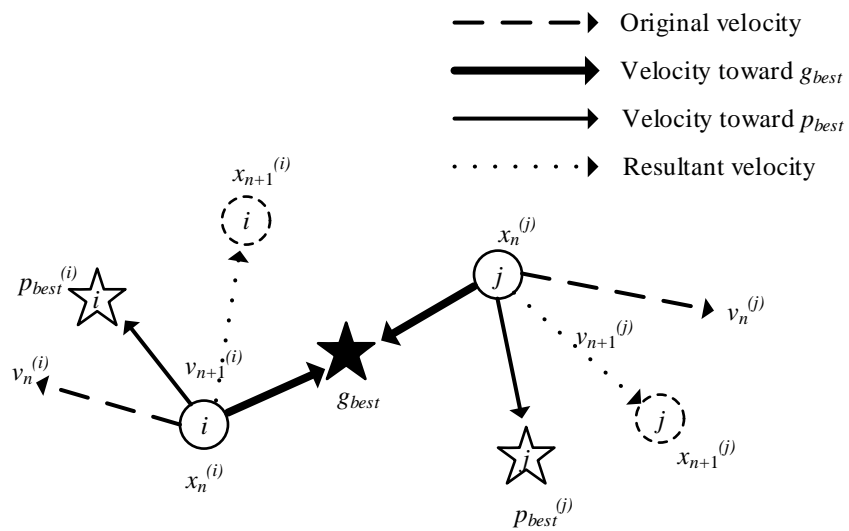
Fig. 3.5: Fundamental mechanism of particle swarm optimization.

- **Real PSO (RPSO)**: This type of PSO optimization searches through a search space consisting of real valued parameters. A WIPT system geometry is an apt example for this type of optimization, where the optimization algorithm chooses a set of real valued design parameters.

- **Binary PSO (BPSO)**: This type of PSO optimization selects the optimum choice from a search space consisting of a certain set of discrete choice options. Choice of compensation configuration is a typical example of this type of optimization.

- **Hybrid PSO (HPSO)**: Optimization problems which have characteristics of both binary and real valued optimizations are solved using Hybrid PSO, HPSO. WIPT system solution requires hybrid PSO approach as it involves both choice of compensation techniques and also selection of coil geometrical parameters.

The optimization objective can be either single or multiple. Single objective optimization has only one design criteria and the system is optimized to achieve the maximum performance with reference to that particular design objective. On the other hand, a multiple objective optimization optimizes more than one design criterion.

3.5.2   PSO Terminology

PSO terminology is introduced in this subsection. PSO is a sophisticated technique and the mathematical variables are aptly described by a certain established jargon. This terminology is introduced in this subsection and will be used in this thesis without any further explanation [55].

- **Agent**: Each individual bee in the swarm is referred to as an agent. Each agent constantly updates its position to be closer to the local best and global best position in every iteration.

- **Position:** Position refers to an agents place in the field. If the solution space is N dimensional, then its position is also an N dimensional quantity.

- **Fitness:** There needs to be a criterion to judge the merit of a particular solution or position of an agent. In evolutionary algorithms this criterion is called Fitness function. For example, in a WIPT design problem, efficiency of the IPT link can be a fitness function.

- **Personal Best (p_{best}):** Each particle remembers the position of the best fitness value discovered by that particle. If a position having a better fitness value is identified by the particle, then the p_{best} is replaced by the new position.

- **Global Best (g_{best}):** The position which gives the best fitness in the whole swarm is remembered by all the agents in the swarm. This position is called the global best position. Identical to p_{best} update procedure, the g_{best} is updated as soon as a position with better fitness than the current g_{best} is spotted.

3.5.3 Newtonian Mechanics Model of RPSO

The mathematical modeling of PSO is based on Newtonian Mechanics [55]. Assuming the solution space is N-dimensional real vector, then for each agent with mass m, its time varying position and velocity can be expressed following Newton's second law as:

$$\frac{d\overrightarrow{x}}{dt} = \overrightarrow{v} \tag{3.1}$$

$$\frac{d\overrightarrow{v}}{dt} = \overrightarrow{a} = \frac{\overrightarrow{F}}{m} \tag{3.2}$$

Here, $\overrightarrow{F}$ is the force on the agent, $\overrightarrow{a}$ stands for acceleration and $\overrightarrow{v}$ symbolizes speed. In order to formulate an iterative process, (3.2) is simplified to the form of (3.4).

$$\frac{\overrightarrow{x}_t - \overrightarrow{x}_{t-1}}{\Delta t} = \overrightarrow{v_t} \Rightarrow \overrightarrow{x_t} = \overrightarrow{x}_{t-1} + \overrightarrow{v_t}\Delta t \tag{3.3}$$

$$\frac{\overrightarrow{v_t} - \overrightarrow{v}_{t-1}}{\Delta t} = \frac{\overrightarrow{F}_{t-1}}{m} \Rightarrow \overrightarrow{v_t} = \overrightarrow{v}_{t-1} + \frac{\overrightarrow{F}_{t-1}}{m}\Delta t \tag{3.4}$$

Convention of PSO literature dictates mass of the agent m and time step Δt, both to be unity value [55]. This greatly simplifies the governing equations of PSO and reduces them to:

$$\overrightarrow{x_t} = \overrightarrow{x}_{t-1} + \overrightarrow{v_t} \tag{3.5}$$

$$\overrightarrow{v_t} = \overrightarrow{v}_{t-1} + \overrightarrow{F}_{t-1} \tag{3.6}$$

The only parameter which is unknown in these equations is the accelerating force, $\overrightarrow{a}$. The influences on global best and personal best on each agent are modelled as two spring like attractions [55]. This results in a force expression of:

$$\overrightarrow{F}_{t-1} = c_1(\overrightarrow{p}_{t-1} - \overrightarrow{x}_{t-1}) + c_2(\overrightarrow{g}_{t-1} - \overrightarrow{x}_{t-1}) \tag{3.7}$$

Here, $\overrightarrow{p}_{t-1}$ and $\overrightarrow{g}_{t-1}$ are position vectors of personal and global bests respectively and c_1, c_2 are Hooke's constants.

The iterative process described until now, uses social and cognitive knowledge in a deterministic manner. The pitfall of this approach is the probability of premature convergence to a local optimum, as there is no randomness in this approach. Thus, to model the natural probabilistic behavior, we need to apply some stochastic factors. The Hooke's coefficients c_1, c_2 are multiplied by random coefficients η_1 and η_2, respectively to introduce some stochastic nature to the search process [55]. These coefficients are either random scalars in the range $(0, 1)$ or arrays with random values in that same range [55]. Moreover, a time varying inertial weight is employed and varied from 0.9 to 0.4 from the beginning of the optimization toward the end. This inertial weight facilitates the quick convergence of the swarm towards the final solution. Inclusion of all these constants give the final form as in 3.8.

$$V_t = wV_{t-1} + c_1\eta_1(P_{t-1} - X_{t-1}) + c_2(G_{t-1} - X_{t-1}) \tag{3.8}$$

3.5.4 Sigmoid Limiting Transformation for Binary PSO (BPSO)

Binary optimization requires the selection of an optimum solution from a set of possible solutions. Thus the positions are defined by an N-bit binary string. (3.9) presents the position of m_{th} agent at $(i-1)_{th}$ iteration [55].

$$\overrightarrow{x}_{m,t-1} = \{x_{m1,t-1}, x_{m2,t-1}, \cdots, x_{mN,t-1}\}, \quad x_{mn,t-1} \in 0,1 \tag{3.9}$$

Binary valued positions leave only three possible distances between a position and its corresponding personal best:

$$p_{mn,t-1} - x_{mn,t-1} = \begin{cases} 1; & \text{if} \quad p_{mn,t-1} = 1, x_{mn,t-1} = 0 \\ 0; & \text{if} \quad p_{mn,t-1} = x_{mn,t-1} = 0 \quad \text{or} \quad p_{mn,t-1} = x_{mn,t-1} = 1 \\ -1. & \text{if} \quad p_{mn,t-1} = 0, x_{mn,t-1} = 1 \end{cases}$$

$$\tag{3.10}$$

The same situation appears in the calculation of $g_{mn,t-1} = 1 - x_{mn,t-1}$. Although the positions are binary values, other parameters in the velocity calculation equation, (3.8), are real values. Thus, the calculated velocity is still a real number in the range $[-V_{max}, V_{max}]$. This situation necessitates a transformation from real valued to binary valued transformation. The authors in [56] present a powerful technique to translate real valued velocity to binary valued position selection. In this technique, the velocity, $v_{mn,t}$ is related to the possibility that $x_{mn,t}$ takes a value of 1 or 0. It is implemented by defining a intermediate variable $S(v_{mn,t})$ via the sigmoid limiting transformation [55]:

$$S(v_{mn,t}) = \frac{1}{1 + e^{-v_{mn,t}}} \tag{3.11}$$

Thus, the sigmoid limiting transformation maps a variable from the range $[-V_{max}, V_{max}]$ into a function value in the range $\left[\frac{1}{1+e^{V_{max}}}, \frac{1}{1+e^{-V_{max}}}\right]$. At high velocities, there can be either $e^{V_{max}}$ or $e^{-V_{max}}$ term in the denominator, which have very high and near to zero values respectively. As this value is in the denominator, the range reduces to (0,1). To introduce

a random nature necessary for any stochastic process, a random number $r_{mn,t}$ is generated and is compared with the result of the sigmoid limiting transformation $S(v_{mn,t})$. The n-th bit selection criteria is:

$$
x_{mn,t} = \begin{cases} 1; & r_{mn,t} < S(v_{mn,t}) \\ 0; & r_{mn,t} \geq S(v_{mn,t}) \end{cases} \tag{3.12}
$$

3.6   A Design Example using Particle Swarm Optimization

A pilot system for a wheelchair application is designed to illustrate a possible application of the proposed method. Table 3.5 lists the specifications of the system. The outer diameters of the primary and secondary coils are dictated by the space under the wheelchair. AWG 12 Litz wire is chosen, based on the current density, and the strand AWG of 38 is chosen, which is suitable for operation in a large frequency range of 20-150 kHz. There are five design variables to be optimized: frequency, the number of turns per layer in primary and secondary, and the number of layers in primary and secondary. The frequency sweep also ranges from 20 to 150 kHz with a resolution of 1 kHz. The maximum number of turns per layer is 35, restricted by the space and the thickness of the wire. The number of layers is restricted to 3. That gives a total search space of 1,433,250 elements and clearly, testing each of them would result in very high computational burden.

Table 3.5: System specifications for the robot WIPT system ©[2015] IEEE.

Parameter	Value
Length from front wheel to end of the board	14 Inch
Length from wheel to wheel	14 Inch
Height from bottom of the wheel chair to top of the floor	3.0 Inch
The thickness of floor	1 Inch
Rated transfer of power	200 W

Coils can be compensated in two ways: series and parallel, resulting in four different compensation topologies: Series-Series (SS), Series-Parallel (SP), Parallel-Series (PS), and Parallel-Parallel (PP). All four compensation techniques are investigated below.

A PSO based simulation tool is developed in MATLAB to implement all analytical functions and calculate the most efficient solution. In the PSO algorithm, the number of particles is 10 and the maximum number of iterations is 100. This results in a total of 1,000 computations. Fig. 3.6 shows its convergence even before a maximum number of iterations is reached. This implies that the PSO can reach the same solution as a brute-force search algorithm, but at only 0.07 % computational cost. The algorithm was run for all four different compensation topologies. The results are summarized in Table 3.6, where N_{tl} is the number of turns per layer, N_l stands for the number of layers, and VA is the VA rating. Subscripts p and s stands for primary and secondary coils, respectively.

Results obtained through a fast PSO can help in gaining some interesting design intuitions. For example, the most efficient power transfer is never at very high frequency, due to higher ac resistance of the coils. While the asymmetry in coil designs is expected due to different voltages at primary and secondary (150V vs. 24V), the optimization reveals that parallel compensation at secondary favors the designs with very small number of turns. For parallel compensated secondary and constant transferred power, the inductance of the secondary should be inversely proportional to the load current. In that case, the most efficient solution is achieved for a small primary coil current (but for large number of primary coil turns), and a small secondary inductance that produce a significant receiver current. This analysis also confirms a well-known fact that SS and PS compensation, due to absence of secondary reactive current component, result in the most efficient design of magnetic couplers.

Pareto optimality is considered for multi-objective optimization when it is impossible to make one performance index better without making at least one of the others worse. In a WPT link, the two most important performance indexes are efficiency and coils VA rating. Ideally, designers want an efficient system with low VA rating. Our investigations proved that independent optimization of primary or secondary VA ratings always leads to oversized coils at the opposite side Fig. 3.7. Thus the decision was made to optimize the total VA rating of the system. Fig. 3.8, shows the Pareto front for all four different compensation

techniques for a total VA vs. efficiency multi-objective optimization.

Table 3.6: Single objective optimization results ©[2015] IEEE

Comp.	f (kHz)	$N_{tl,p}$	$N_{l,p}$	$N_{tl,s}$	$N_{l,s}$	$\eta(\%)$	VA_p	VA_s
SS	67	20	2	4	2	97.67	1014.5	874.3
SP	56	22	2	3	1	95.79	1814.8	332.2
PS	53	21	3	9	1	97.87	949	719.7
PP	58	22	2	3	1	95.82	1839.9	320.5

A prototype of a WPT system is built to verify the PSO algorithm. Primary and secondary coils have 31 and 3 turns, respectively, arranged in one layer (Fig. 3.9). System operates at 40 kHz and employs a 12/38 AWG Litz wire for coil manufacturing. The prototype is used to verify the accuracy of the modelling process, as well as for comparison between the modelled and the measured power transfer efficiency. The calculated and measured circuit parameters are given in Table 3.8.

Table 3.7: Design parameters for the WIPT system of a wheel chair ©[2015] IEEE

Design Parameter	Value
Operating frequency	40 kHz
Primary coil AWG	12
Number of strands in the primary wire	660
Number of turns per layer at primary	31
Number of layers in primary	1
Secondary coil AWG	12
Number of strands in the secondary wire	660
Number of turns per layer at secondary	3
Number of layers in secondary	1

Table 3.8: Experimental results of the PSO algorithm ©[2015] IEEE

Parameter	Simulation result	Experimental result
Primary coil inductance	284.23 μH	283.67 μH
Primary coil resistance	0.1763 Ω	0.2109 Ω
Secondary coil inductance	8.37 μH	8.714 μH
Secondary coil resistance	0.02 Ω	0.0265 Ω
Mutual inductance	9.32 μH	9.13 μH
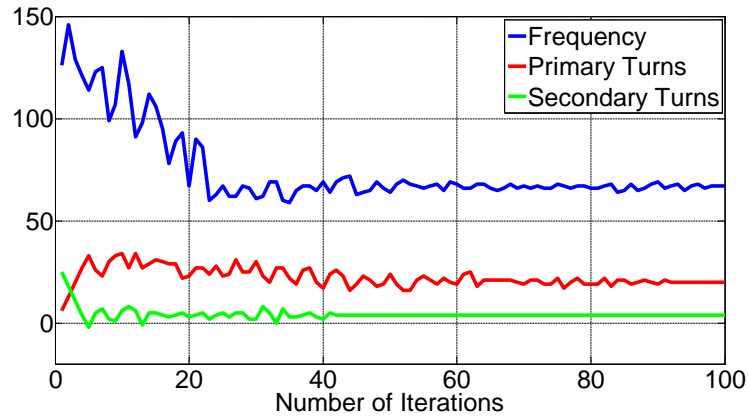
Fig. 3.6: Convergence of PSO variables for single objective optimization ©[2015] IEEE.
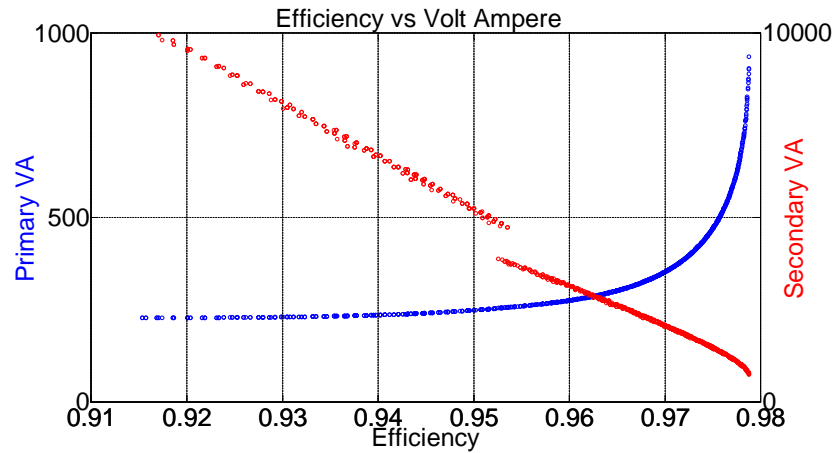
Fig. 3.7: Primary and secondary VA ratings vs. efficiency in the case of single objective (primary VA rating) optimization ©[2015] IEEE.
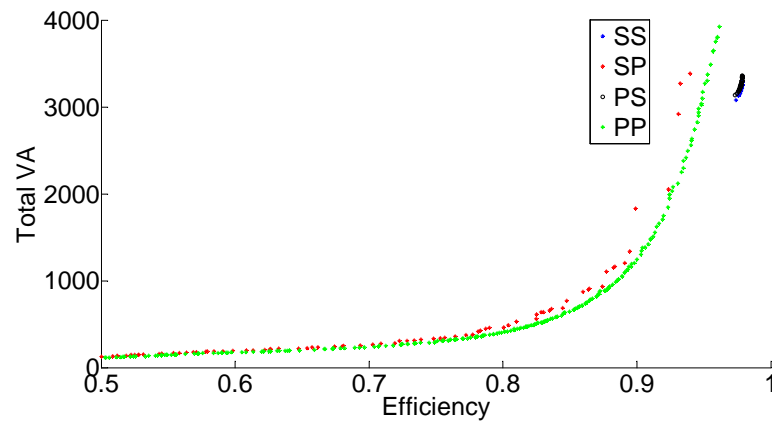
Fig. 3.8: Efficiency vs. total VA rating for four compensation topologies ©[2015] IEEE.
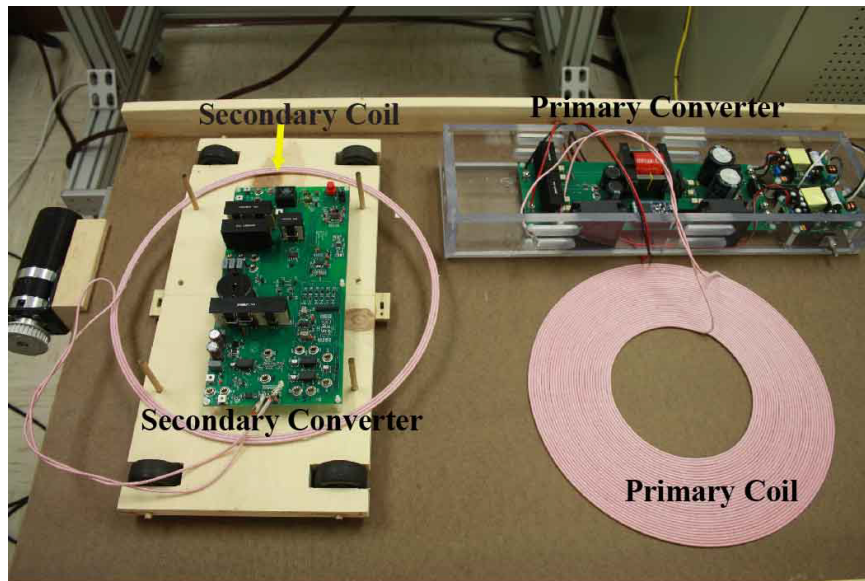
Fig. 3.9: Setup for PSO design verification ©[2015] IEEE.

Chapter 4

Characterization of the Power Transfer Control Problem in Lumped Transmitter Coil-Based In-Motion Wireless Power Transfer Systems

The goal of an in-motion wireless power transfer system is to transfer a certain amount of energy to a moving vehicle with highest possible energy and power efficiency. Previously designed systems in this area generated constant field over the track and the controller in the vehicle was responsible for the power flow control. This approach, although considerably simpler, suffers from much lower energy and power efficiency. In this thesis, a new approach of power transfer is explored. In the proposed approach, the track field is controlled to control the power transfer. As the primary is turned on for a short period of time, this technique has the potential of significantly improved power and energy efficiency.

This chapter analyzes suitable wireless power transfer system architecture for dynamic charging application and identifies the ideal control variable for power transfer control. Section 4.1 presents different wireless power transfer systems for a wide range of applications. A critical review of transmitting coil structures identifies lumped transmitting coil as the more promising structure in terms of higher efficiency and lower VA rating. Although lumped coils have better power transfer characteristics, they create a requirement for accurate vehicle position detection and vehicle communication. Section 4.3 is devoted to analysis of the state-of-the-art position detection and vehicle communication technologies. The key takeaway of this section is that, position detection technologies of the required precision are both complicated and costly. This situation imposes the need for a position sensorless control algorithm. The dynamic parameter in a dynamic wireless power transfer system is the mutual inductance between coils. Section 4.4 is devoted to the extraction of mutual inductance profile. The last two sections analyze the choice of appropriate compensation

structure and identification of ideal control variable for dynamic WIPT systems.

4.1 In-Motion Wireless Power Transfer Systems

Wireless inductive power transfer (WIPT) is the only viable method to transfer energy to a free-moving vehicle. As long as the receiving coil is exposed to high-frequency magnetic field created by the transmitter, the velocity of the receiving object has negligible impact on power transfer. This attractive feature has made WIPT the prime contender to solve the problem of limited on-board energy. Continuous or intermittent charging of on-board batteries can improve vehicle autonomy, prolong the battery life and reduce on-board energy storage requirements.

In-motion wireless charging applications can be broadly classified into three categories, depending on the degrees of freedom the moving object demonstrates with respect to the source field. These are application with only horizontal movement, both horizontal and lateral movement and omnidirectional movement. Some moving objects (eg. factory conveyers and assembly lines, monorails, electric trains, etc. [37, 57–59]) follow predetermined paths having only one degree of freedom. That allows researchers to explore different structures of transmitting and receiving coils, as well as different shapes of magnetic circuit, and achieve both contactless power transfer and high local coupling between coils. For example, the authors in [58] propose a removable, closed-shape dual ring design of magnetic circuit for linear WPT systems with almost no gap. Consequently, coupling between transmitting and receiving coils is improved and less energy is stored in the leakage field, resulting in higher efficiency and power transfer capability of the system. The most frequently used pickup core structures (U- and E-shaped cores) in existing linear WPT systems are discussed in [59], while in [37] the authors present easy removable gapped coaxial WPT system for MAGLEV railway applications.

On the other side, wireless charging systems for heart pumps, biological implants, various transcutaneous changing systems for health monitoring, etc., necessitate movement in three directions, and consequently require a WPT system that can deliver power for any arbitrary position of the receiver. Since these systems usually operate at very high

frequency, typically in MHz range, and have specific, multi-coil receiver topology, they will not be investigated any further in this thesis.

Automated Guided Vehicles (AGV), mobile robots, and electric vehicles move in two directions, sometimes following predetermined paths. Unlike unidirectional guided objects discussed above, lateral misalignment is likely to happen in this case, which eventually reduces the local coupling and power delivered to the receiver. To dynamically charge those objects (to charge them while they are moving), the source of the primary field coil is typically buried under the ground while the receiving coil is attached underneath the vehicle at a constant vertical distance from the ground and source of the field. The coil structures are planar. The shape can be both circular or rectangular. In this thesis, circular coils are explored due to the uniform change of mutual inductance with misalignment. ©2015 IEEE

4.2 Review of Transmitting Coil Structures in In-Motion Wireless Power Transfer Systems

While the vehicle size imposes restrictions upon receiver coil dimensions, two distinctive designs both illustrated in Fig. 4.1, have been adopted for the transmitter coil: distributed elongated track and series of independent lumped coils. Distributed elongated tracks of various lengths and structures have been employed in the designs presented in [16–23]. While energized, the track provides continuous and nearly constant power to a vehicle moving over and along this track. However, a large portion of the primary track remains unutilized since the receiver coil is coupled with only a part of the primary track, not the total primary. As a long track has very large wire, it naturally results in a large inductance (typically 1-2 μH/m [19]) and parasitic resistance. The high inductance and resistance limits the maximum track current to a lower value for the specified track VA rating, and higher losses in the primary coil. Problem of the limited primary track VA rating can be solved by partitioning the track into segments that are independently compensated, but parasitic resistance of the track cannot be eliminated. As a result, the systems presented in [18–23] are typically limited in efficiency, ranging from 70% to 80%, although the equivalent stationary WIPT systems of similar power per pad are reported to achieve the efficiency

of over 90% [41]. Recently, the efficiency of 80% has been reported for a 2m-long cross-segmented electric "I"-core-type rail for roadway powered electric vehicles [20]. [60] ©2015 IEEE.

After identifying the limitations of the elongated primary track, researches have investigated a design where a series of lumped coils are employed to act as transmitters delivering power to a vehicle moving over the coils [20], as illustrated in Fig. 4.1 b). One coil at a time is involved in power transfer, and the entire inductance of the primary coil contributes to it by increasing the mutual coupling between the coils. Energized in a timely manner, these coils can deliver power more efficiently than the elongated track, at the same time reducing the coil voltage stress and eliminating the need for distributed series compensation. However, efficiency improvement is only observed when the two coils are aligned. When coils are misaligned, both transferred power and efficiency are greatly reduced. A possible efficiency profile measured for constant transmitter (input) power is presented in Fig. 4.2 as an illustration. The power that a vehicle moving at a constant speed would receive for different misalignments is illustrated in Fig. 4.3. This phenomenon is also reported in [23] where researchers measured picks and dips of efficiency and the power transferred while the vehicle was moving over two adjacent primary coils. For some positions of the vehicle and the receiver coil, power transfer as low as 10% of the peak value is reported in [23].

From the discussion above, two conclusions can be drawn: a) lumped coils acting as transmitter coils can provide higher power transfer efficiency, only if they are inactive most of the time and energized only when the vehicle with the receiver is above the particular transmitter coil; In Fig. 4.2 which serves as an illustration, it is assumed that power transfer would be terminated when efficiency reduces below 70%; b) synchronization of charging activation and termination with respect to the vehicle position is crucial for effective charging since the receiving coil resides over the transmitter coil for a very short interval of time. For example, a 0.5 m receiving coil of a vehicle moving at the speed of 18 km/h would be exposed to identical transmitting coil for less than 150 ms. Moreover, the time of strong alignment would be just a fraction of that interval, as it is illustrated in Fig. 4.3. This time
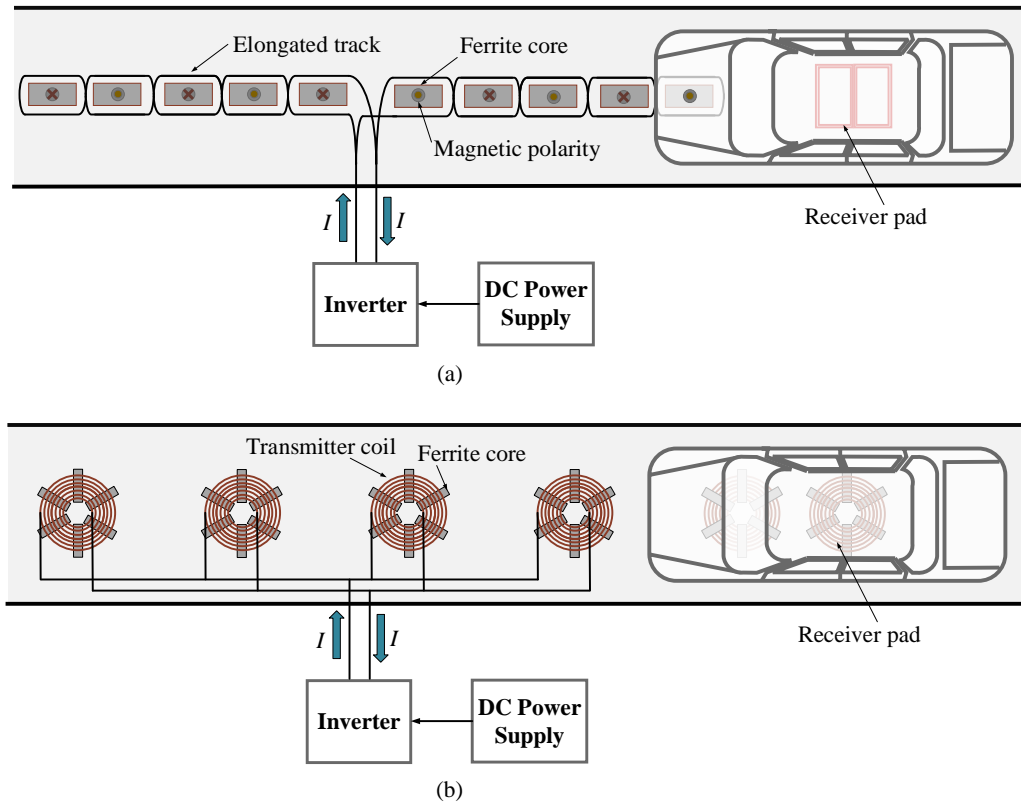
Fig. 4.1: Illustration of a) distributed elongated track b) series of independent lumped coils, as a transmitter coil in an in-motion WPT system.
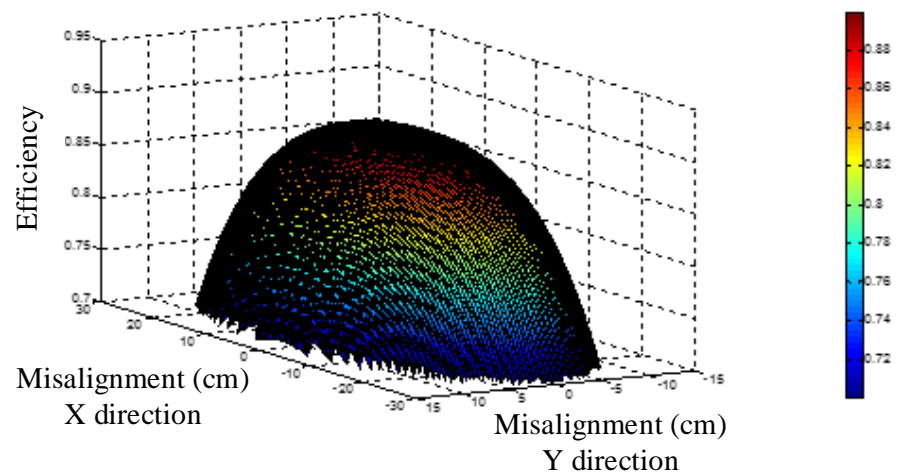
Fig. 4.2: 3D Contour plots of WPT efficiency for different alignments of polarized transmitter and receiver coils - an illustration. X - traveling direction, Y - lateral direction.

becomes even shorter if the vehicle is laterally misaligned with respect to the transmitter coil position.

4.3 State of the Art of Vehicle Position Detection and Vehicle Communication Systems Available for In Motion Charging

There are two challenges typically overlooked when researching dynamic charging of EVs: accurate vehicle position detection and reporting of that position to the charger in a timely manner (if the detector is not directly wired to the transmitter control logic). Some means of position detection and wireless communication (for example Global Positioning System (GPS) [42] and Dedicated Short Range Communication (DSRC) [43], IEEE 802.11p) can be considered to help in providing timed energizing of the transmitter coil. In that case, vehicle should continuously update its position and inform the charger about it. The charger would use the information to determine the most suitable voltage and timing needed to energize the coil and deliver power. Although seemingly simple, this approach introduces some implementation issues, increases the cost and reduces the reliability of the system. In the text that follows, some position detection and wireless communication techniques will be discussed.

Global Positioning System (GPS) is widely used for civilian positioning applications, most commonly as a driving guide. But, GPS lacks the accuracy needed for this particular application. According to [42], GPS provides the best accuracy of around 7-8 meters, and the accuracy drops if the object dynamically changes position. Although there are augmentation techniques that can enhance the accuracy of GPS, it is still far from the required precision for WPT applications. The best case accuracy of Differential GPS system approaches the requirements of WPT dynamic charging applications [61], but the complexity and cost associated with implementation of those ground-based reference stations would be substantial.

Traditional vehicle detection technologies include intrusive techniques, in which devices are inserted into roadbeds (inductive loops and magnetometers) and those mounted overhead or at the road side (cameras - video image detection, radars or sound detector
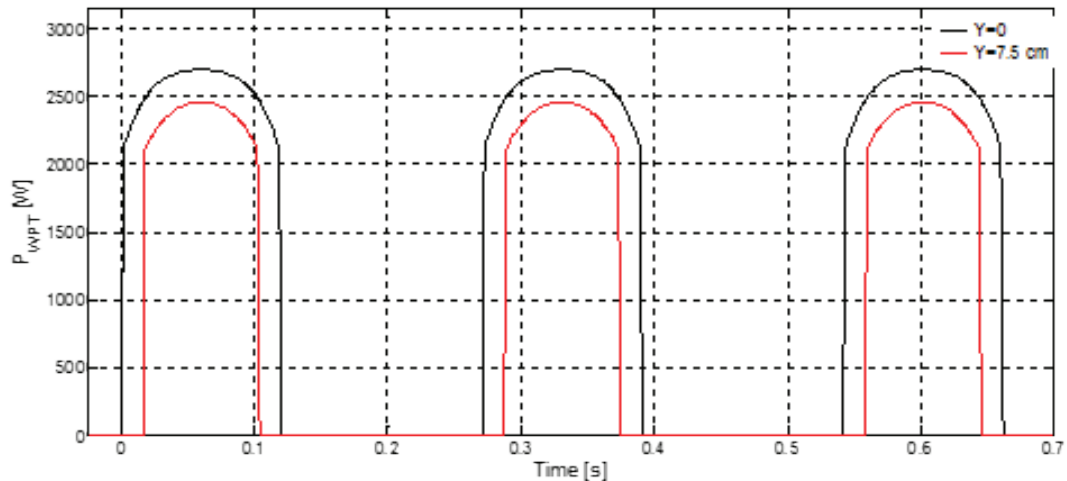
Fig. 4.3: Profiles of wireless power delivered to a vehicle receiver at the speed of 36 km/h for centered and laterally misaligned vehicle paths. Size of the pads: 50 cm x 50 cm.

systems) [62]. All those are dominantly used to detect the presence, and sometimes the passing or speed of the vehicle. Considering the density of the transmitting charging pads and accuracy that are required in both longitudinal and lateral directions, overhead systems would require a dense construction network to cover the entire road section, or otherwise it may experience problems with its viewing angle and pavement reflection (for video systems). On the other hand, road embedded systems, e.g. inductive loops commonly used for vehicle presence and position detection, offer very good accuracy. However, maintenance would be difficult compare to other systems. Since most of those systems operate on magnetic principles, they may interfere with the wireless power transfer, and eventually detune the resonant system. On top of everything, accurate detection of the vehicle itself may not be enough since the position or layout of the coils underneath the chassis may vary from one manufacturer to another.

Regarding the wireless communication protocols and devices, situation is more certain. Oak Ridge National Lab (ORNL) have reported successful low latency communication between grid and vehicle charging subsystems by using 2.4 GHz radio modem systems and delivering 6-byte message with the round trip time of approximately 20 ms [26]. Since 2.4 GHz range is already adopted by growing Wi-Fi network for hand-held and hand-free

devices, it is expected that vehicle-to-charging-infrastructure communication would be incorporated into 5.9 GHz DSRC frequency band. With the data rate of up to 27 Mbps, range up to 300 m, and allowed vehicle speed up to 120 km/h [43], DSRC has already proved a promising communication protocol for vehicle-to-roadside and vehicle-to-vehicle systems, and inclusion of vehicle-to-charging infrastructure communication would be an anticipated extension.

Vehicle position detection and vehicle-to-charger communication is a subject of extensive research and progress in this area can be expected in the future. However, all the solutions that have been proposed and will be proposed in the future would obviously a) proportionally raise the cost; b) increase complexity, and c) reduce reliability of the system. This situation creates the demand for a reliable, non-expensive strategy for vehicle position detection and optimum control of charging with limited communication requirements. According to the author's best knowledge, this topic has not been covered in the literature so far. Thus this research addresses a novel problem of sensorless wireless power transfer control to alleviate the need for any type of vehicle position sensing.

4.4 Analysis of the Mutual Inductance Profile for In Motion WIPT Systems

The principal difference between a dynamic charging system and a stationary one is the time variation of mutual inductance. A 3D electromagnetic simulation tool, ANSYS MAXWELL software is used to generate mutual inductance profile for the proposed coils. Equation (4.1) shows that transferred resistance is proportional to the square of mutual inductance. Thus, knowledge of mutual inductance variation is sufficient to model the load variation. A 3D Finite Element Modeling (FEM) tool, ANSYS MAXWELL is used to get the mutual inductance variation curve with respect to different misalignments. The designed coil is used for these simulations. The mutual inductance curve is shown in Fig. 4.4. A closer inspection of the mutual inductance curve reveals negative inductance at larger misalignments. This phenomenon is reported in [63]. This unusual behavior can be explained using the field cancelation theory, when the two coils are far away, partly overlapped. In this misaligned state, the magnetic flux generated by the two coils are added

destructively. This results in overall reduction of the total magnetic flux, and thus negative inductance. The proposed algorithm only senses the power from the dc bus, which is always positive, irrespective of the mutual inductance polarity. Negative inductance will result in positive power, as resistance is proportional to the square of mutual inductance. A thorough analysis of the mutual inductance curve reveals that the maximum negative inductance is around 5% of maximum inductance. As transferred resistance is square proportional to mutual inductance, the negative peak will transfer only 0.25% of the maximum power. Thus, mutual inductance below 5% of the maximum value is ignored.

$$R_{ref} = \frac{\omega^2 M^2}{R_s} \tag{4.1}$$

Here, ω is the angular frequency of operation, M is the mutual inductance and R_s denotes the secondary load resistance.

4.5 Compensation Structure Choice for In Motion WIPT Systems

The choice of primary compensation structure is an important question for in-motion
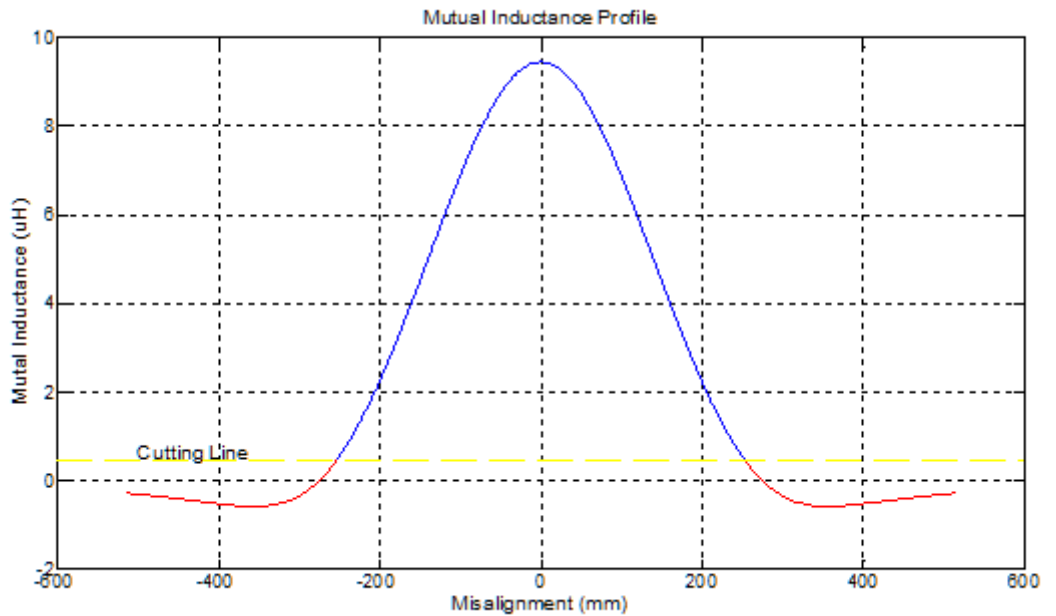
Fig. 4.4: Mutual inductance profile ©[2015] IEEE.

wireless power transfer systems based on lumped transmitting coils. Traditional series and parallel compensation serve well for both in motion charging applications based on elongated tracks and stationary charging applications. However, due to the intermittent nature of power transfer presented by lumped in-motion power transfer systems, series and parallel compensations show serious shortcomings. The problem stems from the fact that in motion power transfer requires strong control over the track current, essentially requiring track current to be independent of load characteristics. Traditional series and parallel compensation both have strongly load dependent track currents. On the other hand, the LCL compensation technique offers excellent control over the load current while tuned, making it suitable for this particular application.

A typical wireless power transfer coil is considered for the understanding of different compensation technique behaviors. The system specifications are given in Table 4.1. The same coils are considered for different possible compensation techniques and performances are evaluated to find the best compensation technique.

Table 4.1: Parameters for compensation choice simulations

Parameter	Unit	Value
Rated primary current	A	10
Rated primary voltage	V	40
Parasitic resistance in the coil	Ω	0.125
Parasitic resistance in the capacitor	Ω	0.125
Rated power	W	400

In the case of series compensation, power transferred is maximum only when load resistance equals parasitic resistance. The loss is maximum when there is no vehicle and the amount of loss far outweighs the power transferred. Not only that, the amount of power loss is far higher than the system rated power, which makes the system unsustainable. It reflects the conclusions of the maximum power transfer theorem: the power transferred is maximized when the load resistance equals the parasitic resistances. The efficiency curve is bell-shaped with the maximum at the middle. A closer look at the transferred power and efficiency expressions give us insight into the reason behind this curves.

$$P_{txf} = \left(\frac{V_{in}}{r_{txf} + r_{par}} \right)^2 r_{txf} \tag{4.2}$$

$$P_{loss} = \left(\frac{V_{in}}{r_{txf} + r_{par}} \right)^2 r_{par} \tag{4.3}$$

$$\eta_P = \frac{P_{txf}}{P_{txf} + P_{loss}} = \frac{r_{txf}}{r_{txf} + r_{par}} \tag{4.4}$$

These equations show that, when the resistance reflected is zero, meaning the vehicle is out of site, the transferred power is also zero. The efficiency is highest when the reflected resistance is highest. Fig. 4.6 and Fig. 4.5 show power transfer characteristics of series compensation. The key point to notice is the untenable amount of losses generated when the vehicle is misaligned.

Parallel compensation also shows similar characteristics. Contrary to the voltage fed series compensation, a parallel compensating tank has to be supplied by a current source. The power transferred to the load has a very similar curve to the series compensated primary.

Fig. 4.5: Reflected resistance normalized to maximum and efficiency for series compensation ©[2015] IEEE.
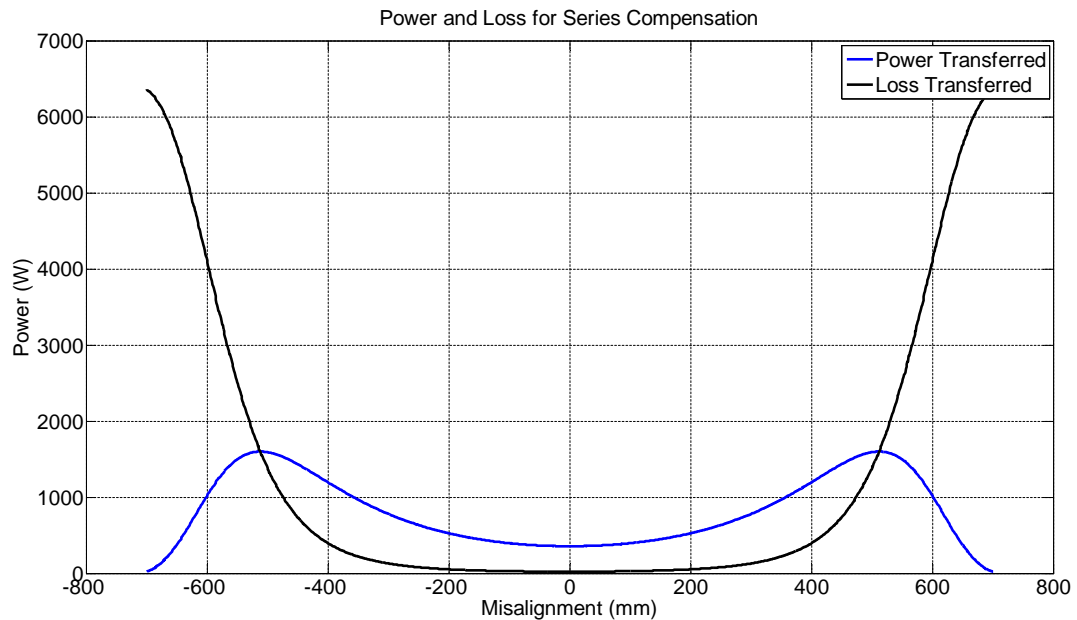
Fig. 4.6: Transferred power and loss for a series compensation©[2015] IEEE.

Fig. 4.7 shows power transferred and losses for a parallel compensated primary. The transferred power is maximum when the transmitted resistance is equal to the parasitic resistance. The efficiency curve in Fig. 4.8 again has the typical bell shape.

These simulations give an insight to the inherent nature of these systems. In these systems, the efficiency increases when the reflected resistance is maximum. But, the transferred power does not follow the efficiency, as the current through the track is changing with the load. If it is possible to have a constant current through the track, irresponsive to the change of resistance through the track then the power curve will also follow the efficiency curve.

This ideal situation is created by the LCL resonant network proposed by Pantic et al. in [64]. This special resonant tank configuration creates a constant current through the track and thus the power transfer is proportional to the reflected resistance. The Fig. 4.9 shows the desired bell-shaped power transfer curve and constant parasitic loss. The efficiency curve in Fig. 4.10 is also slightly wider. This discussion leads us to the conclusion that LCL is an ideal compensation technique for in-motion wireless power transfer.
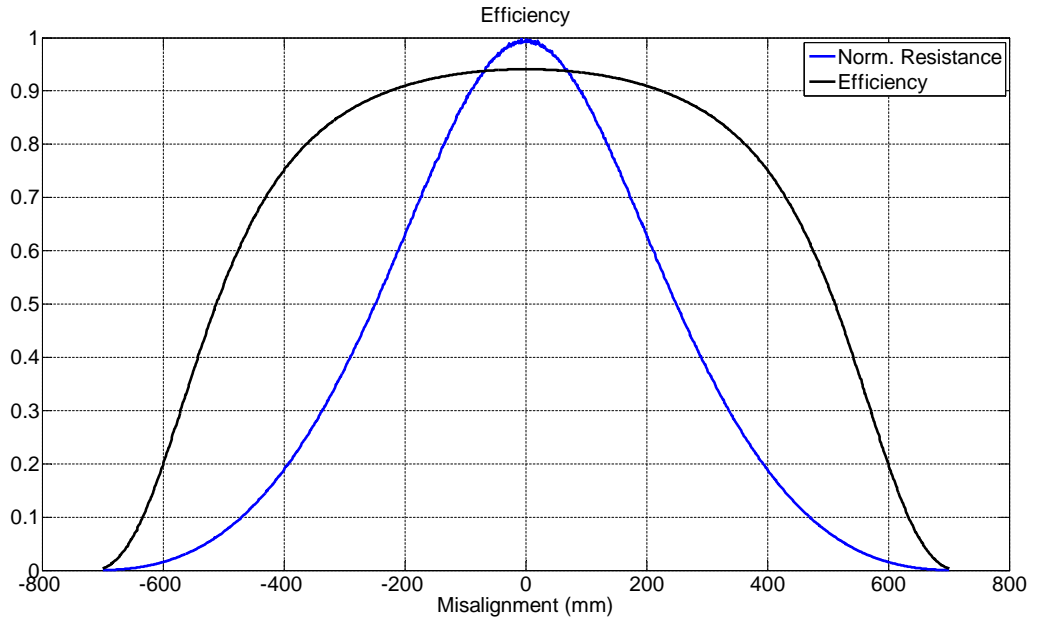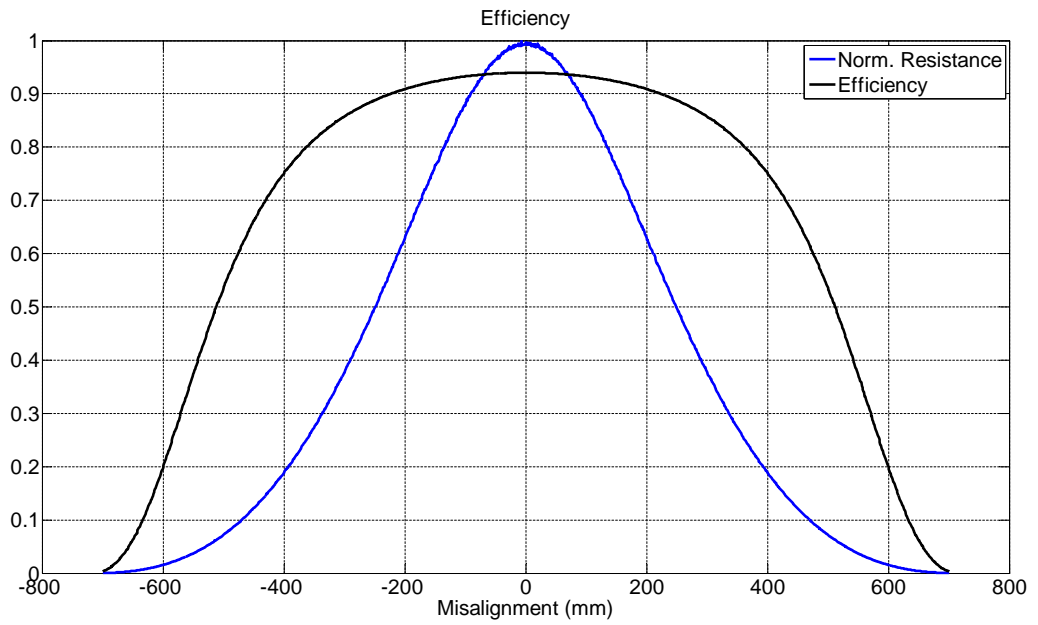
Fig. 4.7: Reflected resistance normalized to maximum and efficiency for parallel compensation©[2015] IEEE.
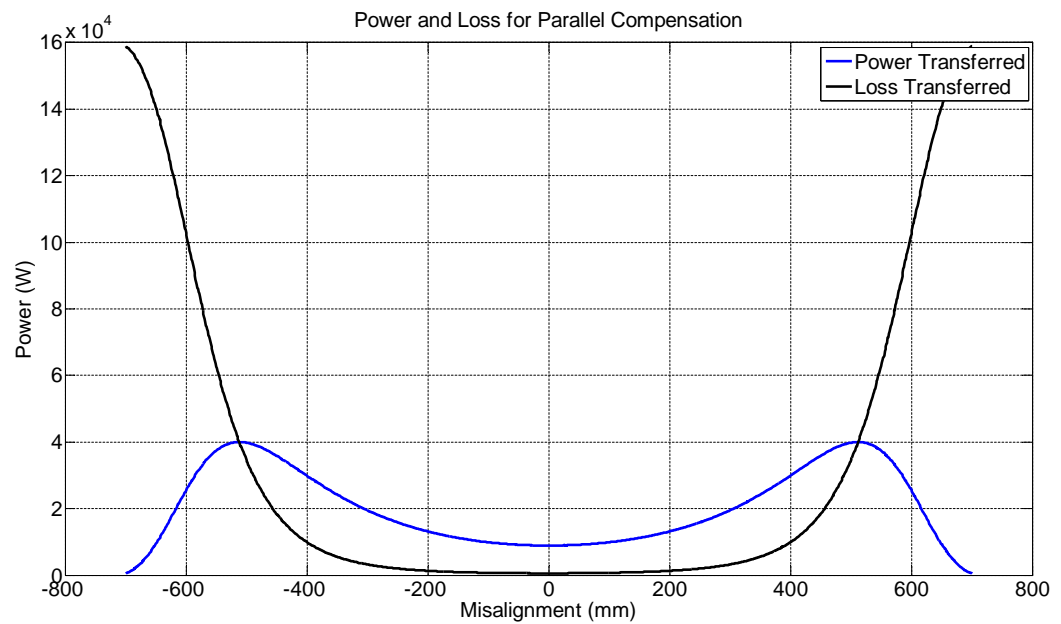
Fig. 4.8: Transferred power and loss for parallel compensation©[2015] IEEE.
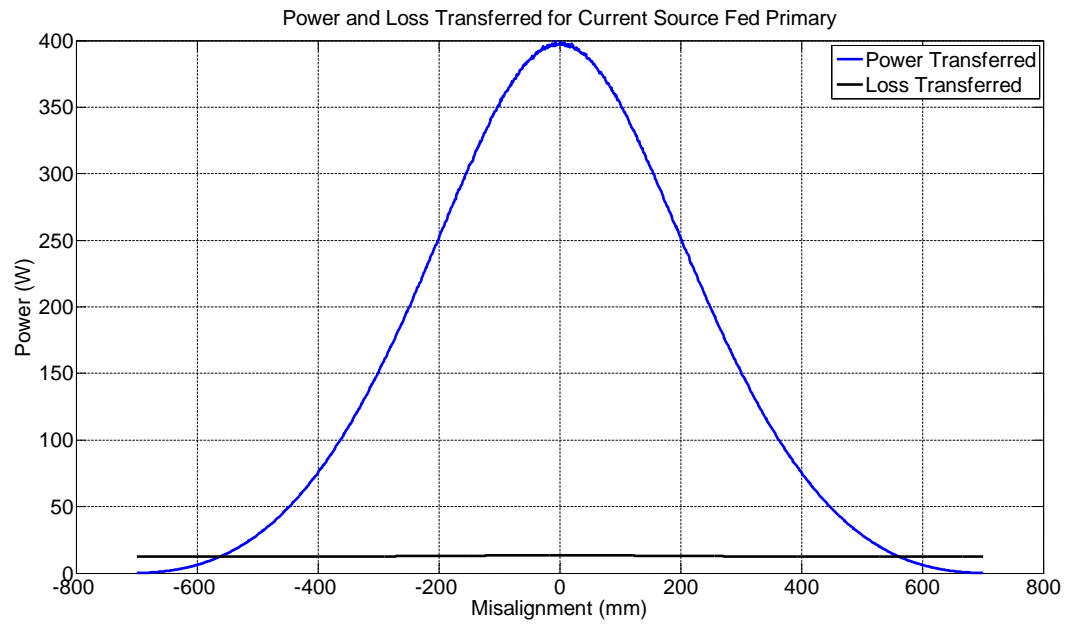
Fig. 4.9: Transferred power and loss for LCL compensation©[2015] IEEE.
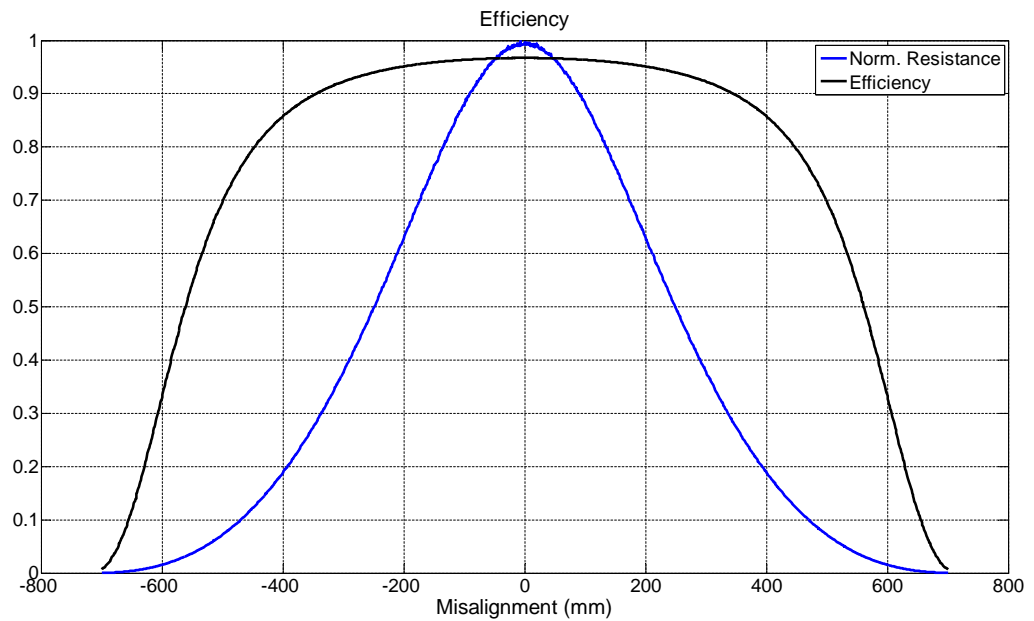
Fig. 4.10: Reflected resistance normalized to maximum and efficiency for LCL compensation©[2015] IEEE.

4.6 Analysis of Dynamic WIPT System Structure and Identification of Ideal Control Variable

The WIPT topology considered in this study is presented in Fig. 4.11. This WIPT system includes two resonant compensation circuits (compensation tanks), placed at the primary and secondary. Primary compensation circuit is responsible for both boosting and filtering transmitter coil current, enabling an inverter of a relatively low VA rating to drive a highly inductive coil inductance. The secondary compensation coil enhances power transfer by boosting the voltage and/or current at the receiver side. As illustrated in Fig. 4.11, the transmitter consists of a rectifier followed by a front-end buck converter that adjusts the dc voltage level applied to the input of a single-phase inverter. The DC converter at the input can be omitted, particularly if phase shift modulation is employed to control the inverter output voltage V_{inv}. A similar configuration is employed at the receiver side to condition the AC power provided by the receiver coil to a form suitable for mainly DC loads at the output.

From the structure above, one can see that power flow from grid to DC load can be controlled both at the receiver and the transmitter sides. Operation of majority of the receiver side controllers is based on modulation of receiver circuit's loaded quality factor Q_L. Quality factor modulation is accomplished through electronically varying the resonant conditions at the receiver, which is equivalent to "screening" the load in a controlled manner from the primary. Although this control is typically enough to satisfy all load requirements, it forces the source to operate at full voltage, being ready to respond to full load requirements of the receiver at any time. This might be inefficient, especially in dynamic charging where full load is delivered for a very short period of time. Recognizing this problem, the authors in [41] propose dual side control in order to maximize overall system efficiency by simultaneously adjusting duty ratio of the boost converter at the receiver and inverter phase shift angle at the transmitter side. However, operation of the proposed controller is contingent upon proper estimation of the coils' mutual inductance and precise system efficiency modeling, and its accuracy might be questionable for a dynamic environment as
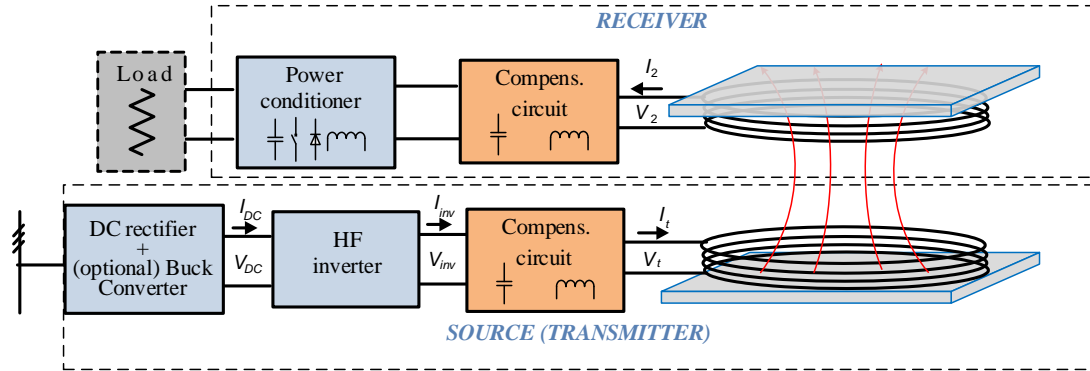
Fig. 4.11: Block diagram depicting a typical inductive WIPT system.

the one discussed here. Also, the central controller positioned at one or the other side of the system would need to exchange real-time measured and control signals with the other side, creating a substantial burden to communication devices. Therefore, in this study, the focus is on the primary controller design with the objective to maximize energy efficiency for dynamic charging applications.

Both the buck converter and the inverter can regulate power transferred to the receiver by varying the frequency or the magnitude of the inverter output voltage. In this thesis, constant frequency operation is considered since the variable frequency control requires complex receiver design, and for a wider range of regulated power it may result in inefficient operation. Fig. 4.12 shows a detailed model of a MOSFET-based transmitter structure, including detailed topologies of both buck and the inverter, and its scaled-down version is used later for experimental verification. In Fig. 4.12 model of the transmitter resonant circuit is presented. The LCC compensation topology is selected, and it consists of series inductor L_s, parallel capacitor C_p and series capacitor C_s. Transmitter coil is modeled with inductance L_t, while the effect of the secondary is represented with reflected impedance Z_r. The resistive part of reflected impedance models active power transfer, while X_r quantifies the uncompensated part of the receiver reactance and/or the presence of magnetic field suppressors surrounding the pads' system (metal pad shielding, vehicle chassis, etc.). To simplify the discussion below, the losses of those components are neglected in Fig. 4.12

and Fig. 4.13, but they will be reassessed later when the system efficiency is studied. If the quality factor of the resonant circuit is high enough (typically above 3), the resonant circuit will filter out most of the higher current harmonic content, allowing only the fundamental component to reach the transmitter coil. Accordingly, for the purpose of power transfer analysis, it is enough to consider and control the first harmonic of the voltage at the output of the inverter, which is emphasized in Fig. 4.13. Certainly, higher harmonics, dominantly flowing through L_s and C_p resonant elements, generate loss in both the inverter and the resonant circuit and should be considered for an accurate loss analysis [21]. LCC compensation structure is adopted at the primary because of its appealing characteristics, when properly tuned: i) voltage regulated, load- and coupling-independent transmitter coil current I_t; ii) voltage stress better distributed among the reactive elements and transmitter coil than in traditional LCL or series compensation topologies; iii) ability to adjust the phase angle between the inverter voltage and the current, or even make it zero, if desired.

Design of an LCC resonant tank is discussed, for example, in [64]. While L_s, and C_p are mostly used to create the resonance with the coil inductance at the operation frequency $f_s = \frac{\omega_s}{2\pi}$:

$$\omega_s L_s = \frac{1}{\omega_s C_p} = \omega_s L_t - \frac{1}{\omega_s C_s} \tag{4.5}$$
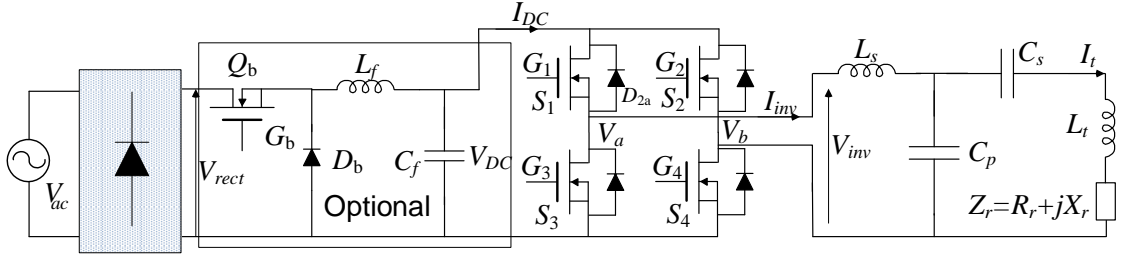
Fig. 4.12: Detailed transmitter topology with the reflected impedance Z_r modeling the receiver presence ©[2015] IEEE.
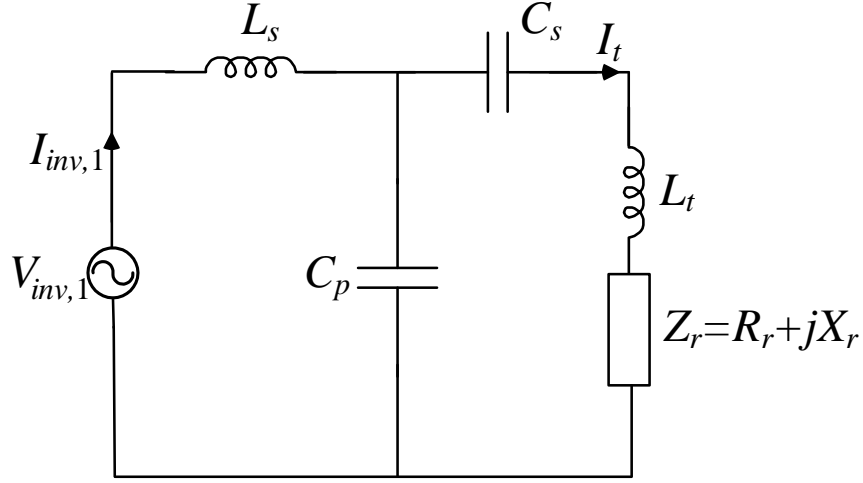
Fig. 4.13: Transmitter compensation circuit topology with reflected impedance Z_r and fundamental supply voltage $V_{inv,1}$.

C_s allows adjusting of transmitter coil current independently from the coil parameters and the inverter voltage rating:

$$I_t = \frac{V_{inv,1}}{\omega_s L_t - \frac{1}{\omega_s C_s}} = \frac{V_{inv,1}}{\omega_s L_s} \tag{4.6}$$

Another options are adjusting the phase angle between the first harmonic of the voltage and current $V_{inv,1}$ and $I_{inv,1}$ to lower the inverter switching loss [21], whichever is more important for a particular design. For the adopted design of the compensation circuit, reflected reactance X_r has no impact on the track current or the power flow, and only varies the phase angle between the inverter voltage and the current affecting to some extent the loss of transmitter system. In the analysis that follows its effect will be neglected.

As a conclusion, for a tuned resonant circuit, the transmitter coil current I_t and the transferred power P_t can be directly controlled by controlling the magnitude of the inverter output voltage on the first harmonic $V_{inv,1}$:

$$I_t = \frac{V_{inv,1}}{\omega_s L_s} \tag{4.7}$$

$$P_t = I_t^2 R_r = \left(\frac{V_{inv,1}}{\omega_s L_s}\right)^2 R_r \tag{4.8}$$

Both inverter and buck converter can control voltage $V_{inv,1}$:

$$V_{inv,1} = \frac{2\sqrt{2}V_{DC}}{\pi} \cos\frac{\alpha}{2} \tag{4.9}$$

Buck converter controls $V_{inv,1}$ by varying duty cycle D and controlling the DC voltage V_{DC} at the inverter input. However, that control would require buck hard-switched converter to be incorporated, and many researchers decide not to do so, supplying the inverter directly from the output of the rectifier. On the other hand, various techniques of fixed-frequency phase shift modulation are available to vary control angle and provide control over the inverter output voltage. In [65] traditional single parameter symmetric phase shift modulation (also known as Symmetric Voltage Cancelation (SVC) strategy) is investigated and applied in LCL converters in WPT systems, and optimized with respect to loss, total harmonic distortion, and overall converter cost. In [66], the authors compare SVC with Asymmetric Duty Cycle (ADC) and Asymmetric Voltage Cancelation (AVC) strategies for operation in ZVS DC/DC series resonant converters, discovering that for some conditions AVC control results in slightly lower total converter loss. Similar results, but now for LCL WPT converters are reported in [67], where AVC provided better efficiency due to the elimination of diode reverse recovery loss. However, ADC requires three control variables, as opposed to one variable for SVC technique, whose optimum selection is not always a straightforward process [67].

The selection of the transmitter topology and inverter output voltage control strategy do not alter the operation of the proposed algorithm, as it only depends on the inverter output voltage magnitude. Therefore, for this study we adopt SVC control strategy that

involves only the inverter, and ignores the buck converter. The SVC is selected due to simplicity, and the reference value of the phase shift angle α can be directly determined from (4.10) as:

$$\alpha = 2\cos^{-1}\left(\frac{\pi V_{inv,1}}{2\sqrt{2}V_{DC}}\right) \tag{4.10}$$

Typical SVC waveforms are given in Fig. 4.14 due to the completeness of the presented material. While drawing the time waveforms in Fig. 4.14, dead time was neglected.
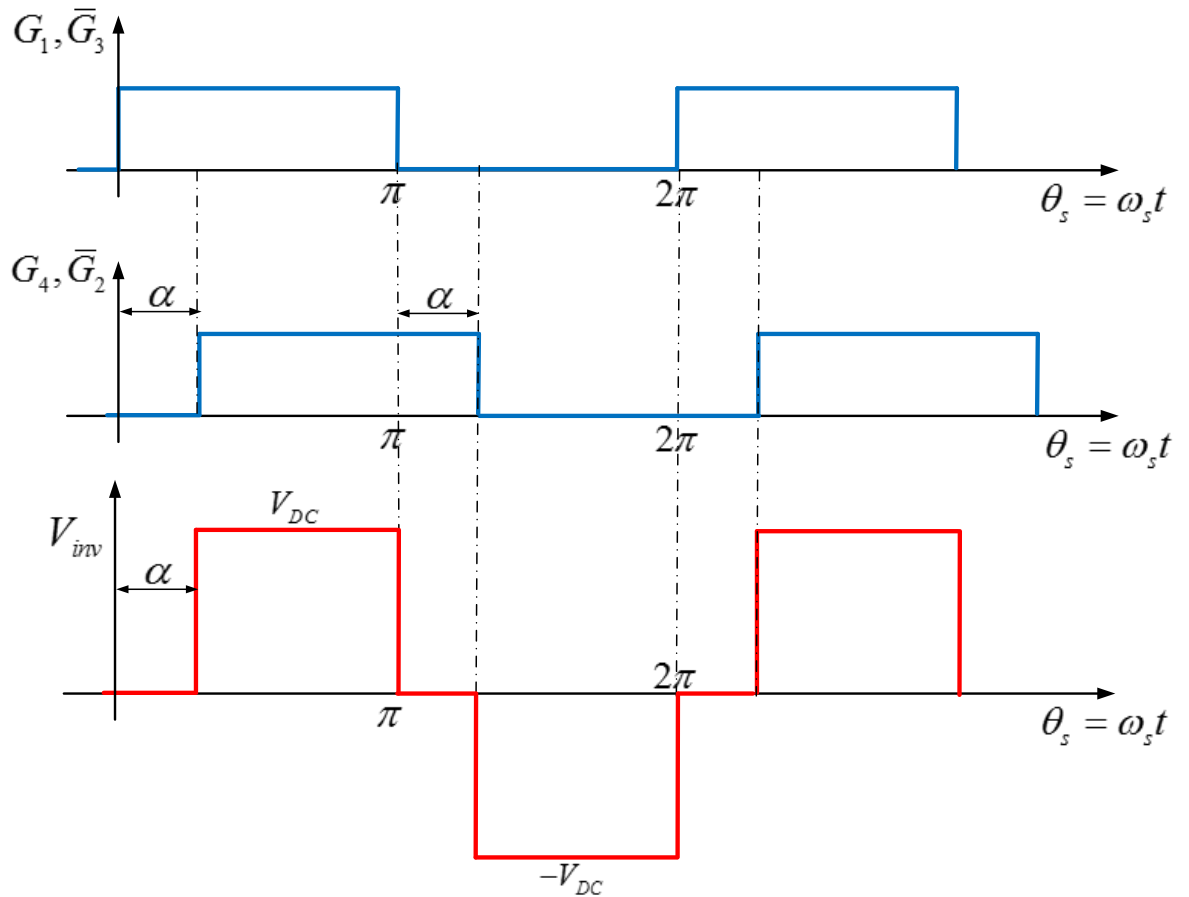
Fig. 4.14: Typical inverter waveforms for the Symmetric Voltage Cancelation control strategy ©[2015] IEEE.

Chapter 5

A Sensorless Feed-forward Power Transfer Control algorithm for In-Motion Wireless Power Transfer System Based on Lumped Transmitting Coil Structure

The promise of higher power and energy efficiency of lumped transmitting coil structure can only be realized with synchronized energizing of the transmitter coils. Synchronization could be accomplished through position detection and vehicular communication devices, but those devices are expensive and still lack the speed and accuracy necessary for proper synchronization. Thus, to ensure effective power transfer, there is a need for a sensorless power transfer control. This chapter delves deep into the characteristics of in-motion wireless power transfer based on lumped transmitting coils and characterizes the power transfer efficiency, as well as power loss. Building upon this analysis, a novel position sensorless feed-forward power transfer control algorithm is proposed. The controller coefficients are analyzed in Section 5.7. After that, the controller is verified with analytical simulations, physical circuit based simulations and practical hardware.

5.1 Transfer Power Profile in Dynamic WPT Systems

The transferred power can be very easily modeled by the reflected resistance from secondary to primary, R_r. The structure of the secondary resonant circuit determines the expression of reflected resistance. For two most common topologies, series and parallel compensations, these expressions are respectively [64]:

$$R_{r,s} = \frac{\omega_s^2 M(t)^2}{R_{L,ac}}$$

$$R_{r,p} = \frac{M(t)^2}{L_r^2} R_{L,ac}$$

where $M(t)$ is mutual coupling between two coils, $R_{L,ac}$ is equivalent AC load closing the resonant circuit at the receiver, and L_r is the self-inductance of the receiver coil. $R_{L,ac}$ depends on the DC load at the output and can be varied by the action of the controller at the receiver. To simplify the analysis below, $R_{L,ac}$ is considered to be constant during the interval when the receiver coil passes above the transmitter coil.

Parallel compensation is preferred at the receiver for in-motion applications since, associated with a boost converter at the receiver, it can provide load charging even at low coupling conditions, meaning when the induced voltage at the receiver is low. On the other hand, series compensation and associated buck converter can operate only when the misalignment is low and when enough voltage is induced in the receiver coil. This features positively discriminate parallel compensation for the applications where misalignment is part of a regular operation cycle.

Considering a parallel compensation at the receiver and constant AC load $R_{L,ac}$, reflected resistance becomes a function of mutual inductance $M(t)$ that varies over time. More precisely, apart from the shape of the coils, M will depend on vehicle speed and coil misalignment, as it was discussed and demonstrated in Chapter 4:

$$M(t) = M(t, v, l) \tag{5.1}$$

where v is vehicle speed and l is distance between two coils when they are closest to each other. To illustrate the previous discussion, normalized mutual inductance time waveforms of the identical single-turn coils are presented for two different velocities ($v = 36$ km/h and $v = 72$ km/h), and measured for aligned and misaligned situations ($l = 0$ and $l = d/4$). Coil radius is $d = 343$ mm and vertical distance $d = 100$ mm in Fig. 5.1. Both diagrams

are normalized by dividing the mutual inductance with the maximum mutual inductance value measured when the coils are perfectly aligned.

Transferred power to a vehicle is a function of bot transmitter control variables, as well as vehicle driving parameters:

$$P_t = \left(\frac{V_{inv,1}}{\omega_s L_s}\right)^2 \frac{\omega_s^2 M(t)^2}{R_{L,ac}} = \frac{V_{inv,1}^2}{R_{L,ac}}\frac{M(t)^2}{L_s^2} \tag{5.2}$$

Coupling coefficient, $k(t)$, can be expressed as:

$$k(t) = \frac{M(t)}{\sqrt{L_t L_r}} \tag{5.3}$$

Introduction of coupling coefficient modifies the power expression of (5.2) as:

$$P_t(t) = \frac{V_{inv,1}^2}{R_{L,ac}}\frac{L_t L_r}{L_s^2}k(t)^2 \tag{5.4}$$

From (5.4) one can see that power P_t monotonically increases with the inverter output
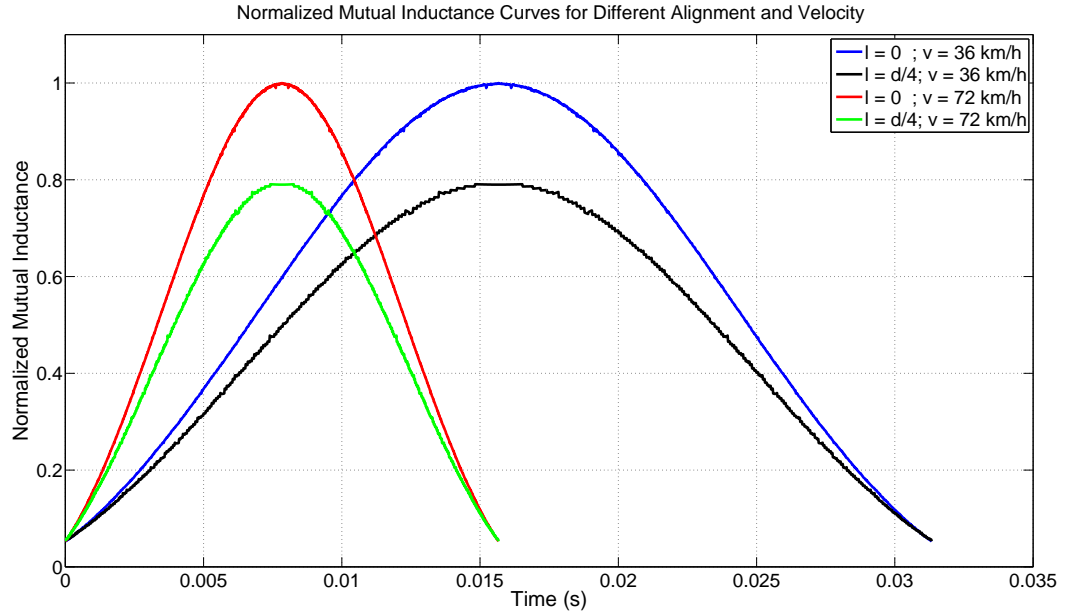
Fig. 5.1: Normalized mutual inductance time waveforms ©[2015] IEEE.

voltage. Therefore, maximum instantaneous power can be obtained if the rated inverter output voltage $V_{inv,r}$ is provided, which corresponds to the rated DC link voltage and no phase shift between the gate signals:

$$P_{t,max}(t) = P_t(V_{inv,1} = V_{inv,1,r}, t) = P_t(V_{DC} = V_{DC,max}, \alpha = 0, t) = \frac{V_{inv,1,r}^2}{R_{L,ac}} \frac{L_t L_r}{L_s^2} k(t)^2$$

(5.5)

After introducing $P_{t,NOM}$ which represents nominal power exchange between two perfectly aligned coils:

$$P_{t,nom} = \frac{V_{inv,1,r}^2}{R_{L,ac}} \frac{L_t L_r}{L_s^2} k_0^2$$

(5.6)

Expressions (5.6) and (5.4) can rewritten as:

$$P_t(t) = P_{t,nom}(t)(V_{inv,1}^* k(t)^*)^2$$

(5.7)

$$P_t(t) = P_{t,nom}(t)(k(t)^*)^2$$

(5.8)

where V_{inv}^* and k^* represent normalized values of the inverter output voltage and the coupling coefficient, respectively:

$$k(t)^* = \frac{k(t)}{k_0}$$

$$V_{inv,1}^* = \frac{V_{inv,1}}{V_{inv,1,r}}$$

Nominal power does not necessarily represent the maximum power that two coils can exchange since the receiver controller still has capacity to vary AC resistance $R_{L,ac}$ requiring more power. By reducing ac load $R_{L,ac}$, the receiver can demand more power, and the transmitter would provide it if the required power rating is below the maximum power that transmitter system can deliver. Whether the transmitter charger would respond to the request depends on the transmitter power rating $P_{t,max}$, which must not be exceeded: $P_t < P_{t,max}$. This action of the receiver might be necessary if, due to misalignment, the vehicle receives less power than it needs, and the misalignment problem cannot be resolved.

5.2 Analytical Modeling of the IPT System

Analytical simulations require analytical system modeling. The IPT system consists of an inverter feeding a LCL network at the primary side. The secondary side is parallel compensated which is followed by a power converter conditioning the power for the load. In this particular system, the effect of the receiver can be accurately modeled by only considering the impedance it reflects to the primary side. As the power transferred is a function of load resistance and track current, the knowledge of reflected impedance is enough to calculate the transferred power. In a parallel compensated secondary, the reflected resistance and reactance are respectively:

$$R_{txf} = \frac{M(t)^2}{L_r^2} R_{L,ac} \tag{5.9}$$

$$X_{txf} = -j\frac{\omega M(t)^2}{L_r} \tag{5.10}$$

Fig. 5.2 shows the equivalent circuit of the primary side of the IPT system. The equivalent circuit is essentially a current source feeding a track inductor and reflected impedance in series. The current through the inductor and the power transferred are independent of the reactance in the branch as it is fed by a constant current source. Thus, to model the power transfer variation, the modeling of the load variation is sufficient. If an assumption is made that the dynamics of the load variation is much slower than the response of the reso-
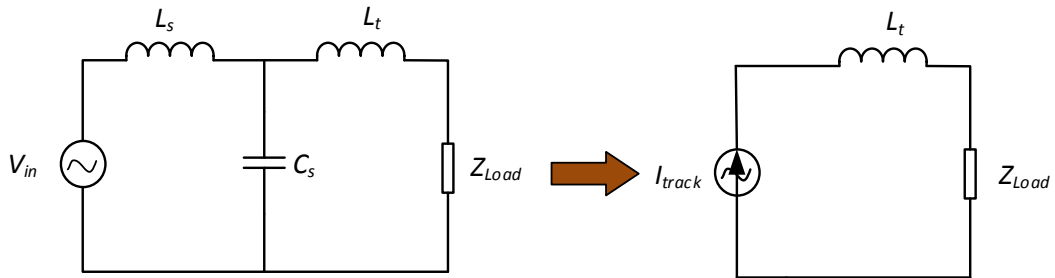
Fig. 5.2: Simplification of the primary equivalent circuit.

nant tank to source current variation, then it is valid to model the primary resonant circuit in steady state and analyze the effect of the proposed controller. The current through the inductor L_s, can be related with the input voltage through the linear relation:

$$I_{track} = \frac{V_{inv,1}}{\omega L_s} \tag{5.11}$$

The load can be modeled as a resistor in series with a track inductor, so it is very intuitive to think of the system as a current source feeding a load resistor.

$$P_{txf} = I_{track}^2 R_{txf} \tag{5.12}$$

The effect of in motion power transfer in the model compared to stationary wireless power transfer is variable load resistance compared to fixed load resistance. So, it is important to understand the nature of the resistance variation with different misalignments. Resistance seen from the primary is proportional to the square of the mutual inductance. Thus, for a certain constant load in the secondary, it suffices to have the knowledge of mutual inductance variation to derive the resistance variation curve.

5.3 Power Loss Profile in Dynamic WIPT Systems

Unlike other power converter and system applications, resonant converters in dynamic WIPT may operate for a substantial amount of time without transferring much power. That operation mode is typically characterized by low power efficiency. Therefore, a good understanding of the loss mechanisms should be developed and optimal operation point should be selected not only for the full load, but for the entire operating range, as well. Transmitter side power loss is a complex function of the transferred power P_t, supply voltage V_{DC}, inverter phase shift angle α and circuit parameters:

$$P_{t,\gamma}(t) = P_{t,\gamma}(P_t, V_{DC}, \alpha) \tag{5.13}$$

The way the inverter output voltage is generated does not only affect the switching losses of the inverter and the buck converter (if employed) but it also affects the loss in the compensation elements due to high-order current harmonics flowing dominantly through the L_s and C_P. On the other hand, loss in the transmitter coil branch is solely dependent on the current flowing through it, and, consequently, on the power transferred to the receiver. Most of the approaches reported in scholar literature identify the transmitter and receiver coils' loss as a dominant factor, and try to optimize the operation after neglecting other sources. While that might be true for mid- and far-range WIPT systems, this premise becomes inaccurate for short distance high-power charging systems, as it was demonstrated in [41]. The authors in [41] provided detailed description of loss distribution in a 5 kW wireless charging system, proving that maximum efficiency of the magnetic couplers can be even higher than the efficiency of the hard-switched primary supply implying that more attention should be paid to their operation. The situation is even more in favor of WIPT pads when the transferred power is reduced, since current independent portion of the switching loss in source converters does not vary much with the load.

Accurate loss modeling is a challenging task, and an everlasting topic of scholar research. In [41] a comprehensive loss model is developed for the entire WIPT structure. However, it includes only the linear component of conductive loss, while switching loss and temperature dependent variation of the circuit parameters are neglected due to complex nature. As an outcome, the authors reported measured system efficiency in laboratory conditions typically being as close as 5% from the analytically calculated value, while for some operation conditions such discrepancy becomes as large as 10% . Although those numbers may seem small, they usually represent an underestimation of the converter loss for up to 50%.

Considering that a WIPT system would typically be available for extensive testing and

verification before an approval and implementation, we adopted a different approach here, which is based on efficiency mapping of the primary system for different values of P_t and V_{inv} (or α). The data collected during the on-site or laboratory tests would be interpolated to serve for power loss estimation during the real-time operation:

$$\eta_P = \eta_P(P_{DC}, V_{inv,1}) = \eta_P(P_{DC}, \alpha) \tag{5.14}$$

The quality of the estimator could be improved by including temperature dependent parameters, but that is left for some future research.

5.4 Transferred Energy and Energy Efficiency in Dynamic WIPT Systems

Total energy transferred to a vehicle during a vehicle transition over a transmitting pad is just the integration of power over the period the vehicle is over the pad. The mathematical formulation can be obtained as:

$$W_t = \int\limits_{-\frac{1}{2}T_m}^{\frac{1}{2}T_m} P_t(t)dt = P_{t,nom} \int\limits_{-\frac{1}{2}T_m}^{\frac{1}{2}T_m} \left(V_{inv,1}^* k^*(t)\right)^2 dt \tag{5.15}$$

where T_m is the time interval during which two coils demonstrate detectable power transfer. Time scale is adjusted to position $t = 0$ which is the moment when two coils are closest to each other.

If the maximum voltage at the output of the inverter is maintained through the entire power transfer interval ($V_{inv} = V_{inv,r}$) maximum absolute energy will be delivered to the load for the given vehicle speed, alignment, and load at the receiver:

$$W_{t,max} = P_{t,nom} \int\limits_{-\frac{1}{2}T_m}^{\frac{1}{2}T_m} (k^*(t))^2 dt \tag{5.16}$$

Finally, (5.15) can be normalized by (5.16) to get the percentage of the maximum energy that would be delivered for the particular energy power exchange event:

$$W_t^* = \frac{W_t}{W_{t,max}} = \frac{\int\limits_{-\frac{1}{2}T_m}^{\frac{1}{2}T_m} \left(V_{inv,1}^* k^*(t)\right)^2 dt}{\int\limits_{-\frac{1}{2}T_m}^{\frac{1}{2}T_m} (k^*(t))^2 dt} \tag{5.17}$$

Now, there can be multiple voltage profiles (5.18) that would result in the same W_t^* over the interval T_m:

$$V_{inv,1}^* = V_{inv,1}^*(t) \tag{5.18}$$

However, those profiles are not equally efficient. As the system is not an instantaneous system, the power efficiency is not an adequate parameter. Power efficiency will be low at more misaligned state and increase to highly efficient in the aligned states. Thus, an efficient profile will transfer more energy in the efficient region compared to the inefficient one. So, power efficiency is not an adequate parameter to assess the power profile but, energy efficiency coefficient is more suitable. Energy efficiency will quantify the efficiency of the total energy transferred over the period of energy transfer. The analytical formulation is given below:

$$\eta_E = \frac{W_t}{W_t + \int\limits_{-\frac{1}{2}T_m}^{\frac{1}{2}T_m} P_{t,\gamma}(t)dt} = \frac{\int\limits_{-\frac{1}{2}T_m}^{\frac{1}{2}T_m} \left(V_{inv,1}^* k^*(t)\right)^2 dt}{\int\limits_{-\frac{1}{2}T_m}^{\frac{1}{2}T_m} \left(V_{inv,1}^* k^*(t)\right)^2 dt + \int\limits_{-\frac{1}{2}T_m}^{\frac{1}{2}T_m} P_{t,\gamma}^*(t)dt} \tag{5.19}$$

where $P_{t,\gamma}^*$ represents power loss normalized by the nominal power $P_{t,nom}$:

$$P_{t,\gamma}^*(t) = \frac{P_{t,\gamma}(t)}{P_{t,nom}} \tag{5.20}$$

From the previous expression one can see that maximum energy efficiency would be obtained for the voltage profile which satisfies energy requirements and, at the same time,

produces minimum energy loss in the transmitter subsystem. The identification of the optimum voltage profile and corresponding phase angle references for the inverter are central topics in the sections below.

5.5 Case study: Transferred Power and Energy vs. Power and Energy Efficiency in Dynamic WIPT Systems

To support the analysis above, a case study is presented here for a dynamic WIPT system whose parameters are summarized in Table 5.1. In this study, two driving trajectories are considered: the first one is perfectly centered, creating zero lateral misalignment with the transmitter coil, while the second trajectory is misaligned with the misalignment being half of coil radius $l = rr/2 = rt/2$. WIPT system transfers nominal power $P_{t,nom} = 150$ W when the coils are perfectly aligned and the transmitter coil is fully energized. Coils are considered to be circular and identical ($r_r = r_t = 0.5$ m), and relative speed of the receiver coil with respect to the transmitter coil is set to 10 m/s. Power transfer is terminated when the transferred power drops below 2.5% of the nominal value $P_{t,nom}$, which consequently defines the charging interval T_m.

Table 5.1: Case study: System specifications and component values

Parameter	Unit	Value
Primary coil inductance, L_t	μH	283.67
Primary coil resistance, ESR_{Lt}	Ω	0.1763
Primary inductor inductance, L_s	μH	73.49
Secondary coil inductance, L_r	μH	8.71
Secondary coil resistance, ESR_{Lr}	Ω	0.02

Let us assume that the time profiles of the coupling coefficient k are determined as a result of coil simulations or experimental tests and given in Fig. 5.3. While in a practical case inverter voltage can take any value between 0 and $V_{inv,1,r}$, in this case study only two discrete values will be consider: i) inverter voltage is zero and system does not transfer power (neither does it generate loss); ii) inverter produces rated voltage at the output transferring the maximum power for the given coupling conditions and receiver load. In Fig. 5.4, power efficiency η_P is plotted as a function of transferred power P_t for rated voltage

at the output of the inverter $V_{inv,1} = V_{inv,1,r}$. From the diagram in Fig. 5.4, one can notice that transmitter efficiency monotonically increases with the amount of power delivered to the load. This implies that the power will be transferred most efficiently if the power burst is synchronized with the interval of strong coupling, and rated voltage is applied at the transmitter side.

One concludes that energy efficiency is considerably smaller than the maximum value of power efficiency. The reason for this are low efficient power transfer zones where negligible energy is transferred but still considerable loss is dissipated at the transmitter. Discrepancy between those two performance indexes could be reduced if less than the maximum energy is required by the vehicle. In that case, the transmitter controller could narrow the interval during which its coil is energized, and position the excitation time to capture the central, highly efficient part of the power transfer profile. By extending the interval T_s from zero to T_m, transferred energy can be increased, but it is accompanied by lower energy efficiency. The simulation result for both transferred energy and the energy efficiency are given in Fig. 5.5 as a function of the normalized interval $T_s^* = T_s/T_m$.

In the discussion above, only the case where the vehicle goes over the coil in the ground with perfect alignment is covered, not the misaligned case shown in Fig. 5.6. In this case, the vehicle receives the maximum possible energy from the track. Now, if the vehicle does not receive enough energy as it commands, it has three possible energy options. First, to increase load resistance seen by the primary by increasing the load resistance seen by the secondary resonant tank. The duty cycle of the converter in the secondary side can be changed to achieve this effect. The energy transferred increases, but the secondary quality factor increases, as well. The increased secondary quality factor results in higher circulating current in receiver's passive components and thus decreased efficiency. The second option is to ask for more energy from the primary. In this case, the primary voltage would be shaped to give more energy. This will also result in relatively inefficient solutions as the primary will have to transfer energy in the peripheral and more inefficient regions. The third and most efficient solution for the vehicle is to align itself.
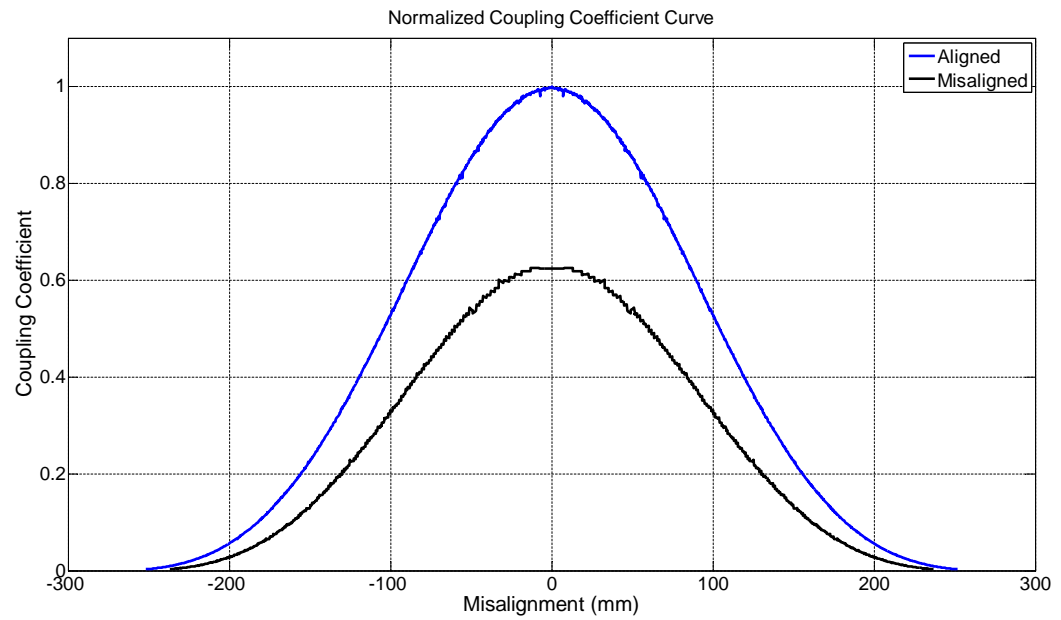
Fig. 5.3: Profile of the coupling coefficient k for two different vehicle alignments: aligned and misaligned by $d/4$.
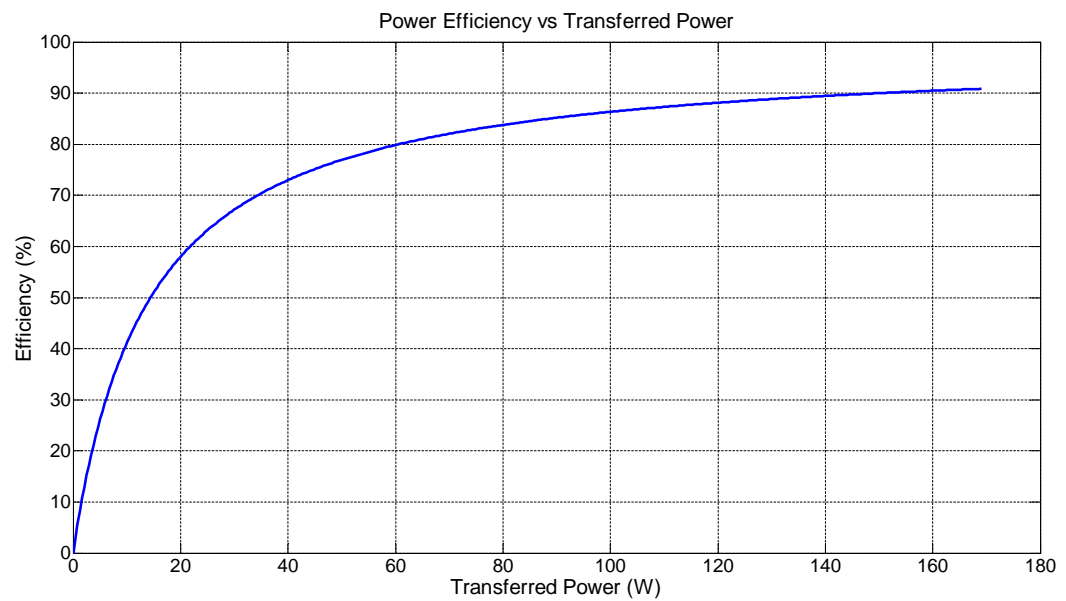

Fig. 5.4: Power efficiency η_P as a function of transferred power P_t for the rated inverter voltage ©[2015] IEEE.
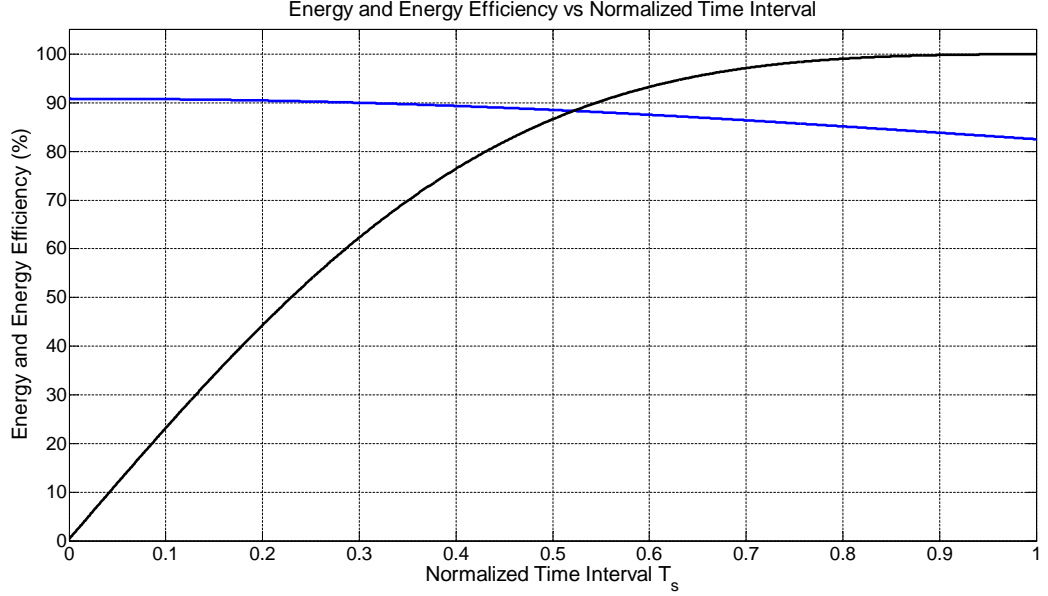
Fig. 5.5: Transferred energy W_t and energy efficiency η_E as a function of normalized interval T_s^* ©[2015] IEEE.

5.6 Description of Control Strategies

Results in Fig. 5.5 reveal that for every vehicle trajectory, there is an optimum length of the interval T_s that would result in transferring the required amount of energy. However, the coupling coefficient profile $k(t)$ is unknown a-priori, as well as the right time instant when the maximum coupling would occur. On the other hand, the information available to the controller at every moment is the transferred power to the load, which can be determined from the measured DC power P_{DC} after subtracting estimated value of the power loss. Therefore, in this thesis, a control strategy is proposed: according to this strategy, the controller makes decision about the optimum voltage energizing profile based only on the actual value of the transfer power and energy requirement factor m. The structure of the controller algorithm is given in Fig. 5.7.

Although centrally aligned rectangular curve can transfer the required amount of energy most efficiently, it requires accurate detection of the vehicle position. Eliminating this requirement requires a passive detection of the peak alignment without any position detection mechanism, and the transferred power as the only measured parameter. The proposed
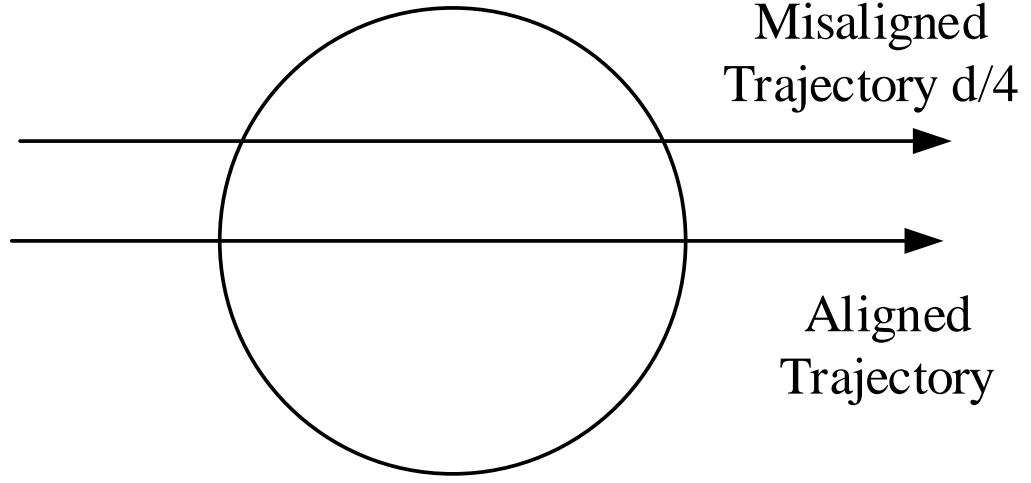
Fig. 5.6: Aligned and misaligned trajectories.
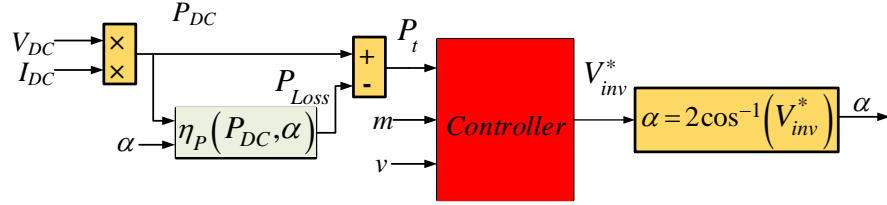
Fig. 5.7: Block diagram of the proposed controller ©[2015] IEEE.

profile is to use a exponential profile which will increase with more alignment, meaning higher power. A normalized power transfer value, $P_t/P_{t,max}$ is calculated and then it is exponentiated and multiplied with two parameters. Appropriate choice of these parameters can ensure a certain amount of energy transferred. The proposed algorithm is presented in (5.21):

$$I_t = \min \left[A(m)I_{max} \left(\frac{P_{dc}}{P_{t,max}} \right)^{g(m)}, I_{t,max} \right] \tag{5.21}$$

Essentially, the LCL network can act as a current source feeding the track, thus enabling a control of the track current and therefore ensuring the controller operation. Although,

this equation conveys the physical meaning of the system quite succinctly, there is a lack of clarity from the inverter voltage control point of view. Chapter 4 identified phase shift control as the ideal control variable to control the resonant tank voltage. So, the controller is simplified and written in terms of the normalized inverter voltage in (5.23):

$$\frac{V_{in}}{\omega L_s} = \min \left[A(m) \frac{V_{max}}{\omega L_s} \left(\frac{P_{dc}}{P_{t,max}} \right)^{g(m)}, \frac{V_{max}}{\omega L_s} \right] \tag{5.22}$$

$$v^*_{inv,1} = \min \left[A(m) \left(\frac{P_{dc}}{P_{t,max}} \right)^{g(m)}, 1 \right] \tag{5.23}$$

Here, I_t is the track current, I_{max} is the maximum current through the track, $A(m)$ and $g(m)$ are the two coefficients of the control algorithm. The effect of these two coefficients is analyzed both analytically and numerically in the following text.

5.7 Study of Effect of Controller Coefficient Variation on System Performance

The controller coefficients determine both the amount of energy transfer, as well as the efficiency of that energy transfer. There is a strong need to analyze the limit of these controller coefficients and its general effect on the power transfer. After the general effect is analyzed, the choice of appropriate controller coefficient is necessary to ensure controller energy transfer in an efficient manner. These two aspects are the central topics of discussion in this section.

5.7.1 Sign and Limit of the Coefficient

The $g(m)$ quantity must have a positive sign. The reason lies in the characteristic of the waveform. In the discussions above, we concluded that the waveform should be bell-shaped in nature. This means the first part of the waveform which starts from a misaligned state and ends in aligned state must be exponentially increasing. The other side, meaning the side where the alignment reduces, has to be the opposite: exponentially decaying. In the heart of the control equation is the ratio $P_{dc}/P_{t,max}$, which controls the

nature of the waveform. Here, the maximum power quantity, $P_{t,max}$ is a constant value, while the dc power quantity, P_{dc} is an exponential curve. So, the quantity, $P_{dc}/P_{t,max}$ has essentially an exponential waveform with the highest value of 1 in the middle. So, a positive exponential value is needed for realizing increasing exponential waveform at the beginning and decreasing exponential waveform in the end.

Simulations show that if one uses 0.5 or above as the exponential value the applied current waveform becomes a zero value. The reason behind needs a closer inspection.

$$v_{inv,1}^{*} = \min \left[A(m) \left(\frac{P_{dc}}{P_{t,max}} \right)^{g(m)}, 1 \right] \tag{5.24}$$

This expression contains an inherent exponential behavior. The behavior comes from the dc power value.

$$\left(\frac{P_{dc}}{P_{t,max}} \right)^{g(m)} = \left(\frac{I_t^2 R_{ref}}{I_{max}^2 R_{max}} \right)^{g(m)} = \left(\frac{I_t^2}{I_{max}^2} \right)^{g(m)} \left(\frac{R_{ref}}{R_{max}} \right)^{g(m)} \tag{5.25}$$

$$\Rightarrow \left(\frac{P_{dc}}{P_{t,max}} \right)^{g(m)} = \left(\frac{I_t}{I_{max}} \right)^{2g(m)} \left(\frac{R_{ref}}{R_{max}} \right)^{g(m)} \tag{5.26}$$

Now, the curve can be viewed as multiplication of two curves. The second curve $\left(\frac{R_{ref}}{R_{max}} \right)^{g(m)}$ holds the answer. The variation of resistance comes from variation of the mutual inductance. The reflected resistance is proportional to the square of the mutual inductance. So, the ratio reduces to:

$$\left(\frac{R_{ref}}{R_{max}} \right)^{g(m)} = \left(\frac{CM^2}{CM_{max}^2} \right)^{g(m)} = \left(\frac{M}{M_{max}} \right)^{2g(m)} \tag{5.27}$$

The quantity inside is less than one, so if the exponential term is greater than one, the whole term will decrease instead of increasing. This will collapse the algorithm. This means that $2g(m)$ has to be smaller than unity, resulting in $g(m)$ being smaller than 0.5.

5.7.2 Effect of Two Factors

Any exponential curve can be modified by two parameters. One is the multiplication factor and another is the exponentiation factor. In our problem, the reflected resistance

curve has a natural concave shape. If the multiplication factor is changed, the applied current is increased but the original concave shape of the applied voltage waveform is kept intact. Fig. 4.5 shows that the inefficient areas are at the edge (misaligned), and the efficient area is in the middle (aligned). This intuition leads us to the conclusion that: if it is more important to have more energy transferred, and the efficiency is of secondary importance then the better approach is to have small $g(m)$, shown in Fig. 5.9. On the other hand if it is more important to be efficient in the energy transfer then higher $A(m)$, shown in Fig. 5.8, should be used, since it preserves the natural concave shape.

5.8   Analytical Simulation of Control Algorithm

The motivation of the analytical simulation stems from the fact that there are different possible source voltage profiles which can give the same energy to the load, but the efficiency would vary. The variation of the source voltage profile comes from the different coefficients $A(m)$ and $g(m)$. Different combinations of these coefficients result in same energy transferred albeit with different energy efficiency. This necessitates an analytical simulation, which will identify the values of $A(m)$ and $g(m)$ which give the same energy
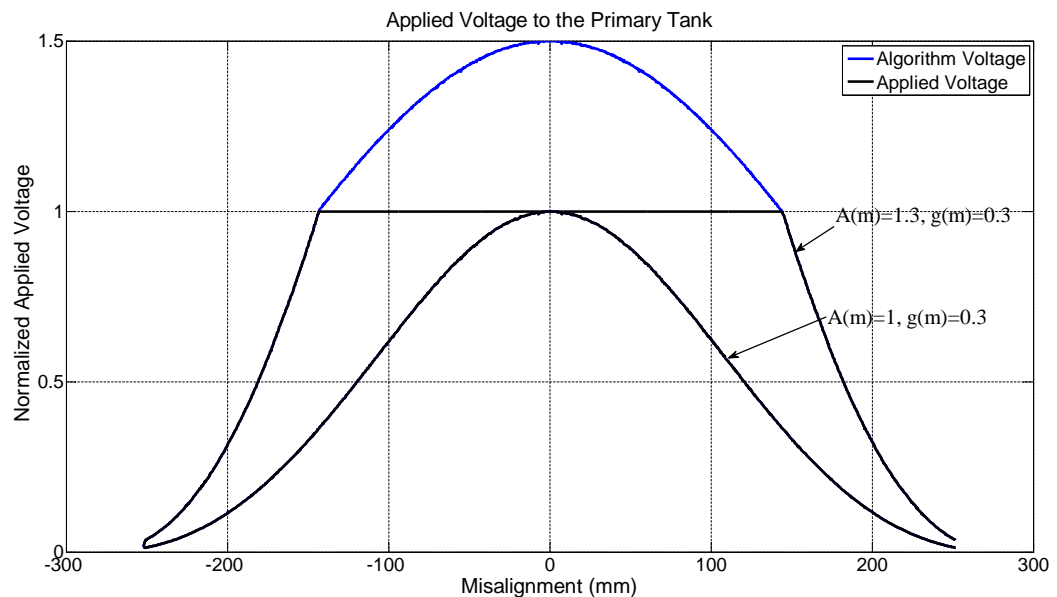

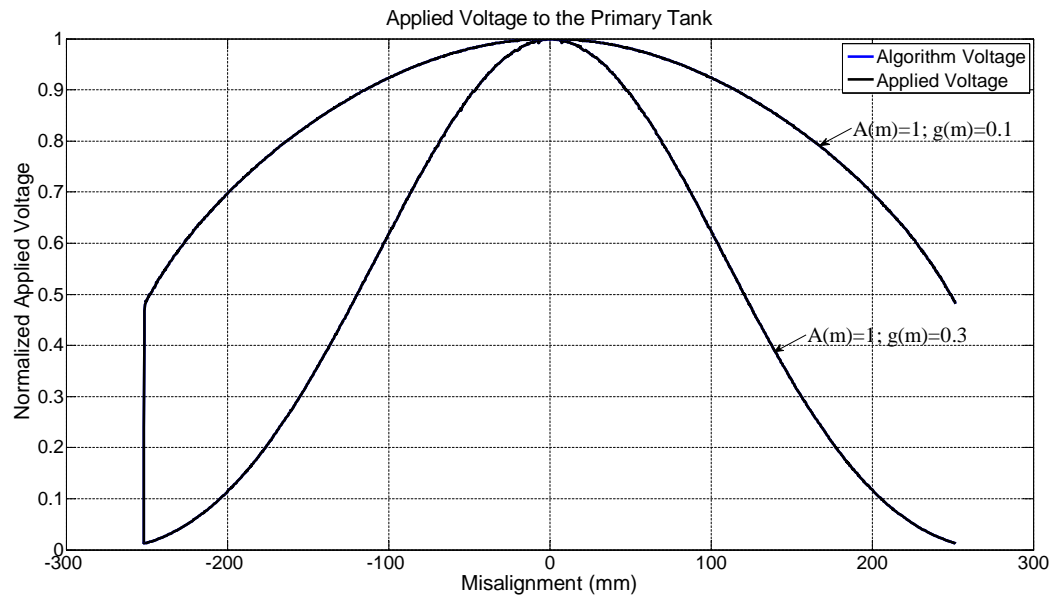Fig. 5.8: Different profiles for same g_m and different A_m.

Fig. 5.9: Different profiles for different g_m and same A_m.

transferred with maximum energy efficiency.

A two loop iterative algorithm is developed which sweeps through all possible coefficient values for $A(m)$ and $g(m)$ to find different possible energy percentages, compared to the maximum possible energy transferred: if the input voltage were the maximum for the whole period. Then, all possible $A(m)$ and $g(m)$ values corresponding to a certain energy percentage is found. The next step is to develop an algorithm which sorts out the most efficient solution for that particular energy percentage.

5.8.1 The Extraction of $A(m)$ and $g(m)$ Waveform to Percentage of Energy Relationship

Fig. 4.5 reveals that the central portion is the most efficient region and the peripheral portion is the less efficient one. This means the curves which are more centered will result in more efficient energy transfer, compared to the curves which are flatter. This knowledge is the fundamental tool to extract the most efficient curve. There are two possible ways to extract the most efficient $A(m)$ and $g(m)$ combination for a certain percentage of energy transfer. They are:

1. Choice based on intuitions on coefficient types

2. Choice based on similarity with ideal waveform

In the following text the two choices are explored in detail.

5.8.2 Choice Based on Intuitions on Coefficient Type

This technique is based on the effect of the coefficients on system performance. From the discussion of the preceding section, an understanding of $A(m)$ and $g(m)$ is gained. Lower values of $g(m)$ coefficients results in higher track current in misaligned areas. As a result, lower values of $g(m)$ waveforms have higher energy transfer in the peripheral region. Higher values of the $A(m)$ coefficients increases track current in the aligned portions more than the misaligned portions, this results in a more centered energy transfer. Thus, the higher values of $A(m)$ is more efficient and desired for a certain energy transfer.

Summarizing the concepts, we can state that we can have two requirements. The $g(m)$ coefficient should be high and the A(m) should be the low. Based on these two contradictory coefficients we can have three possible selection criteria among the curves with same percentage of energy transfer.

1. The curves with the highest $g(m)$ is first chosen, then among them the lowest possible $A(m)$ value is chosen.

2. The curves with the highest $A(m)$ is first chosen, then among them the lowest possible $g(m)$ value is chosen.

3. A new parameter, g_A is defined which takes into account both of these effects. This parameter is the ratio of $g(m)$ to $A(m)$. Both, higher values of $g(m)$ and lower values of $A(m)$ result in higher values of the parameter. The maximum of that parameter is chosen.

$$\uparrow g_A = \frac{\uparrow g(m)}{\downarrow A(m)}$$

5.8.3 Choice Based on Similarity with the Ideal Waveform

We all know that the ideal waveform is the rectangular waveform. The rectangular waveform centered on the maximum aligned point only transfers energy in the most efficient region. The most efficient exponential waveform will also have the similar characteristic, meaning it will transfer its maximum amount of energy in the central region. So, we can develop a new coefficient which will quantify this concept. The factor is termed as Energy Delivery Factor, f_{ED}. This factor is the ratio of the energy delivered for the exponential and the rectangular waveforms, in the rectangular region. Fig. 5.10 illustrates the concept. For a certain percentage of energy transferred, we know the width of the rectangular curve which corresponds to that percentage of energy transferred. Then the energy transferred by an exponential curve in that particular interval is calculated. The ratio of the energy transferred between the rectangular and exponential curve is called the Energy Delivery Factor.

$$f_{ED} = \frac{\int\limits_{t_{start}}^{t_{end}} I_{max}^2 R_{ref} dt}{\int\limits_{t_{start}}^{t_{end}} I_t^2 R_{ref} dt} \tag{5.28}$$

Here I_{max} is the maximum current, I_t is the track current of the exponential waveform and the R_{ref} is the resistance curve. This factor can be expressed in terms of the parameters proposed in the previous literature.

$$f_{ED} = \frac{\int\limits_{t_{start}}^{t_{end}} \left(\frac{V_{inv,max}}{\omega L_s}\right)^2 R_{ref} dt}{\int\limits_{t_{start}}^{t_{end}} \left(\frac{V_{inv,1}}{\omega L_s}\right)^2 R_{ref} dt} \tag{5.29}$$

$$\Rightarrow f_{ED} = \frac{\int\limits_{t_{start}}^{t_{end}} R_{ref} dt}{\int\limits_{t_{start}}^{t_{end}} (v_{inv,1}^*)^2 R_{ref} dt} \tag{5.30}$$

Fig. 5.10 shows the concept graphically. The energy under the exponential curve and

the rectangular curves are calculated and then the ratio is found. This ratio is the figure of merit for choosing the curves. Fig. 5.11, Fig. 5.12 and Fig. 5.13 has high, low and median f_{ED} factors respectively for a certain percentage of energy transfer. The curve with the highest f_{ED} is chosen.

5.8.4   Checking of the Different Algorithm Values

We know that the algorithm shapes the source voltage to deliver a certain percentage of energy. The different values of $A(m)$ and $g(m)$ can result in different source voltage profiles which can deliver the same percentage of energy. The algorithm chooses the most efficient voltage profile among them. Discussion above shows that the most efficient source voltage profile is the rectangular profile, centered around the perfectly aligned point. The most efficient exponential profile should deliver the most amount of energy in the region of the rectangular profile. Intuitively, this should result in curves which are centered around the central point, without much applied voltage in the peripheral region.

Using this knowledge of the inherent characteristic of the curve, we can make a verification of our choice of the curves. The source voltage curve with the highest energy delivery factor will naturally be centered the most. On the other hand of the spectrum, the curve which has the lowest energy delivery factor will be the one which is spread out the most.
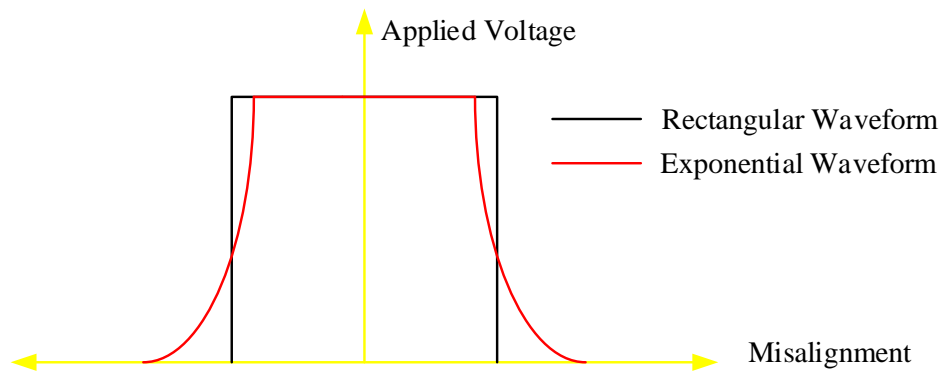

Fig. 5.10: Rectangular and Exponential Waveforms ©[2015] IEEE.

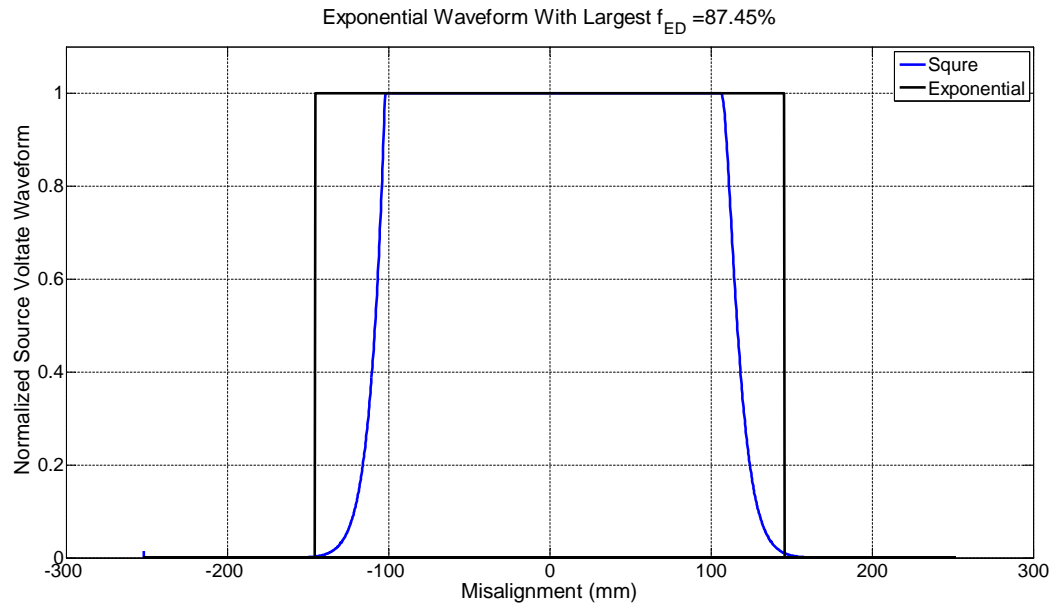The median energy delivery factor will be in the middle.

Fig. 5.11: The exponential and square rectangular waveforms which deliver 80% energy, with highest energy delivery factor
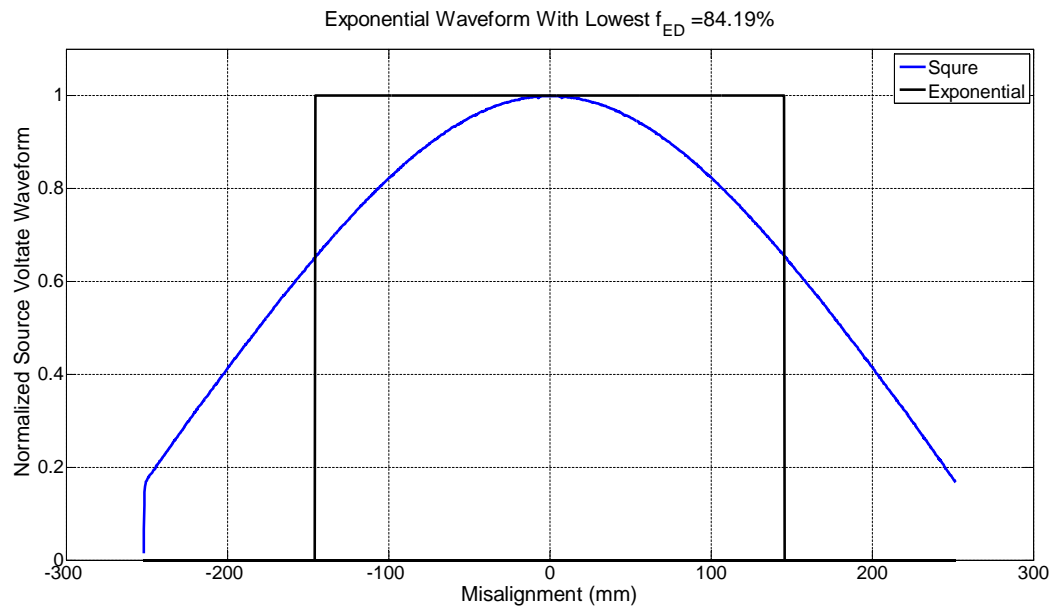

Fig. 5.12: The exponential and square rectangular waveforms which deliver 80% energy, with lowest energy delivery factor
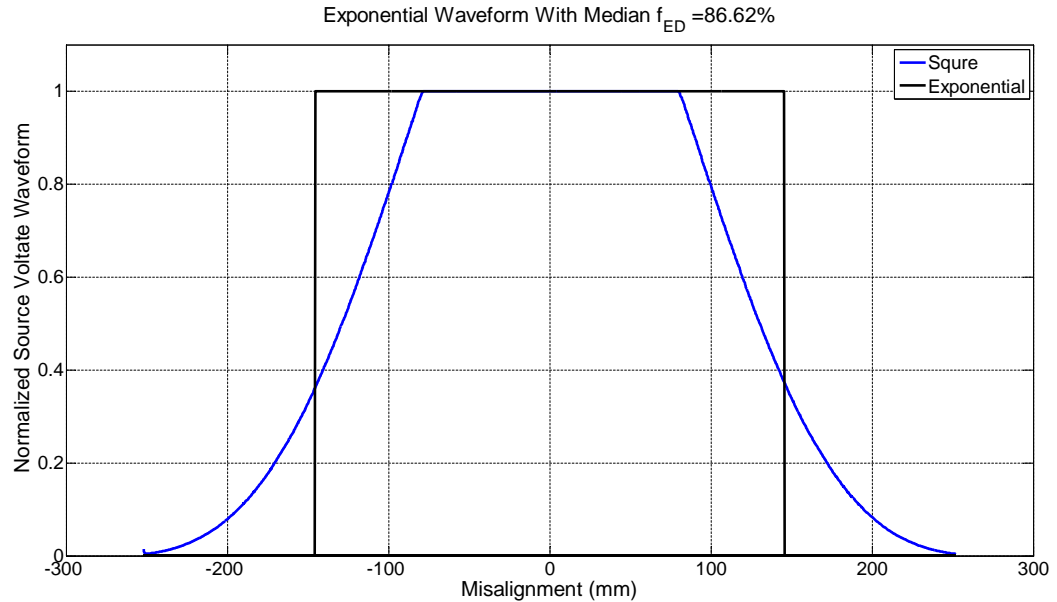
Fig. 5.13: The exponential and square rectangular waveforms which deliver 80% energy, with median energy delivery factor

5.8.5 Comparison of Different Selection Algorithms

The three different selection algorithms are compared in terms of the energy delivery factor. Energy delivery factor denotes energy delivered in the centered, meaning efficient region. The curve with the highest energy delivery factor should be the best. There are four selection algorithms. The first three are selection algorithms based on intuitions of the two factors. The performances of the four algorithms are listed in a table in Appendix A . The table shows that selection based on g_A gives very close results to the best selection based on f_{ED}. Fig. 5.14 gives a graphical illustration of the most efficient controller coefficients for certain values of energy transferred.

5.9 Physical Circuit Simulation

The simulations above are based on simplified analytical models of the dynamic wireless power transfer systems. These simulations ignore many different effects of the practical system: transients of the passive components, switching of the semiconductor components. In recent years, there has been an advancement of circuit simulation tools which can simulate
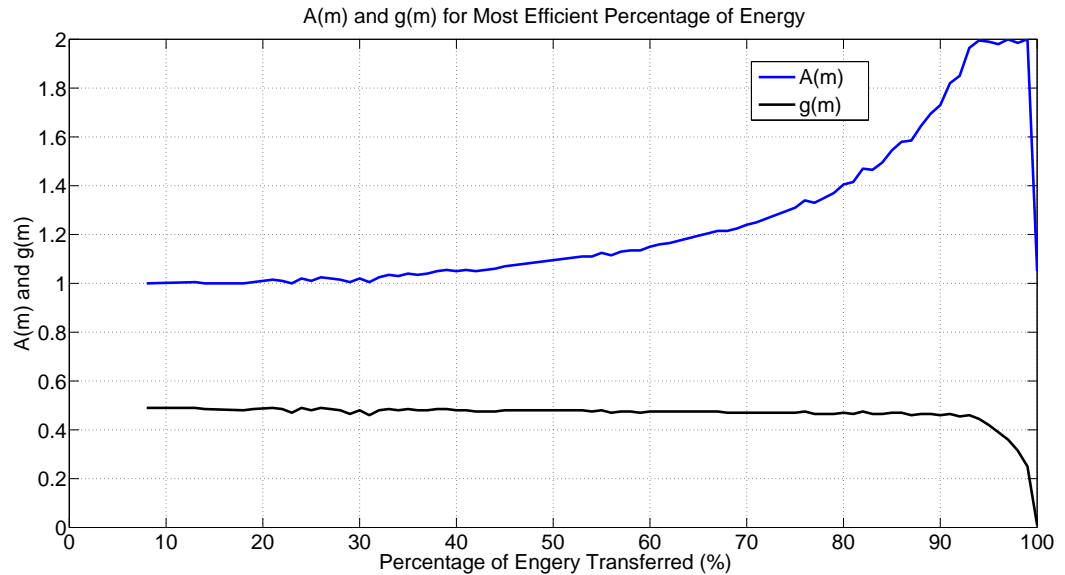
Fig. 5.14: $A(m)$ and $g(m)$ values for the most efficient energy transfer for a certain amount of energy transfer ©[2015] IEEE.

practical circuit behaviors with remarkable accuracy.

For the verification of the control algorithm above, a real time implementation was developed using MATLAB-SIMULINK. The circuit was modeled in PLECS, shown in Fig. 5.16. PLECS can interact with MATLAB-SIMULINK. This makes PLECS a very attractive option for simulation of closed loop control in power electronic systems. The basic structure of the simulation setup is given below in Fig. 5.15.

The circuit simulation block is made of an inverter followed by the LCL resonant tank. The only effect of the secondary side, is the resistance transferred to the primary.
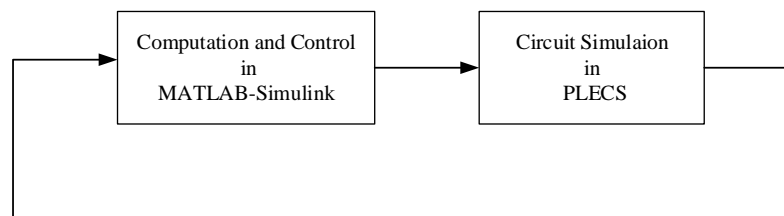

Fig. 5.15: Basic simulation structure for physical simulation of the circuit parameters.

This effect was modeled by a controlled resistor, in PLECS. The controller is developed in MATLAB-SIMULINK. The block diagram of the controller is given below in Fig. 5.17.

Circuit simulation results are presented in Table 5.2. The analytical and circuit simulations show good matching. The discrepancy can be attributed to the neglected dynamics of resonant tank and losses that have not been considered in the mathematical modeling of the system.
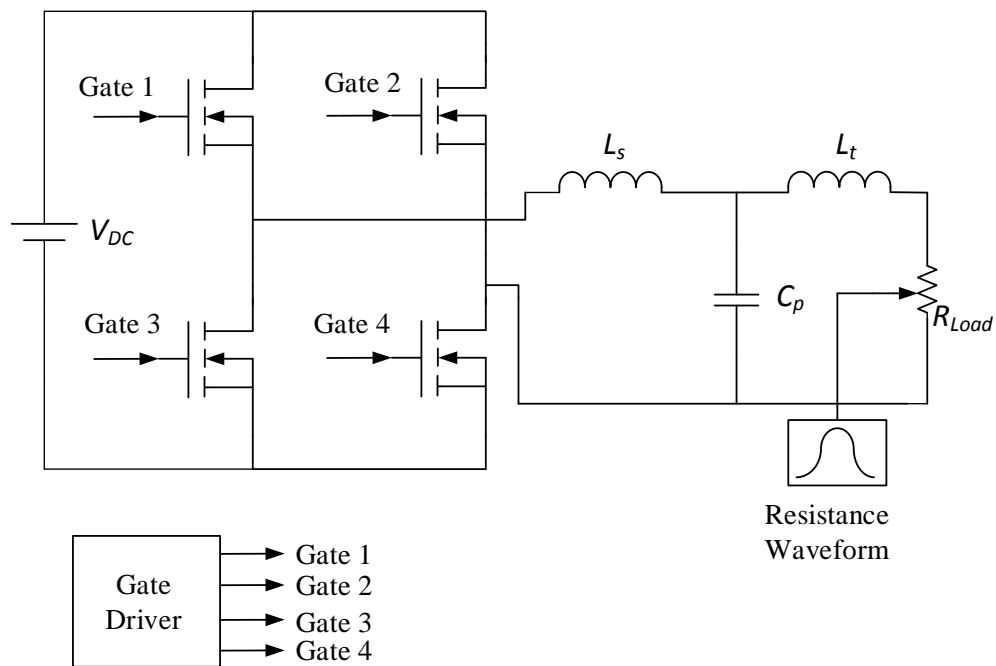

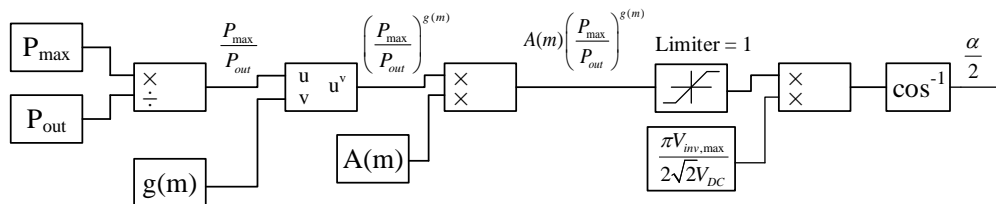Fig. 5.16: PLECS setup for the in-motion power transfer algorithm.

Fig. 5.17: Block diagram of the control algorithm implementation in MATLAB-SIMULINK.

Table 5.2: Results of circuit simulation ©[2015] IEEE.

$A(m)$	$g(m)$	Transferred energy (analytical) [%]	Transferred energy (simulation) [%]
1	0.47	23.39	22.11
1.5	0.475	83.53	78.7
1.2	0.475	65.91	58.31

5.10   Hardware Verification

A prototype was built with a table and moving cart to emulate a running vehicle over a track. Secondary coil was redesigned to reduce field redistribution with the presence of secondary load and compensation circuit. Ferrite blocks are added at the back of the coil to give a lossless path for the magnetic flux to flow. Behind the ferrite blocks, a metal sheet is added to totally block flux flow to the back, albeit in a lossy manner. Fig. 5.18 gives an illustration of the secondary side. Table 5.3 lists the parameters of the redesigned secondary coil.

Table 5.3: Secondary coil construction parameters.

Parameter	Value
Back metal length	355.6 mm
Back metal width	355.6 mm
Back metal thickness	1.45 mm
Length of ferrite	188.2 mm
Width of ferrite	28.24 mm
Thickness of ferrite	20.2 mm
Length of ferrite protrusion	57.44 mm

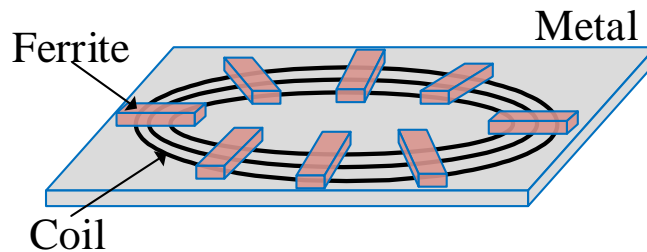After the hardware is built, an experimental measurement of the mutual inductance

Fig. 5.18: Secondary side coil construction.

is carried out. As these are AC systems, the mutual inductance variation will manifest in terms of varying magnitude of the open circuit voltage. So, there needs to be an algorithm to extract the envelope of this AC signal. Hilbert transform is employed to extract the envelope of the signal and then the remaining ripple is filtered out by low pass filtering. The mutual inductance is calculated from the open circuit voltage induced in the secondary, as it is linearly related to the track current. Fig. 5.19 presents the induced voltage waveform at the secondary with no load and fixed track current. Fig. 5.20 gives the mutual inductance profile.

Using the empirical mutual inductance profile, a new set of simulations are carried out. Then practical system waveforms are given in Fig. 5.21 and Fig. 5.23, which are
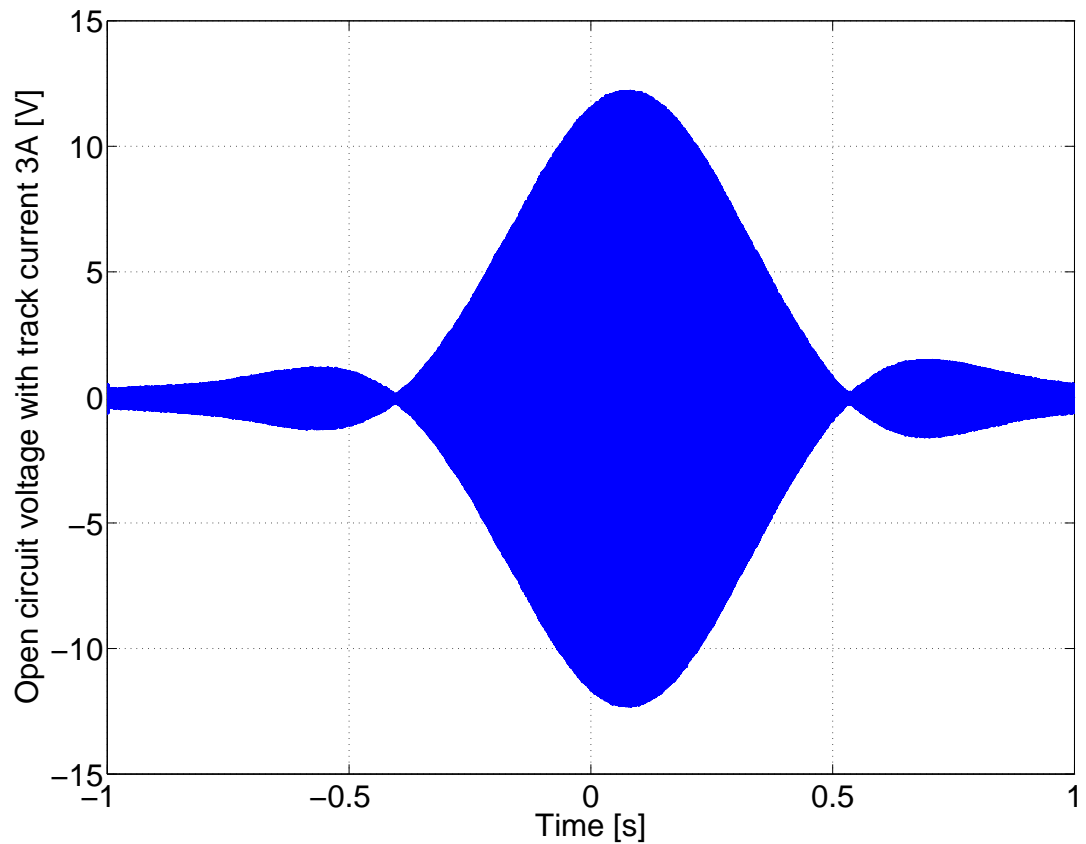

Fig. 5.19: Open circuit induced voltage at the secondary for track current of 3A.
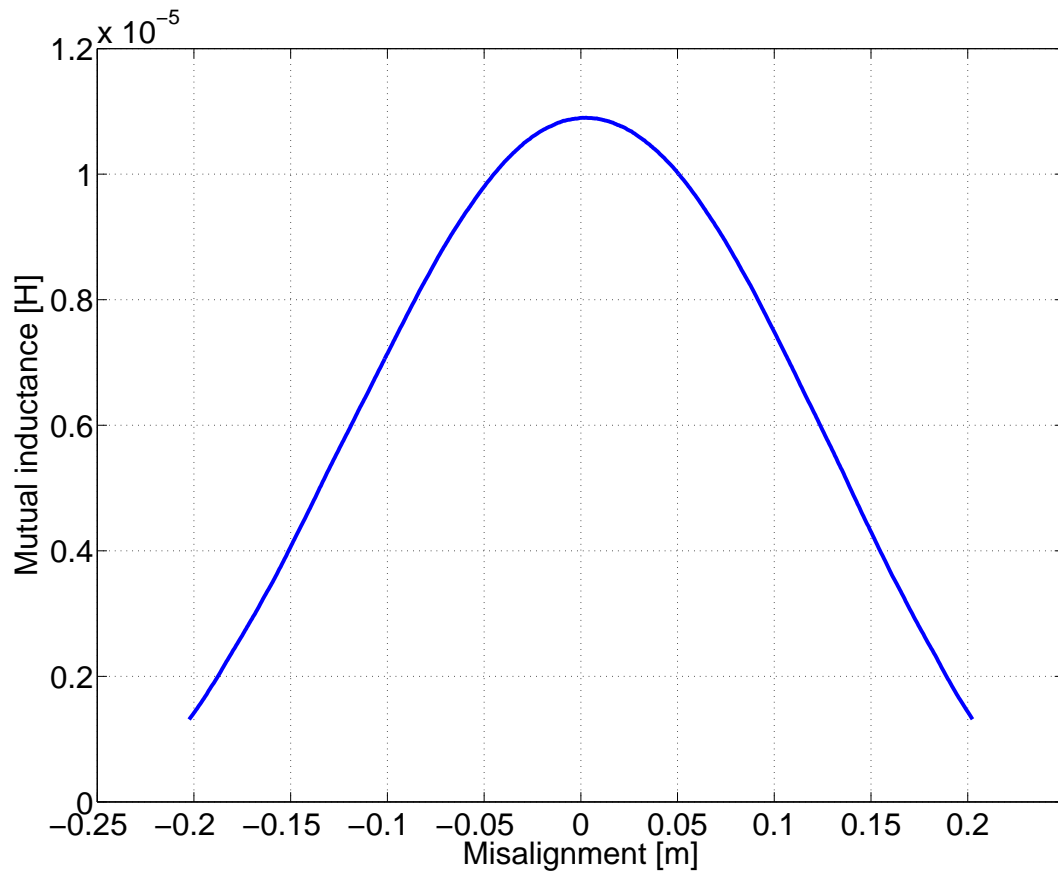
Fig. 5.20: Experimental mutual inductance profile.

uncontrolled and controlled power transfer respectively. Envelope of these two curves are presented in Fig. 5.22 and Fig. 5.24 respectively. The energy delivered is 37.9986 J for the uncontrolled case and 51.9578 J for controlled case. For controller coefficient of A_m and g_m the theoretical energy delivery percentage is 68.28%. The practical power transfer percentage is 73.13%. They show very good matching. Table 5.4 lists a comprehensive performance of the controller. Fig. 5.25 and Fig. 5.26 presents the scope capture of 70 and 90 percent energy respectively.
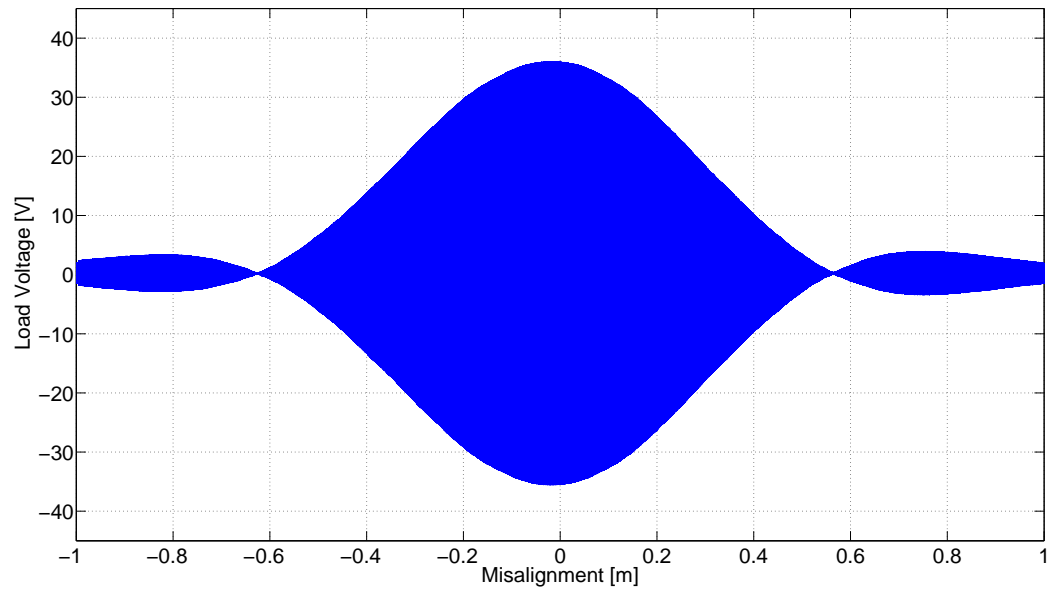
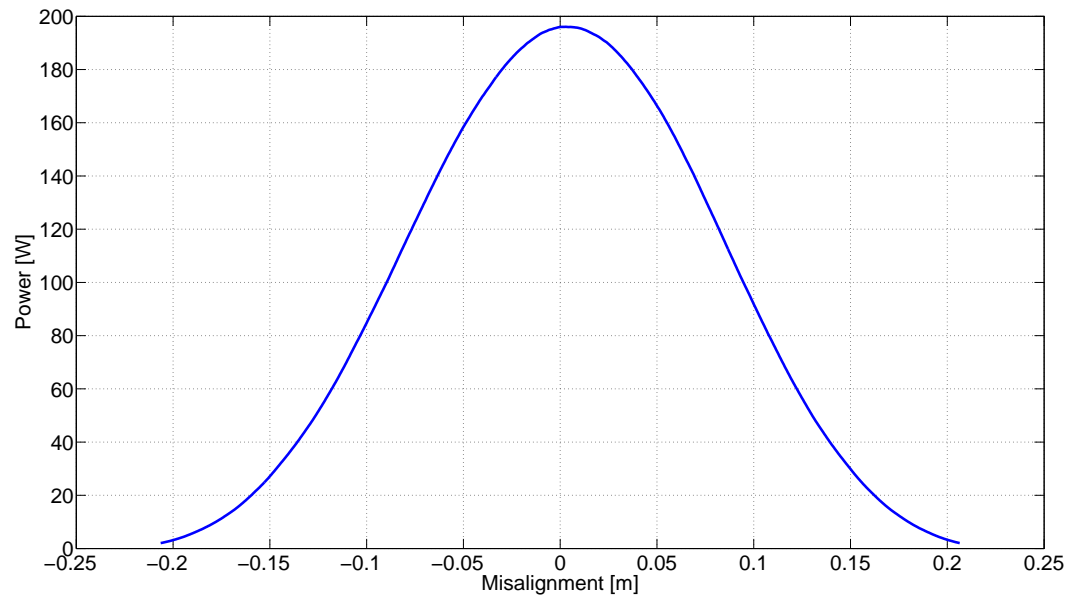Fig. 5.21: Load voltage for uncontrolled power transfer ©[2015] IEEE.

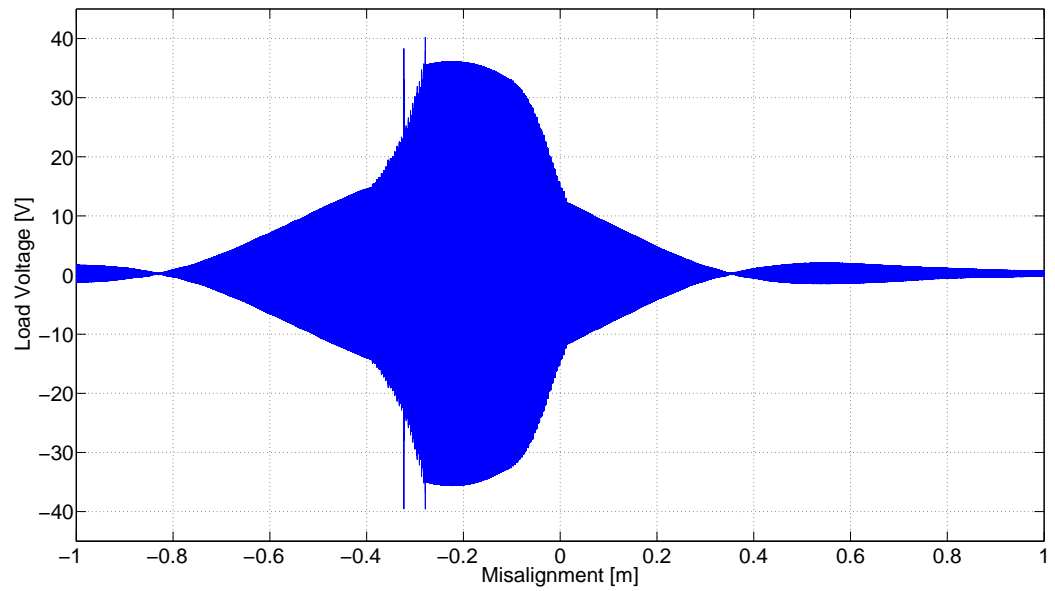Fig. 5.22: Power profile for uncontrolled power transfer.

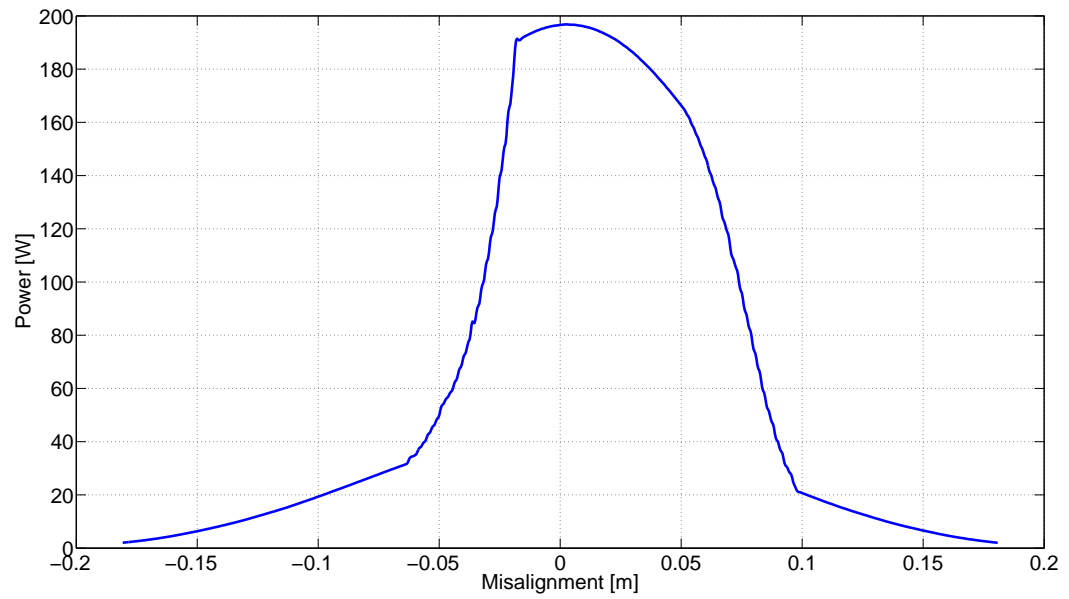Fig. 5.23: Load voltage for controlled power transfer.

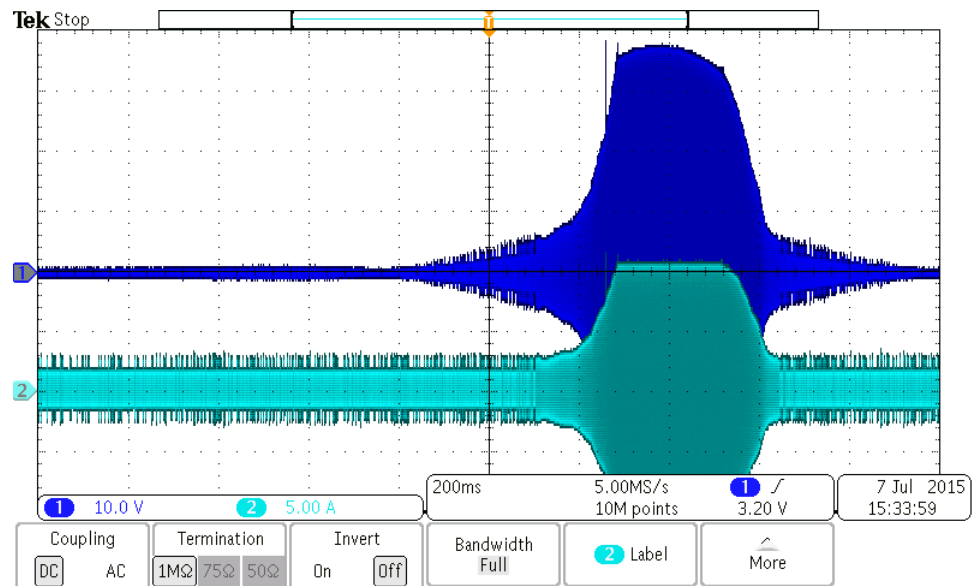Fig. 5.24: Power profile for controlled power transfer.

Fig. 5.25: Scope image for 70 percent energy transfer, blue is load voltage and cyan is track current ©[2015] IEEE.
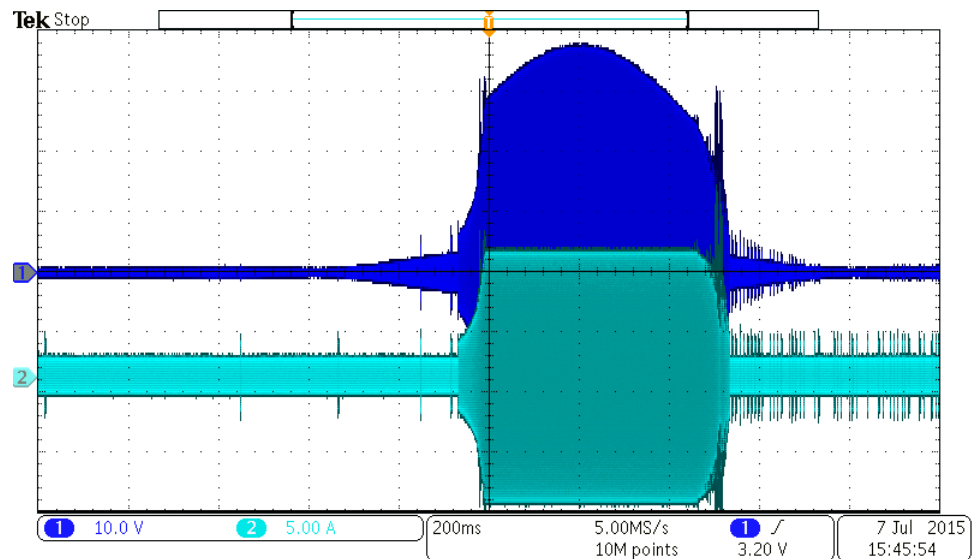

Fig. 5.26: Scope image for 90 percent energy transfer, blue is load voltage and cyan is track current ©[2015] IEEE.

Table 5.4: Results of circuit simulation.

$A(m)$	$g(m)$	Energy (analytical) [%]	Energy (simulation) [%]	Speed [mps]
1.39	0.415	90	84.77	0.4
1.39	0.415	90	80.71	0.8
1.18	0.4	80	78.39	0.4
1.18	0.4	80	78.64	0.8
1.12	0.425	70	63.75	0.4
1.12	0.425	70	61.99	0.8
1.055	0.42	60	52.94	0.4
1.055	0.42	60	45.33	0.8
1.03	0.44	50	41.79	0.4
1.03	0.44	50	36.41	0.8

Chapter 6

Conclusion and Future Work

6.1 Conclusion

This thesis proposes novel approaches to optimization and control of WIPT systems based on lumped transmitting coils. The first optimization algorithm is based on comprehensive search of the solution space. This algorithm is both accurate and time consuming. Thus, an particle swarm optimization based algorithm is proposed. This algorithm significantly reduces the computational cost without sacrificing the comprehensiveness.

Traditional elongated coil based in-motion wireless power transfer systems suffer from high VA rating and very low efficiency ($< 70\%$). On the other hand, lumped coil structures can provide upto 95% efficiency. But, this efficiency can be demonstrated only in the very aligned regions, and considerably reduced efficiency at misaligned regions. This situation presents unique control challenges associated with a lumped coil structure. This thesis proposes a novel feed-forward control algorithm to control the energy transfer in lumped coil structures. The algorithm is analyzed through rigorous analytical analysis and then verified through physical simulations and hardware verification.

6.2 Future Work

This thesis tackles two aspects of lumped transmitting coil based in-motion wireless power transfer. One is the design optimization and another is the control of energy transfer. Future work can be divided into these two main categories.

6.2.1 Optimization

This thesis introduces an artificial intelligence technique for wireless power transfer system design problem. The technique proposed in this thesis is particle swarm optimization.

There are several other artificial intelligence techniques such as ant colony optimization and genetic algorithm. Those other techniques have their benefit as well as deficiencies. Exploring these new techniques is a future extension of this optimization scheme.

6.2.2 Control

This thesis proposes a novel feed-forward control algorithm. Although feed-forward control algorithms are faster, they suffer from noise susceptibility. Thus, in the future, a slower outer feedback loop can be introduced to compensate for the noise susceptibly of the inner loop. Moreover, this thesis explores the exponential candidate function for the feed-forward control algorithm. Several other candidate functions can be explored to attain better performance.

References

[1] E. A. Avallone, T. Baumeister, and A. Sadegh, *Marks' Standard Handbook For Mechanical Engineers (Standard Handbook for Mechanical Engineers)*. Mcgraw-Hill Professional, 2006.

[2] P. Kundur, N. J. Balu, and M. G. Lauby, *Power system stability and control*. McGraw-hill New York, 1994, vol. 7.

[3] T. Gonen, *Electrical Power Transmission System Engineering: Analysis and Design*. CRC Press, 2011.

[4] Z. Yang, W. Liu, and E. Basham, "Inductor modeling in wireless links for implantable electronics," *Magnetics, IEEE Transactions on*, vol. 43, no. 10, pp. 3851–3860, Oct 2007.

[5] A. RamRakhyani, S. Mirabbasi, and M. Chiao, "Design and optimization of resonance-based efficient wireless power delivery systems for biomedical implants," *Biomedical Circuits and Systems, IEEE Transactions on*, vol. 5, no. 1, pp. 48–63, Feb 2011.

[6] S. L. Loke, E. H. Lee, and R. M. Awaida, "Systems and methods for wireless power transfer," Patent, Aug. 23, 2007, uS Patent App. 11/844,242.

[7] E. T. Ozaki, R. Burdo, and S. Farahani, "Systems and methods relating to multi-dimensional wireless charging," Patent, Sep. 25, 2009, uS Patent App. 12/567,339.

[8] C. Liu and A. Hu, "Steady state analysis of a capacitively coupled contactless power transfer system," in *Energy Conversion Congress and Exposition, 2009. ECCE 2009. IEEE*, Sept 2009, pp. 3233–3238.

[9] M. Kline, I. Izyumin, B. Boser, and S. Sanders, "Capacitive power transfer for contactless charging," in *Applied Power Electronics Conference and Exposition (APEC), 2011 Twenty-Sixth Annual IEEE*, March 2011, pp. 1398–1404.

[10] C. S. Tang, Y. Sun, Y. G. Su, S. K. Nguang, and A. Hu, "Determining multiple steady-state zcs operating points of a switch-mode contactless power transfer system," *Power Electronics, IEEE Transactions on*, vol. 24, no. 2, pp. 416–425, Feb 2009.

[11] C. Liu and A. Hu, "Steady state analysis of a capacitively coupled contactless power transfer system," in *Energy Conversion Congress and Exposition, 2009. ECCE 2009. IEEE*, Sept 2009, pp. 3233–3238.

[12] C. Liu, A. Hu, and N.-K. Nair, "Modelling and analysis of a capacitively coupled contactless power transfer system," *Power Electronics, IET*, vol. 4, no. 7, pp. 808–815, Aug 2011.

[13] E. J. Nalos, W. Lund, O. Denman, and S. Rathjen, "Microwave power beaming for long range energy transfer," in *Microwave Conference, 1978. 8th European*, Sept 1978, pp. 573–578.

[14] L. Luk, "Point-to-point wireless power transportation in reunion island," in *International Astronautical Congress, 48 th*, Turin, Italy, 1997.

[15] M. Stuchly, "Health effects of exposure to electromagnetic fields," in *Aerospace Applications Conference*, vol. 1, 1995, pp. 351–368.

[16] J. G. Bolger, F. Kirsten, and L. S. Ng, "Inductive power coupling for an electric highway system," in *Vehicular Technology Conference, 1978. 28th IEEE*, vol. 28, March 1978, pp. 137–144.

[17] J. Shin, S. Shin, Y. Kim, S. Ahn, S. Lee, G. Jung, S.-J. Jeon, and D.-H. Cho, "Design and implementation of shaped magnetic-resonance-based wireless power transfer system for roadway-powered moving electric vehicles," *Industrial Electronics, IEEE Transactions on*, vol. 61, no. 3, pp. 1179–1192, March 2014.

[18] S. Lee, J. Huh, C. Park, N.-S. Choi, G.-H. Cho, and C.-T. Rim, "On-line electric vehicle using inductive power transfer system," in *Energy Conversion Congress and Exposition (ECCE), 2010 IEEE*, Sept 2010, pp. 1598–1601.

[19] J. Huh, S. Lee, W. Lee, G. Cho, and C. Rim, "Narrow-width inductive power transfer system for online electrical vehicles," *Power Electronics, IEEE Transactions on*, vol. 26, no. 12, pp. 3666–3679, Dec 2011.

[20] S. Choi, J. Huh, W. Lee, S. Lee, and C. Rim, "New cross-segmented power supply rails for roadway-powered electric vehicles," *Power Electronics, IEEE Transactions on*, vol. 28, no. 12, pp. 5832–5841, Dec 2013.

[21] G. Covic, J. Boys, M. Kissin, and H. Lu, "A three-phase inductive power transfer system for roadway-powered vehicles," *Industrial Electronics, IEEE Transactions on*, vol. 54, no. 6, pp. 3370–3378, Dec 2007.

[22] M. Budhia, G. Covic, and J. Boys, "Design and optimisation of magnetic structures for lumped inductive power transfer systems," in *Energy Conversion Congress and Exposition, 2009. ECCE 2009. IEEE*, Sept 2009, pp. 2081–2088.

[23] O. C. Onar, J. M. Miller, S. L. Campbell, C. Coomer, C. White, and L. E. Seiber, "A novel wireless power transfer for in-motion ev/phev charging," in *Applied Power Electronics Conference and Exposition (APEC), 2013 Twenty-Eighth Annual IEEE*, March 2013, pp. 3073–3080.

[24] G. Covic and J. Boys, "Inductive power transfer," *Proceedings of the IEEE*, vol. 101, no. 6, pp. 1276–1289, June 2013.

[25] C. Liu, A. Hu, N. Nair, and G. Covic, "2-d alignment analysis of capacitively coupled contactless power transfer systems," in *Energy Conversion Congress and Exposition (ECCE), 2010 IEEE*, Sept 2010, pp. 652–657.

[26] M. Theodoridis, "Effective capacitive power transfer," *Power Electronics, IEEE Transactions on*, vol. 27, no. 12, pp. 4906–4913, Dec 2012.

[27] L. Summerer and O. Purcell, "Concepts for wireless energy transmission via laser," *Europeans Space Agency (ESA)-Advanced Concepts Team*, 2009.

[28] "Laser article in wikipedia (retrieved on 1 april, 2015)." [Online]. Available: https://en.wikipedia.org/wiki/Laser

[29] J. Hagerty, F. Helmbrecht, W. McCalpin, R. Zane, and Z. Popovic, "Recycling ambient microwave energy with broad-band rectenna arrays," *Microwave Theory and Techniques, IEEE Transactions on*, vol. 52, no. 3, pp. 1014–1024, March 2004.

[30] S. Hasanzadeh and S. Vaez-Zadeh, "Efficiency analysis of contactless electrical power transmission systems," *Energy Conversion and Management*, vol. 65, no. 0, pp. 487 – 496, 2013, global Conference on Renewable energy and Energy Efficiency for Desert Regions 2011 2011. [Online]. Available: http://www.sciencedirect.com/science/article/pii/S0196890412002932

[31] J. L. Villa, J. Salln, A. Llombart, and J. F. Sanz, "Design of a high frequency inductively coupled power transfer system for electric vehicle battery charge," *Applied Energy*, vol. 86, no. 3, pp. 355 – 363, 2009. [Online]. Available: http://www.sciencedirect.com/science/article/pii/S0306261908001359

[32] G. A. Covic, G. Elliott, O. Stielau, R. M. Green, and J. T. Boys, "The design of a contact-less energy transfer system for a people mover system," in *Power System Technology, 2000. Proceedings. PowerCon 2000. International Conference on*, vol. 1, 2000, pp. 79–84 vol.1.

[33] O. Stielau and G. A. Covic, "Design of loosely coupled inductive power transfer systems," in *Power System Technology, 2000. Proceedings. PowerCon 2000. International Conference on*, vol. 1, 2000, pp. 85–90 vol.1.

[34] C.-S. Wang, O. Stielau, and G. Covic, "Design considerations for a contactless electric vehicle battery charger," *Industrial Electronics, IEEE Transactions on*, vol. 52, no. 5, pp. 1308–1314, Oct 2005.

[35] J. Sallan, J. Villa, A. Llombart, and J. Sanz, "Optimal design of icpt systems applied to electric vehicle battery charge," *Industrial Electronics, IEEE Transactions on*, vol. 56, no. 6, pp. 2140–2149, June 2009.

[36] S. Hasanzadeh, S. Vaez-Zadeh, and A. Isfahani, "Optimization of a contactless power transfer system for electric vehicles," *Vehicular Technology, IEEE Transactions on*, vol. 61, no. 8, pp. 3566–3573, Oct 2012.

[37] S. Kiwon, H.and Kim, S. Kim, Y. Chun, and S. Ahn, "Design of a wireless power transfer system for railway applications," *International Journal of Railway*, vol. 5, no. 4, pp. 167–174, 2012.

[38] R. Bosshard, J. Kolar, J. Muhlethaler, I. Stevanovic, B. Wunsch, and F. Canales, "Modeling and *eta - alpha* -pareto optimization of inductive power transfer coils for electric vehicles," *Emerging and Selected Topics in Power Electronics, IEEE Journal of*, vol. 3, no. 1, pp. 50–64, March 2015.

[39] C.-Y. Huang, J. Boys, G. Covic, and M. Budhia, "Practical considerations for designing ipt system for ev battery charging," in *Vehicle Power and Propulsion Conference, 2009. VPPC '09. IEEE*, Sept 2009, pp. 402–407.

[40] R. Eberhart and Y. Shi, "Particle swarm optimization: developments, applications and resources," in *Evolutionary Computation, 2001. Proceedings of the 2001 Congress on*, vol. 1, 2001, pp. 81–86 vol. 1.

[41] H. Wu, A. Gilchrist, K. Sealy, and D. Bronson, "A high efficiency 5 kw inductive charger for evs using dual side control," *Industrial Informatics, IEEE Transactions on*, vol. 8, no. 3, pp. 585–595, Aug 2012.

[42] "Us government information about gps (retrieved on 1 april, 2015)." [Online]. Available: http://www.gps.gov/systems/gps/performance/accuracy/

[43] [Online]. Available: http://www.its.dot.gov/DSRC/index.htm

[44] A. Massarini and M. Kazimierczuk, "Self-capacitance of inductors," *Power Electronics, IEEE Transactions on*, vol. 12, no. 4, pp. 671–676, Jul 1997.

[45] G. Grandi, M. Kazimierczuk, A. Massarini, and U. Reggiani, "Stray capacitances of single-layer solenoid air-core inductors," *Industry Applications, IEEE Transactions on*, vol. 35, no. 5, pp. 1162–1168, Sep 1999.

[46] A. Massarini, M. Kazimierczuk, and G. Grandi, "Lumped parameter models for single- and multiple-layer inductors," in *Power Electronics Specialists Conference, 1996. PESC '96 Record., 27th Annual IEEE*, vol. 1, Jun 1996, pp. 295–301 vol.1.

[47] J. Ferreira, "Aring;nalytical computation of ac resistance of round and rectangular litz wire windings," *Electric Power Applications, IEE Proceedings B*, vol. 139, no. 1, pp. 21–25, Jan 1992.

[48] R. D. Marchal-Crespo L., "Effect of robotic guidance on motor learning of a timing task," Scottsdale, AR, 2008.

[49] F.-S. D. W. C. Mataric M.J., Eriksson D.J., "Social assistive robotics for post-stroke rehabilitation," *Journal of Neural Engineering and Rehabilitation*, vol. 4, 2007.

[50] M. Melonis, "Empowering adults with a cognitive disability through inclusion of non-linear context aware prompting technology (ncaps)," in *RESNA Annual Conference 2012*, 2012, pp. 59–108.

[51] C. Bodine, "Assistive technologies in spatial environments," *Cognitive Processing*, vol. 7(1), pp. 167–174, 2006.

[52] "Rerc-act website (retrieved on 1 april, 2015)." [Online]. Available: http://www.rerc-act.org/

[53] T. A. H. W. C. B. R. Z. Z. P. Nazmul Hasan, Isaac Cocar, "A practical implementation of wireless power transfer systems for socially interactive robots," in *Energy Conversion Congress and Exposition (ECCE), 2015 IEEE*, Sept 2015.

[54] J. Kennedy, J. F. Kennedy, and R. C. Eberhart, *Swarm intelligence.* Morgan Kaufmann, 2001.

[55] N. Jin, *Particle swarm optimization in engineering electromagnetics.* ProQuest, 2008.

[56] J. Kennedy and R. Eberhart, "A discrete binary version of the particle swarm algorithm," in *Systems, Man, and Cybernetics, 1997. Computational Cybernetics and Simulation., 1997 IEEE International Conference on*, vol. 5, Oct 1997, pp. 4104–4108 vol.5.

[57] M. Budhia, V. Vyatkin, and G. A. Covic, "Powering flexible manufacturing systems with intelligent contact-less power transfer," in *Industrial Informatics, 2008. INDIN 2008. 6th IEEE International Conference on*, July 2008, pp. 1160–1165.

[58] J.-Y. Lee, H.-Y. Shen, and K.-C. Chan, "Design and implementation of removable and closed-shape dual ring pickup for contactless linear inductive power track system," in *Energy Conversion Congress and Exposition (ECCE), 2013 IEEE*, Sept 2013, pp. 2219–2226.

[59] A. Green and J. Boys, "10 khz inductively coupled power transfer-concept and control," in *Power Electronics and Variable-Speed Drives, 1994. Fifth International Conference on*, Oct 1994, pp. 694–699.

[60] T. S. Z. P. Nazmul Hasan, Hongjie Wang, "A novel position sensorless power transfer control of lumped coil-based in-motion wireless power transfer systems," in *Energy Conversion Congress and Exposition (ECCE), 2015 IEEE*, Sept 2015.

[61] "Differential gps article in wikipedia (retrieved on 1 april, 2015)." [Online]. Available: http://en.wikipedia.org/wiki/Differential_GPS

[62] M. K. M. Klein, Lawrence A. and D. R. Gibson, *Traffic Detector Handbook*, 2006, vol. II.

[63] Y. Su, X. Liu, and S. R. Hui, "Mutual inductance calculation of movable planar coils on parallel surfaces," *Power Electronics, IEEE Transactions on*, vol. 24, no. 4, pp. 1115–1123, 2009.

[64] Z. Pantic, S. Bai, and S. Lukic, "Zcs -compensated resonant inverter for inductive-power-transfer application," *Industrial Electronics, IEEE Transactions on*, vol. 58, no. 8, pp. 3500–3510, Aug 2011.

[65] H. Wu, A. Gilchrist, K. Sealy, P. Israelsen, and J. Muhs, "Design of symmetric voltage cancellation control for lcl converters in inductive power transfer systems," in *Electric Machines Drives Conference (IEMDC), 2011 IEEE International*, May 2011, pp. 866–871.

[66] J. Burdio, F. Canales, P. Barbosa, and F. Lee, "Comparison study of fixed-frequency control strategies for zvs dc/dc series resonant converters," in *Power Electronics Specialists Conference, 2001. PESC. 2001 IEEE 32nd Annual*, vol. 1, 2001, pp. 427–432 vol. 1.

[67] B. Sharp and H. Wu, "Asymmetrical voltage-cancellation control for lcl resonant converters in inductive power transfer systems," in *Applied Power Electronics Conference and Exposition (APEC), 2012 Twenty-Seventh Annual IEEE*, Feb 2012, pp. 661–666.

Appendices

Appendix A

Selection of Controller Coefficients

Table A.1: Selection of coefficients

E(%)	Selection based on $A(m)$			Selection Based on $g(m)$			Selection Based on g_A			Selection Based on f_{ED}		
	$A(m)$	$g(m)$	f_{ED}	$A(m)$	$g(m)$	f_{ED}	$A(m)$	$g(m)$	f_{ED}	$A(m)$	$g(m)$	f_{ED}
8	1	0.49	0.318	1	0.49	0.318	1	0.49	0.318	1	0.49	0.318
14	1	0.485	0.598	1	0.485	0.598	1	0.485	0.598	1	0.485	0.598
21	1.015	0.49	0.738	1	0.475	0.729	1.015	0.49	0.738	1.015	0.49	0.738
25	1.015	0.485	0.839	1.005	0.475	0.807	1.015	0.485	0.839	1.01	0.48	0.841
30	1.035	0.49	0.838	1	0.455	0.774	1.035	0.49	0.838	1.02	0.48	0.881
35	1.05	0.49	0.868	1	0.44	0.786	1.05	0.49	0.868	1.04	0.48	0.903
40	1.05	0.48	0.929	1	0.42	0.803	1.05	0.48	0.929	1.05	0.48	0.929
45	1.09	0.49	0.908	1	0.4	0.81	1.09	0.49	0.908	1.07	0.48	0.944
50	1.115	0.49	0.92	1	0.38	0.815	1.115	0.49	0.92	1.095	0.48	0.956
55	1.145	0.49	0.929	1	0.355	0.823	1.13	0.485	0.959	1.125	0.48	0.965
60	1.185	0.49	0.942	1	0.325	0.836	1.155	0.48	0.964	1.15	0.475	0.97
65	1.23	0.49	0.948	1	0.295	0.847	1.21	0.485	0.962	1.195	0.475	0.977
70	1.285	0.49	0.955	1	0.265	0.857	1.24	0.475	0.977	1.24	0.47	0.984
75	1.36	0.49	0.96	1	0.23	0.87	1.31	0.475	0.98	1.31	0.47	0.986
80	1.46	0.49	0.968	1	0.19	0.888	1.385	0.47	0.984	1.405	0.47	0.991
85	1.605	0.49	0.974	1	0.15	0.905	1.515	0.47	0.988	1.545	0.47	0.994
90	1.84	0.445	0.98	1	0.105	0.929	1.66	0.455	0.989	1.7	0.46	0.996
100	1.975	0.245	0.996	1.005	0.01	0.996	1.975	0.245	0.996	1.05	0.01	1

Appendix B

Published Papers

■ Nazmul Hasan, Tarak Saha, Hongjie Wang and Zeljko Pantic, *A Novel Position Sensorless Power Transfer Control of Lumped Coil Based In-Motion Wireless Power Transfer Systems*, Accepted in to the Energy Conversion Congress and Exposition (ECCE), Montreal 2015.

■ Nazmul Hasan, Tuba Yilmaz, Regan Zane, Zeljko Pantic, *Multi-Objective Particle Swarm Optimization Applied to the Design of Wireless Power Transfer Systems*, IEEE Wireless Power Transfer Conference (WPTC), Bolder 2015.

■ Nazmul Hasan, Isaac Cocar, Thomas Amely, Hongjie Wang, Cathy Bodine, Regan Zane and Zeljko Pantic , *A Practical Implementation of Wireless Power Transfer Systems for Socially Interactive Robots*, Accepted in the Energy Conversion Congress and Exposition (ECCE), Montreal 2015.